UNIVERSITÉ MONTPELLIER II

Sciences et techniques du Languedoc

THÈSE

Présentée à L'Université Montpellier II – Sciences et techniques du Languedoc
pour obtenir le diplôme de Doctorat

École Doctorale : Systèmes Intégrés en Biologie, Agronomie, Géosciences, Hydrosciences, Environnement

Spécialité : Biologie intégrative des plantes

Modélisation mathématique, simulation numérique et contrôle optimal des rétroactions entre biomécanique et croissance de l'arbre

par

Thomas Guillon

Soutenue le 12 décembre 2011

Jury

Evelyne Costes	Directeur de recherche (INRA)	Présidente du Jury
Yves Dumont	Chargé de recherche (CIRAD)	Examinateur
Thierry Fourcaud	Chargé de recherche (CIRAD)	Directeur de thèse
Georges Jeronimidis	Professeur (University of Reading)	Rapporteur
Gérard Maugin	Directeur de recherche (CNRS)	Examinateur
B. Daya Reddy	Professeur (University of Cape Town)	Rapporteur

---

UMR botAnique et bioinforMatique de l'Architecture des Plantes
CIRAD, TA A51/PS2, 34398 Montpellier cedex 5

à Eliane, Clémence et Serge

REMERCIEMENTS

Je tiens tout d'abord à remercier mon directeur de thèse, Thierry Fourcaud, qui m'a accordé sa confiance, son soutien et sa disponibilité pour réaliser ce travail durant ces trois années.

Je remercie chaleureusement Yves Dumont pour son aide, ses encouragements et son implication sur les aspects mathématiques.

Je remercie vivement Georges Jeronimidis et Daya Reddy pour avoir accepté d'être les rapporteurs de ma thèse et pour leurs conseils avisés.

Je remercie également Evelyne Costes et Gérard Maugin de m'avoir fait honneur de leur présence à Montpellier pour ma soutenance et pour leurs commentaires passionnants.

Je remercie Tancrède Alméras pour les discussions fructueuses que nous avons eu sur la biomécanique de l'arbre.

Mes remerciements s'adressent également à toute l'équipe de l'UMR AMAP pour son accueil chaleureux. Toutes les discussions informelles avec les chercheurs et les étudiants ont constitué des moments précieux pour le développement de ma thèse.

Enfin, je tiens à remercier chaleureusement tous mes proches et ma famille qui m'ont encouragé durant la réalisation de ce projet, en particulier ma femme Joy, pour son soutien inestimable.

TABLE DES MATIÈRES

Chapitre 1

PRÉSENTATION

1.1 Introduction

Recouvrant 31% de la surface terrestre, les arbres et les forêts ont un rôle majeur dans le développement économique et social des populations (sylviculture, industrie du bois et du papier), ils participent également au maintien de la biodiversité et atténuent les effets dus aux changements climatiques [1]. D'un point de vue biologique, le concept d'arbre n'est pas précisément défini, il repose davantage sur l'identification d'un ensemble de caractéristiques non exclusives des plantes, telles que la taille, la longévité, la présence de bois ou la pérennité d'une tige rigide [2, 3]. La hauteur est considérée comme le principal trait écologique de l'arbre, elle représente l'intensité de la compétition pour la lumière chez les plantes [4]. Cependant, la croissance en hauteur des arbres est nécessairement limitée. D'une part, au cours de la photosynthèse, la biomasse allouéee à la croissance en hauteur ne peut être investi dans le développement de feuilles et d'organes reproducteurs. D'autre part, une hauteur importante fragilise la stabilité mécanique de la structure et impose, en retour, un investissement supplémentaire de biomasse pour assurer la fonction de support (développement des racines, augmentation du diamètre du tronc) [5, 6].

Dans ce contexte, la biomécanique de l'arbre est une discipline située à l'interface de la biologie et de l'ingénierie mécanique [5]. Elle permet d'analyser les compromis réalisés dans les stratégies de croissance des arbres. Cette démarche repose sur l'idée essentielle que les lois de la physique s'appliquent également aux organismes vivants et que la performance de la forme d'une structure biologique peut être ainsi analysée et quantifiée. Les applications de la biomécanique de l'arbre sont nombreuses et concernent la qualité du bois [7], le risque de casse au vent dans le cadre de la sylviculture [8] et en milieu urbain [9] mais également l'éco-ingénierie de la stabilité des pentes par les racines d'arbre [10].

1.2 Les mouvements de l'arbre

La croissance de l'arbre a pour principal objectif l'exploration de l'espace afin d'optimiser l'interception de la lumière et d'acquérir des nutriments, notamment par les racines [6]. Concernant la partie aérienne de l'arbre, la croissance primaire correspond à une augmentation de la longueur des axes de l'arbre, alors que la croissance secondaire se définit par l'augmentation de leur diamètre. Les changements de la géométrie et l'évolution de la masse se traduisent ainsi par un mouvement de l'ensemble de la structure lié à l'augmentation du poids propre et aux moments de flexion. Cette double contrainte mécanique entraine inévitablement l'affaissement de toute la structure. Ces effets doivent alors être compensés par un mécanisme permettant de contrôler la position de l'arbre pendant la croissance [11]. Il existe deux mécanismes permettant d'induire un mouvement qui contrebalance les effets de l'augmentation du poids propre :

- au cours de la croissance primaire, des divisions cellulaires asymétriques ou une expansion asymétrique des cellules localisées sur le méristème apical, engendre une modification de la courbure à l'extrémité de la tige, permettant ainsi d'orienter la direction de la croissance (voir figure 1.1(a)) ;
- au cours de la croissance secondaire, à la périphérie de l'axe, les nouvelles cellules subissent une phase de maturation se traduisant par une déformation. S'il y a formation de bois de réaction, cette déformation est asymétrique (plus importante à un côté du cerne) et les nouvelles cellules étant solidaires du bois précédemment formé, cela génère une contrainte à l'intérieur de la section engendrant à son tour, un mouvement de l'ensemble de la structure [12]. Cette déformation peut correspondre à un rétrécissement plus important à un côté du cerne (bois de tension, voir figure 1.1(c)) ou à un allongement (bois de compression, voir figure 1.1(d)).

La combinaison de ces deux phénomènes permet ainsi à l'arbre d'orienter sa croissance vers la lumière (phototropisme) tout en contrôlant les effets dus à l'augmentation du poids propre (gravitropisme négatif) [13]. Par ailleurs, l'apparition de nouvelles cellules non déformées à la périphérie

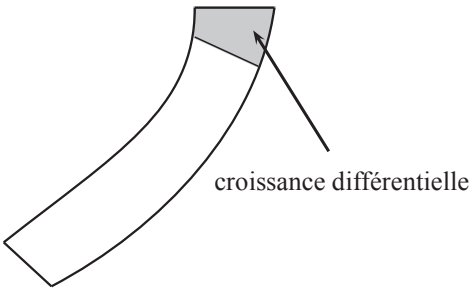

(a) Croissance différentielle du méristème apicale avec une expansion des cellules ou des divisions cellulaires plus importantes sur le côté droit, ce qui engendre une courbure et réoriente l'axe vers la gauche.

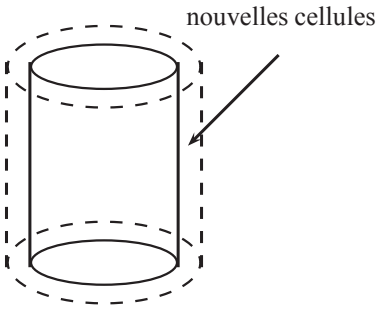

(b) L'axe étant compressé par son poids propre, les nouvelles cellules apparaissant à la périphérie, pendant la croissance secondaire, rigidifient les sections droites.

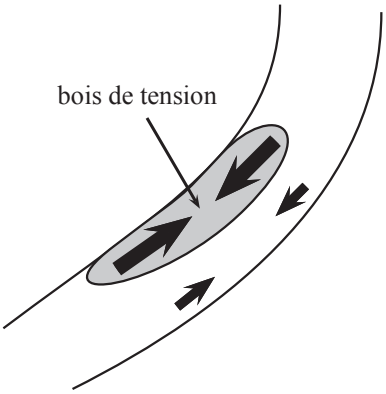

(c) Formation de bois de tension qui se traduit par le rétrécissement plus important des nouvelles cellules à un côté du cerne pendant leur phase de maturation.

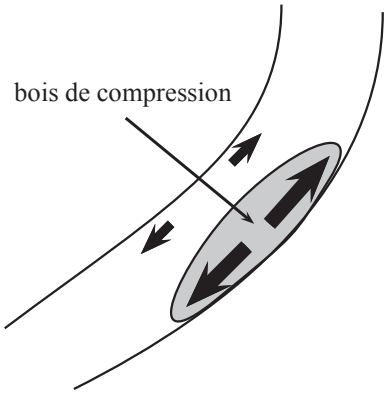

(d) Formation de bois de compression qui se traduit par l'allongement plus important des nouvelles cellules à un côté du cerne pendant leur phase de maturation.

Fig. 1.1: Les mécanismes de contrôle impliqués dans les stratégies de croissance de l'arbre.

d'un cerne préalablement déformé augmente la rigidité de l'axe (voir figure 1.1(b)). Ce phénomène améliore la résistance mécanique de l'arbre, notamment par rapport aux effets du vent [7], mais il s'oppose à l'efficacité de la formation du bois de réaction pour la réorientation de la structure [14]. Ainsi, l'objectif de cette thèse est de développer un modèle mathématique afin de quantifier les effets de chaque facteur engendrant un mouvement de l'arbre. Ce modèle permettra d'analyser les stratégies de croissance de l'arbre en fonction de différents contextes écologiques.

1.3 Modélisation mathématique de la biomécanique de l'arbre en croissance

La modélisation mathématique des effets biomécaniques de la croissance de l'arbre dépasse le cadre de la théorie classique de la mécanique des structures. Le problème majeur concerne la définition d'une configuration de référence pour un solide en croissance [15]. En effet, en mécanique des milieux continus, l'existence d'une déformation, c'est-à-dire la variation de la distance entre deux points du solide au cours d'un mouvement, est uniquement détectée relativement à une configuration fixe servant de référence. La configuration de référence est arbitraire, elle est cependant souvent choisie comme la configuration initiale du solide, avant l'application des efforts. Or, dans le cas d'une structure en croissance, la configuration initiale ne contient aucun des points matériels qui apparaitront avec la croissance et il est donc impossible d'estimer les déformations mécaniques qu'ils subiront. D'autre part, la superposition de nouveaux points matériels libres de contraintes, sur une surface préalablement déformée, pose un problème de modélisation qui n'est pas abordé dans la théorie classique.

Afin de surmonter ces difficultés, des approches incrémentales ont été développées dans différents travaux [16, 17, 18, 19, 20]. Ces démarches séparent les effets de la croissance et des déformations mécaniques. A partir d'une discrétisation du temps, on considère qu'à chaque instant, une nouvelle couche de points matériels libres de contraintes est apposée sur la surface en croissance de la dernière configuration déformée, formant ainsi une configuration intermédiaire précontrainte. Puis, à partir de cette configuration intermédiaire, un nouvel équilibre mécanique est calculé en considérant l'incrément d'efforts extérieurs qui s'ajoute à la croissance. Cette approche algorithmique, limite fortement l'analyse mathématique du problème mécanique puisqu'elle correspond à une approximation numérique explicite d'un modèle en temps continu inconnu. Il est donc impossible d'évaluer les erreurs de la discrétisation et d'analyser les propriétés qualitatives du modèle.

Le premier article composant cette thèse (chapitre 2), intitulé *A new mathematical framework for modelling the biomechanics of growing trees with rod theory*, propose un nouveau formalisme mathématique reposant sur la théorie des poutres [21] et permet de modéliser en temps continu et simultanément la croissance et la biomécanique de l'arbre. La contribution essentielle de ce travail est l'obtention d'un système d'équations aux dérivées partielles modélisant l'ensemble des rétroactions entre croissance et biomécanique de l'arbre. Il est alors possible d'exploiter tous les outils mathématiques de l'analyse. De plus, en considérant les mouvements dans un plan d'une poutre inextensible et sans cisaillement, il est possible pour la première fois, d'obtenir une solution analytique du problème dans le cas de petits changements d'angles. Ces solutions mettent également en évidence les différentes stratégies de croissance que l'arbre peut développer pour le redressement des branches.

1.4 Méthodes numériques pour la biomécanique de l'arbre en croissance

Si les changements d'angles sont importants (redressement de l'axe principal d'un arbre, etc.), les solutions exactes du système d'équations aux dérivées partielles obtenues au chapitre précédent

(chapitre 2) ne sont plus réalistes pour analyser la dynamique de l'arbre. Il est alors nécessaire de développer des méthodes numériques pour résoudre les équations non linéaires. Le deuxième article de cette thèse (chapitre 3), intitulé *Numerical methods for the biomechanics of growing trees*, compare un ensemble de méthodes numériques pour simuler la biomécanique de la croissance de l'arbre. Le modèle est reformulé en couplant deux problèmes :

- un problème portant sur l'angle de déformation de la poutre avec des conditions aux limites pour la variable d'espace ;
- un problème de Cauchy décrivant l'évolution de la courbure intrinsèque de la poutre due à la croissance secondaire.

A partir de cette formulation, la dépendance entre l'espace et le temps impose de résoudre l'équation de l'équilibre mécanique portant sur l'angle de déformation à chaque instant. De plus, il apparait que des conditions de régularité plus importantes doivent être considérées pour l'équation portant sur l'équilibre mécanique. La résolution numérique repose donc sur une approximation avec les éléments finis d'Hermite. Concernant le problème de Cauchy, plusieurs schémas numériques sont étudiés : les schémas d'Euler explicite et implicite, les méthodes de Heun et de Crank-Nicolson. Une attention particulière est portée sur la précision du schéma d'Euler explicite, puisqu'il s'apparente aux approches incrémentales développées précédemment [16, 17, 18, 19, 20]. Les résultats montrent que la précision des méthodes numériques dépend fortement de la valeur des paramètres de vitesse de croissance radiale et du rayon du méristème apical. Dans les cas les moins favorables (vitesse de croissance radiale importante et faible valeur pour le rayon du méristème apical), même avec de très petits pas de temps, l'erreur globale pour la méthode d'Euler explicite peut atteindre un ordre de grandeur important. En revanche, les méthodes implicites peuvent présenter des instabilités dans le cas de grands pas de temps. Ainsi, cet article présente les caractéristiques essentielles des méthodes numériques en fonction des valeurs des paramètres du modèle.

1.5 Controle optimal de l'allocation de biomasse pour un arbre en croissance

Le troisième et dernier article de cette thèse (chapitre 4), intitulé *Optimal control of biomass allocation in primary and secondary growth for the gravitropic response of a growing stem*, exploite les précédents développements afin de comparer les stratégies de croissance de l'arbre dans différents contextes écologiques. En effet, les expérimentations menées en champ ou en laboratoire mettent en évidence des stratégies de redressement très variées selon les espèces [14, 22, 23]. La capacité de la réponse gravitropique (ou phototropique) peut dépendre de la tolérance à l'ombre de l'espèce [14], mais aussi de stratégies écologiques plus spécifiques, comme la capacité pour un jeune arbre à exploiter un trou de lumière dans la canopée [24]. Ces stratégies de croissance reposent sur l'allocation dynamique de la biomasse à la croissance primaire (permettant la croissance en hauteur) et à la croissance secondaire (permettant de rigidifier ou de réorienter l'axe principal). Ainsi, une formulation mathématique de deux problèmes de contrôle optimal pour un axe initialement incliné est proposée afin de comparer :

1. l'allocation dynamique de la biomasse qui maximise la hauteur à chaque instant, ce qui correspond à une situation de forte compétition pour la lumière dans un peuplement dense ;
2. l'allocation dynamique de la biomasse qui maximise la hauteur en un laps de temps déterminé, ce qui correspond à la situation d'un jeune arbre en croissance devant dépasser une canopée fermée afin d'optimiser l'interception de la lumière.

Les conditions nécessaires du premier ordre de ces deux problèmes sont alors évaluées à partir de la résolution des équations adjointes [25, 26]. Puis, la méthode du gradient projeté est détaillée pour obtenir une approximation numérique. Ce travail donne ainsi les bases théoriques pour analyser et comparer les stratégies de croissance des arbres en fonction des différents contextes écologiques.

Références

[1] FAO, Situation des forêts du monde, Tech. rep., Organisation des Nations Unies pour l'alimentation et l'agriculture, Rome (2011).

[2] F. Hallé, R. Oldeman, P. Tomlinson, Tropical trees and forests : an architectural analysis, Springer-Verlag, Berlin, 1978.

[3] R. J. Petit, A. Hampe, Some evolutionary consequences of being a tree, Annual Review of Ecology, Evolution, and Systematics 37 (2006) 187–214.

[4] D. S. Falster, M. Westoby, Plant height and evolutionary games, Trends in Ecology and Evolution 18 (2003) 337–343.

[5] K. J. Niklas, Plant biomechanics : an engineering approach to plant form and function, The Univeristy of Chicago Press, 1992.

[6] M. Fournier, A. Stokes, C. Coutand, T. Fourcaud, B. Moulia, Ecology and biomechanics : a mechanical approach to the ecology of animals and plants, CRC Taylor and Francis, 2006, Ch. 1 : Tree Biomechanics and Growth Strategies in the Context of Forest Functional Ecology, pp. 1–33.

[7] T. Alméras, J. Gril, D. Julien, M. Fournier, Growth-related stresses in stems - modelling their development and biological function, Revue Forestière Française 6 (2008) 749–760.

[8] P. Ancelin, B. Courbaud, T. Fourcaud, Development of an individual tree-based mechanical model to predict wind damage within forest stands, Forest Ecology and Management 203 (2004) 101–121.

[9] K. R. James, N. Haritos, P. K. Ades, Mechanical stability of trees under dynamic loads, American Journal of Botany 93 (2006) 1522–1530.

[10] J. Norris, A. Stokes, S. Mickovski, E. Cammeraat, R. van Beek, B. Nicoll, A. Achim (Eds.), Slope Stability and Erosion Control : Ecotechnological Solutions, Springer, 2008.

[11] B. Moulia, C. Coutand, C. Lenne, Posture control and skeletal mechanical acclimation in terrestrial plants : Implication for mechanical modeling of plant architecture, American Journal of Botany 93 (2006) 1477–1489.

[12] M. Fournier, H. Bailleres, B. Chanson, Tree biomechanics : Growth, cumulative prestresses, and reorientations, Biomimetics 2 (1994) 229–251.

[13] B. Moulia, M. Fournier, The power and control of gravitropic movements in plants : a biomechanical and systems biology view, Journal of Experimental Botany 60 (2009) 461–486.

[14] T. Alméras, M. Derycke, G. Jaouen, J. Beauchêne, M. Fournier, Functional diversity in gravitropic reaction among tropical seedlings in relation to ecological and developmental traits, Journal of Experimental Botany 60 (2009) 4397–4410.

[15] D. Ambrosi, F. Mollica, On the mechanics of a growing tumor, International Journal of Engineering Science 40 (2002) 1297–1316.

[16] H. Yamamoto, M. Yoshida, T. Okuyama, Growth stress controls negative gravitropism in woody plant stem, Planta 216 (2002) 280–292.

[17] T. Fourcaud, P. Lac, Numerical modelling of shape regulation and growth stresses in trees. part i : An incremental static finite element formulation, Trees 17 (2003) 23–30.

[18] N. Hodge, P. Papadopoulos, A continuum theory of surface growth, Proceedings of the Royal Society of London A 466 (2010) 3135–3152.

[19] O. M. O'Reilly, T. N. Tresierras, On the evolution of intrinsic curvature in rod-based models of growth in long slender plant stem, International Journal of Solids and Structure 48 (2011) 1239–1247.

[20] J.-D. M. Catherine Coutand and, G. Jeronimidis, J.-F. Destrebecq, Twig : A model to simulate the gravitropic response of a tree axis in the frame of elasticity and viscoelasticity, at intra-annual time scale, Journal of Theoretical Biology 273 (2011) 115–129.

[21] S. S. Antman, Nonlinear Problems of Elasticity, Springer, 2005, Ch. 8 : Theory of Rods Deforming in Space, pp. 269–344.

[22] R. Herrera, C. Krier, C. Lalanne, E. H. M. Ba, A. Stokes, F. Salin, T. Fourcaud, S. Claverol, C. Plomion, (not) keeping the stem straight : a proteomic analysis of maritime pine seedlings undergoing phototropism and gravitropism, BMC Plant Biology 10 (2010) 217.

[23] M. Ba, F. Salin, T. Fourcaud, A. Stokes, Reorientation strategies in leaning stems of young maritime pine (*Pinus pinaster*) and loblolly pine (*Pinus taeda*), IAWA Journal 31 (2010) 465–480.

[24] C. Collet, M. Fournier, F. Ningre, A. P.-I. Hounzandji, T. Constant, Growth and posture control strategies in fagus sylvatica and acer pseudoplatanus saplings in response to canopy disturbance, Annals of Botany 107 (2011) 1345–1353.

[25] M. Gunzburger, Adjoint equation-based methods for control problems in incompressible, viscous flows, Flow, Turbulence and Combustion 65 (2000) 249–272.

[26] M. Hinze, R. Pinnau, M. Ulbrich, S. Ulbrich, Optimization with PDE Constraints, Springer, 2009.

Chapitre 2

A NEW MATHEMATICAL FRAMEWORK FOR MODELLING THE BIOMECHANICS OF GROWING TREES WITH ROD THEORY

Thomas Guillon* Yves Dumont† Thierry Fourcaud†

Abstract

The analysis of the shape evolution of growing trees requires an accurate modelling of the interaction between growth and biomechanics, including both static and adaptive responses. However, this coupling is a problematic issue since the progressive addition of new material on an existing deformed body makes the definition of a reference configuration unclear. This article presents a new mathematical framework for rod theory that allows overcoming this difficulty in the case of slender structures that grow both in length and diameter like tree branches. A key point in surface growth problems is the strong dependency between space and time. On this basis, the virtual reference configuration was defined as the set of initial geometric properties of the cross-sections at their date of appearance. The classical balance equations of the rod theory were then reformulated with respect to this evolving reference configuration. This new continuous formulation leads to an evolution equation of the relaxed configuration that takes into account changes in material and geometrical properties of the growing rod.

Primary (linked to growth in length) and secondary (linked to growth in diameter) tropisms, i.e. the adaptive biomechanical response of growing trees to the local environment, were also considered as a component of remodelling in tree growth, which modifies the relaxed configuration. Analytical solutions of our growth model was found in simple cases, i.e. assuming planar and small deflections and considering a linear elastic constitutive law. Corresponding motion results were compared with results provided by the classical rod theory and analysed with regards to growth strategies involved in gravitropic responses. These first qualitative results show that the proposed mathematical model was able to simulate the main processes involved in tree growth. This mathematical formalism is particularly suited to study the biomechanical response of trees subjected to quasi-static loads. This contribution also provides new insight into a more general three-dimensional theory of surface growth and raises new mathematical challenges about the analysis of this original system of partial differential equations.

Keywords : Surface growth, Cambial growth, Cell maturation strain, Gravitropism, Continuous modelling, Nonlinear partial differential equations.

∗. Université Montpellier II, UMR AMAP, TA-A51/PS2, boulevard de la Lironde, 34398 Montpellier Cedex 5, France

†. CIRAD, UMR AMAP, TA-A51/PS2, boulevard de la Lironde, 34398 Montpellier Cedex 5, France

2.1 Introduction

The analysis of shape evolution in growing trees is highly related to the interaction between their growth dynamics and biomechanical responses. Tree growth and development mainly aim to explore space in order to optimize light interception and nutrient acquisition. Growth of tree axes, i.e. stem and branches, results from two processes that correspond to 1 – growth in length, also called primary or apical growth; 2 – growth in cross-section area, which is called cambial or secondary growth. Growing trees are subjected to mechanical loadings such as gravity or wind forces [1]. Consequently, they have to develop growth strategies in order to find a trade-off between their mechanical stability and other physiological functions [2]. The mechanical stability of trees is controlled by material and/or structural modifications. Material adaptation is linked with wood formation and differentiation, and their resulting properties, e.g. wood density, cell wall width or microfibril angles. Wood formation [3] takes place in the cambial zone that is located at the periphery of the axes, i.e. between the xylem and the bark. Consequently, although secondary growth can results in a material variability within the structure, it does not change the material properties of the inner wood core once this wood is already mature. Secondary growth is thus assimilated to a surface growth. Structural control consists in modifying tree shape by increasing the diameter of stem and branches, changing tree topology (self-pruning and ramification) and/or reorienting existing axes (primary and secondary tropisms) [1, 4]. Secondary tropism, e.g. straightening up of tree axes or negative gravitropism, is a key process in tree stability, which originates from a differential elongation or shortening of wood fibres during their maturation phase (longitudinal maturation strains) within a given cross-section. Such a biomechanical process is repeated for each new formed cells during the whole axes life span, generating internal prestresses, called maturation stresses, which cumulate during tree growth [5, 6].

A mathematical description of the biomechanics of trees is of considerable importance to identify and analyse the major mechanisms involved in tree growth. In biology, surface growth is classically defined as the accretion of new material points at the external or internal surface of a tissue [7, 8, 9]. The coupling between surface growth and mechanics highlights theoretical issues that exceed the traditional framework of structural mechanics due to the evolution of the domain geometry [10]. The specificity of surface growth raises at least two questions.

1. How to define a reference configuration ? This question consists of two geometrical issues. First, the reference configuration is represented by a three dimensional manifold whereas the initial configuration is just a surface that is represented by a two-dimensional manifold. Thus, the usual computation of the deformation gradient between the initial configuration and the current configuration is inappropriate [11]. Second, the surface growth field over the reference configuration may possibly depend on information from the current configuration (environmental control of tree growth).
2. How to model the deposition of new unstrained material on an existing deformed surface ? This question is concerned with the evolution of material and geometrical properties in the case of non-conservative mass and volume, which is of mechanical interest.

The mathematical description of surface growth kinematics for rigid bodies has been largely developed by Skalak and coworkers in [7, 9]. A traditional way to model the mechanical response of growing bodies is to use an incremental approach [12, 13]. This approach consists in adding new material layers to the surface of the last known prestressed configuration, and, subsequently, computing the new deformed configuration under load increments at the current step. As trees are slender structures, the incremental approach has been used in conjunction with rod (or beam) theory in order to simulate the mechanical response of growing stems [14, 15, 16]. The remodelling phenomenon involved by growth processes were also studied and applied to plant stems [17, 18], but the effects of primary and secondary growth were finally considered with a similar incremental approach [19]. All these models separate growth and mechanical effects, thus avoiding the main

theoretical questions mentioned above. Furthermore, the mathematical analysis of the growth problem remains impossible since these models are based on explicit discrete-time schemes of unknown continuous-time models.

The purpose of this study is to provide a new mathematical framework to deal with continuous-time surface growth problems for the special Cosserat theory of rods [20]. In this framework, mechanical and growth effects are considered simultaneously. This paper is organized as follows. In section 2.2, the geometry of the different configurations of a growing rod is examined and leads to the definition of a growing reference configuration as a set of initial conditions for the new material points provided by growth organs. Section 2.3 and 2.4 set the balance equations and the constitutive relations of the growing rod. Section 2.5 gives supplementary hypotheses necessary to model tree growth, which mainly concern the reorientation of the apical shoot during primary growth, the increase of linear mass density due to secondary growth, the evolution of the relaxed configuration due to changes in material and geometrical properties of the rod cross-sections and the movements induced by a differential in maturation strains (DMS) of newly formed wood cells. The planar motion of a growing rod is analysed in Section 2.6 and leads to analytical solutions in the case of linearized equations. Solutions of the dynamic problem are compared with the classical rod theory. The model is then parametrized in order to simulate realistic growth strategies of tree branches. Concluding remarks about the contribution of this theory for future works in surface growth modelling, in particular in the context of tree biomechanics, are provided in Section 2.7.

2.2 The geometry of deformation

This section is devoted to the definition of different configurations needed to model the movement of a growing rod. We denote $\mathbf{E}^3$ the three-dimensional euclidean space with an oriented orthonormal basis $(\boldsymbol{i}, \boldsymbol{j}, \boldsymbol{k})$. First, a fixed reference configuration is described and leads to the definition of the material parametrization and the set of all admissible material points at each time. The current configuration is then given at each time by the actual position and orientation of the existing cross-sections. The relaxed configuration is defined as the rod geometry obtained when all external loads have been removed from the current configuration. This relaxed configuration is time-dependent since growth process may change material and geometrical properties of the cross-section. Finally, the definition of the reference configuration is completed and defined as the set of initial conditions of strains in the relaxed configuration.

2.2.1 The reference configuration

Some remarks about the definition of a reference configuration

The definition of a reference configuration in the framework of surface growth has been considered as a problematic issue because new material points, which did not exist before, must be added at each time at the surface of the deformed body [10, 12, 13]. However, the reference configuration is just a time-independent placement of all material points in the physical space and does not necessarily correspond to an observed configuration in a given motion [21, 22]. In the context of surface growth, an important distinction has to be made between the body, which is a time-varying continuous set of material points, and the reference configuration, which gives a time-independent map of the body in the euclidean space. Finally, the major interest in the definition of a reference configuration is to identify the geometrical implications of oriented growth, i.e. primary growth path, separately from those due to mechanical effects with a static material parametrization.

Defining the reference configuration of a growing rod

Following the notations of Antman [20], the reference configuration of a rod is defined by the three vector-valued functions:

$$[0, L(t)] \ni s \mapsto \boldsymbol{r}^\circ(s), \boldsymbol{d}_1^\circ(s), \boldsymbol{d}_2^\circ(s) \in \mathbf{E}^3 \tag{2.1}$$

where $\boldsymbol{d}_1^\circ$ and $\boldsymbol{d}_2^\circ$ are orthonormal and represent the orientation of the material cross-sections of the rod and $\boldsymbol{r}^\circ$ is the base curve of the rod identifying the position of the material cross-sections of the body in the euclidean space. As the reference configuration is arbitrary, the material parameter s is chosen to be the arc-length. Thus, at each time t, the elongation of the axis due to the primary growth of the rod is characterized by the increase in length of the base curve $L(t)$. It follows from the above mentioned remark that the time varying body is identified at each time t with $[0, L(t)]$ and that primary growth corresponds to the addition of new material points at the end of the base curve, completing the reference configuration without motion (see figure 2.1). The apical growth

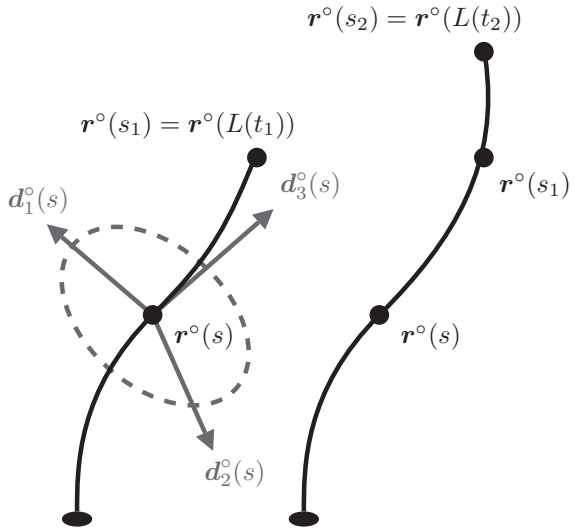

Fig. 2.1: Growth of the base curve of the rod $\boldsymbol{r}^\circ$ representing the reference configuration at time t_1 and t_2. At each cross-section, the orthonormal basis $\left(\boldsymbol{d}_i^\circ(s)\right)_{i=1,2,3}$ gives the orientation of the cross-sections.

velocity is considered known, denoted by $v_a(t) = \mathrm{d}L(t)/\mathrm{d}t$. The length L is assumed to be a strictly increasing function of time, then the inverse function $\gamma(s)$ gives the date of appearance of a material point at arc-length s. This indicates that time and space are not independent which is a specific feature of the surface growth phenomena. The set of all admissible material points at each time is then given by (see figure 2.2):

$$\mathcal{Q} = \left\{(s,t)/t \in \mathbb{R}^+, s \in [0, L(t)]\right\} \tag{2.2}$$

This set $\mathcal{Q}$ is a key element to identify the initial and the boundary conditions in the formulation of the mechanical problem of surface growth. To be more precise, at each time t, we can consider the two boundary points located at the ends of the rod, i.e. at $s = 0$ and $s = L(t)$, which is equivalent to the couples $(0, t) \in \mathcal{Q}$ and $(L(t), t) \in \mathcal{Q}$. Conversely, at each arc-length s, the time $t = \gamma(s)$ could be used to represent an initial condition at the appearance of the material point at arc-length s, which is equivalent to the couple $(s, \gamma(s)) \in \mathcal{Q}$. In order to build the reference configuration, it remains to define $\boldsymbol{r}^\circ$, $\boldsymbol{d}_1^\circ$ and $\boldsymbol{d}_2^\circ$ which will be done in the following section.

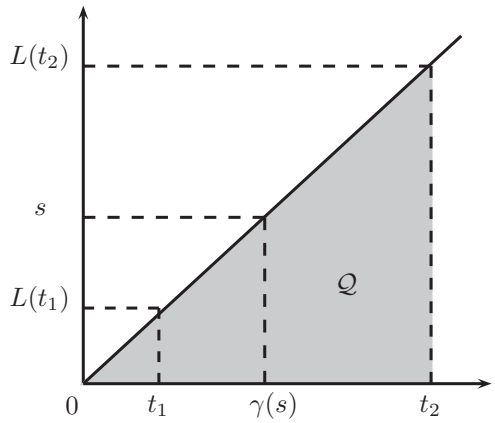

(a) Cumulated length of a growing rod as a linear function in time (infinite growth with constant speed).

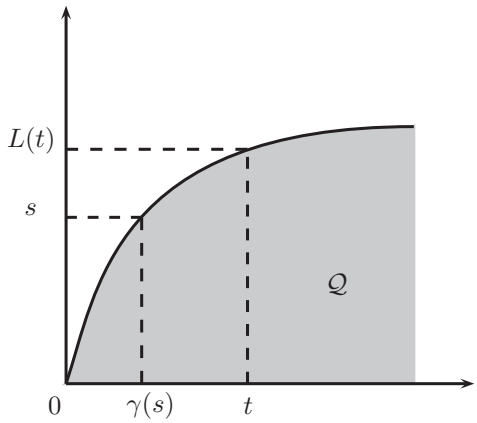

(b) Characteristic cumulated length of plant growth (see [23] for an example on Maritime pine trees).

Fig. 2.2: Kinetics of rod elongation and corresponding basic set of the whole rod cross-sections in space-time. At each arc-length s, the inverse function γ gives the date of appearance of the material point located on the base curve of the rod.

2.2.2 The current configuration

As a result of the definition of the basic set $\mathcal{Q}$ in space-time, the motion of a rod is given at each time and each admissible arc-length by the three vector-valued functions:

$$\mathcal{Q} \ni (s,t) \mapsto \boldsymbol{r}(s,t), \boldsymbol{d}_1(s,t), \boldsymbol{d}_2(s,t) \in \mathbf{E}^3 \tag{2.3}$$

where $\boldsymbol{r}(s,t)$ gives the position of cross-section s at time t in the current configuration. At each arc-length s, an orthonormal basis is defined by setting $\boldsymbol{d}_3 = \boldsymbol{d}_1 \times \boldsymbol{d}_2$, which gives the orientation of the cross-section at time t. The vectors $(\boldsymbol{d}_i)_{i=1,2,3}$ are called the directors of the rod and we now define the strain vector-valued functions $\boldsymbol{u}$ and $\boldsymbol{v}$ such that [20]:

$$\begin{aligned} \partial_s \boldsymbol{d}_i &= \boldsymbol{u} \times \boldsymbol{d}_i \\ \partial_s \boldsymbol{r} &= \boldsymbol{v} \end{aligned} \tag{2.4}$$

The components of $\boldsymbol{u}$ and $\boldsymbol{v}$ in the local basis $(\boldsymbol{d}_i)_{i=1,2,3}$ are denoted by:

$$\begin{aligned} \mathbf{u} &= (u_1, u_2, u_3) \\ \mathbf{v} &= (v_1, v_2, v_3) \end{aligned} \tag{2.5}$$

where u_1 and u_2 are related to the bending strains, u_3 is called the torsional strain or twist, v_1 and v_2 are the shear strains and finally, $v_3 > 0$ is the dilatation. We consider that the rod is fixed at the origin with a specified orientation, which is equivalent to the following kinematics boundary conditions:

$$\begin{aligned} \boldsymbol{d}_i(0,t) &= \boldsymbol{d}_{0i} \\ \boldsymbol{r}(0,t) &= \mathbf{0} \end{aligned} \tag{2.6}$$

Then, it follows from equations (2.4) and from the boundary conditions (2.6), that the knowledge of $\boldsymbol{u}$ and $\boldsymbol{v}$ leads to the computation of $\boldsymbol{d}_i$ and $\boldsymbol{r}$, $\forall (s,t) \in \mathcal{Q}$.

2.2.3 The relaxed configuration

About the definition of *remodelling* in tree growth

In the previous section we have defined the properties of the current configuration, giving the position of the base curve and the orientation of the cross-sections at each time. However, growth

involves processes that do not necessary induce a motion in the current configuration, while they modify the relaxed configuration. According to Taber [8] the evolution of the form of biological organisms results from three main processes, i.e. growth (change in mass), remodelling (change in material properties) and morphogenesis (change in shape). However these phenomena are closely linked and their definition (as given by Taber) is not univocal. For instance, remodelling is often considered as a result of growth and includes both a change in material and geometrical properties [4]. In this paper, we define *remodelling* in tree growth as the set of biological processes that modify the relaxed configuration in the rod theory. We distinguish three main phenomena:

1. The cambial or secondary growth, i.e. the accretion of new material points at the surface of the xylem (new wood cells are indeed formed in the cambium that is located between the xylem and the bark). This process results in an increase in cross-section areas and second moment of inertia, and thus increases the rod stiffness. However the newly formed cells do not participate in the balance of forces applied previously to the system, i.e. preexisting stresses are not redistributed over the new rod cross-section area and the strain in the neighbours of these new material points remains zero (see [1]).
2. The spatial variation in wood properties [3], which is mainly due to cell differentiation, e.g. formation of reaction wood, cambium ageing, climate variations and heartwood formation. This material variation results in a change in apparent stiffness (Modulus of Elasticity) of the rod.
3. The tropisms, i.e. movements induced by external stimulus as light or gravity [24]. In the non-lignified region located at the stem/branch tip, movements are induced by a differential growth, i.e. more cells are formed on one side of the axis. In the current model, this process called primary reorientation has been considered geometrically and not as resulting from a mechanical process (see section 2.5.1). Bending and twisting of the lignified parts of a tree axis are induced by a differential in maturation strains (DMS) of wood cells along the perimeter of xylem cross-sections [1]. This DMS is due to the local formation of reaction wood that has different structural and mechanical properties compared to the normal wood. Although these phenomena induce a movement of the rod in the current configuration, the stress field involved does not balance external forces and is auto-equilibrated. Consequently, this process also modifies the shape of the relaxed (in the sense of releasing the external forces) configuration, as well as the distribution of stresses and strains within the cross-sections [15].

An important part of remodelling can be associated to an acclimative response of trees, e.g. thigmomorphogenesis when considering mechanical perturbations [25]. Remodelling effects have already been addressed in plant growth models in [17, 18, 19], who have suggested an evolution equation for the intrinsic curvature of the rod but without details about the underlying biological processes. Moreover, it is important to notice that changes in geometry and material properties in plants are concomitant with the growth process. In particular, the evolution of mass accretion due to primary and secondary growth is missing in [17] and [18] and is still described with an incremental approach in [19].

Notations for the relaxed configuration

The relaxed configuration is defined at time t as the geometry of the rod when all external forces are removed from the current configuration. In order to account for the evolution of the material and geometrical properties of the cross-sections and for tropisms, the relaxed configuration will be denoted by (see figure 2.3):

$$\mathcal{Q} \ni (s,t) \mapsto \boldsymbol{r}^*(s,t), \boldsymbol{d}_1^*(s,t), \boldsymbol{d}_2^*(s,t) \in \mathbf{E}^3 \tag{2.7}$$

The equations in (2.4) also applied to the relaxed configuration:

$$\begin{aligned} \partial_s \boldsymbol{d}_i^* &= \boldsymbol{u}^* \times \boldsymbol{d}_i^* \\ \partial_s \boldsymbol{r}^* &= \boldsymbol{v}^* \end{aligned} \tag{2.8}$$

and the components of the strain measures $\boldsymbol{u}^*$ and $\boldsymbol{v}^*$ in the local basis $(\boldsymbol{d}_i^*)_{i=1,2,3}$ are given by:

$$\begin{aligned} \mathbf{u}^* &= (u_1^*, u_2^*, u_3^*) \\ \mathbf{v}^* &= (v_1^*, v_2^*, v_3^*) \end{aligned} \tag{2.9}$$

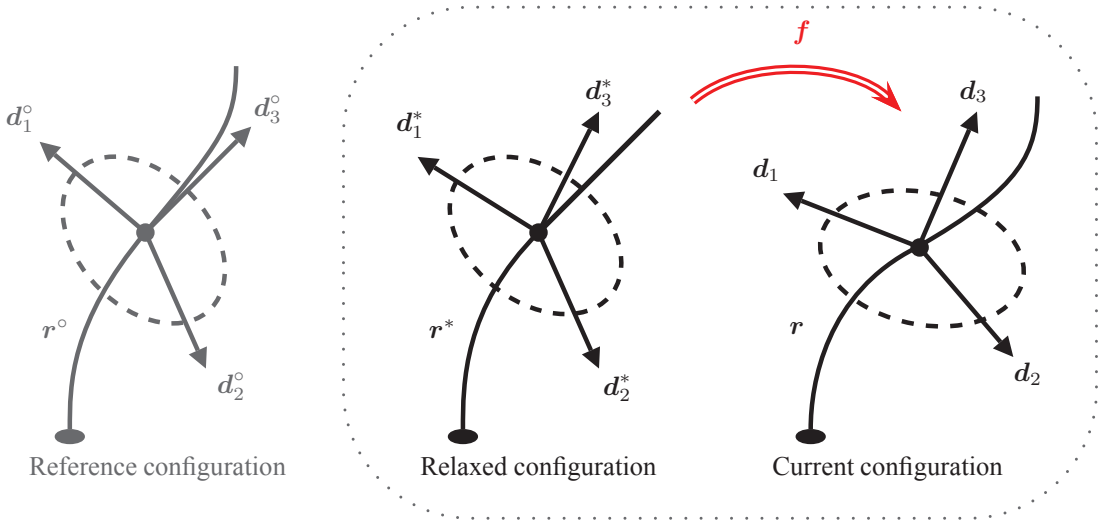

Fig. 2.3: At each time t, we consider a representation of the reference configuration $(\boldsymbol{r}^\circ, \boldsymbol{d}_i^\circ)$ which gives the initial conditions of strains in the others configurations. The relaxed configuration $(\boldsymbol{r}^*, \boldsymbol{d}_i^*)$ which depends on the evolution of the material and geometrical properties of the cross-sections, is defined at each time of growth as the unloaded (suppression of external loads) geometry of the rod. The current configuration $(\boldsymbol{r}, \boldsymbol{d}_i)$ corresponds to the actual motion of the rod when external forces are added to the relaxed configuration. The reference configuration is static whereas the quantities inside the dotted box may evolve in time.

The reference configuration as a set of initial conditions of strains

At each time, the length of the base curve of the reference configuration increases, but it remains to define the geometrical properties of this curve. As the reference configuration is arbitrary, we choose the simplest general description for the strain vectors:

$$\begin{aligned} \mathbf{u}^\circ &= (0, \kappa^\circ, \tau^\circ) \\ \mathbf{v}^\circ &= (0, 0, 1) \end{aligned} \tag{2.10}$$

Here, $\boldsymbol{u}^\circ$ and $\boldsymbol{v}^\circ$ are usually called *initial strain vectors* [20] even though they do not originate from a mechanical deformation but describe the initial geometry of the rod. Therefore, the local basis $(\boldsymbol{d}_i^\circ)_{i=1,2,3}$ corresponds to the Serret-Frenet frame and κ° and τ° are respectively the curvature and the torsion of the base curve of the reference configuration. The equation (2.4) is equivalent to the Serret-Frenet formulae and we have:

$$\begin{aligned} \frac{\mathrm{d}\boldsymbol{d}_i^\circ}{\mathrm{d}s} &= \boldsymbol{u}^\circ \times \boldsymbol{d}_i^\circ \\ \frac{\mathrm{d}\boldsymbol{r}^\circ}{\mathrm{d}s} &= \boldsymbol{d}_3^\circ \end{aligned} \tag{2.11}$$

The reference configuration is growing in length in a direction that may depend on information about the position in the current configuration, thus κ° and τ° are unknown and have to be deduced from a growth law describing the preferential orientation of the primary growth at the date of appearance of each cross-section s (see section 2.5.1). This is the case in particular in biological systems when growth is modified by biotic, e.g. strains [26], or abiotic, e.g. gravity or light, factors [4]. The geometry of the reference configuration does not represent any real motion of the rod. This geometry characterizes the relative change in the orientation of the cross-sections at their date of appearance, i.e.:

$$\begin{aligned} \mathbf{u}^*(s,\gamma(s)) &= \mathbf{u}^\circ(s) \\ \mathbf{v}^*(s,\gamma(s)) &= \mathbf{v}^\circ(s) \end{aligned} \tag{2.12}$$

Finally, the definition of the reference configuration contains all the necessary information about the geometrical part of the growth process, including both genotypic and phenotypic (environmental dependent) components of growth, and is summarized by the quantities v_a, κ° and τ°.

2.3 Balance equations

We denote $\boldsymbol{n}, \boldsymbol{m}$ and $\boldsymbol{f}, \boldsymbol{l}$ respectively, the resultant contact force and couple, and the body force and body couple per unit of arc-length in the reference configuration. Considering that growth is a sufficiently slow process, the following quasi-static balance equations are considered [20]:

$$\begin{aligned} \partial_s \boldsymbol{n} + \boldsymbol{f} &= \mathbf{0} \\ \partial_s \boldsymbol{m} + \partial_s \boldsymbol{r} \times \boldsymbol{n} + \boldsymbol{l} &= \mathbf{0} \end{aligned} \tag{2.13}$$

The components of $\boldsymbol{n}$ and $\boldsymbol{m}$, in the local basis $(\boldsymbol{d}_i)_{i=1,2,3}$ are denoted:

$$\begin{aligned} \mathbf{n} &= (n_1, n_2, n_3) \\ \mathbf{m} &= (m_1, m_2, m_3) \end{aligned} \tag{2.14}$$

We suppose that the rod is free at $s = L(t)$, then the boundary conditions are given by:

$$\begin{aligned} \boldsymbol{n}(L(t),t) &= \mathbf{0} \\ \boldsymbol{m}(L(t),t) &= \mathbf{0} \end{aligned} \tag{2.15}$$

2.4 Constitutive relations

We consider the constitutive relations of an extensible and shearable elastic rod. As growth may change material and geometrical properties, the constitutive relations have an explicit dependence on time:

$$\begin{aligned} \mathbf{n}(s,t) &= \hat{\mathbf{n}}\big(\mathbf{u}(s,t) - \mathbf{u}^*(s,t), \mathbf{v}(s,t) - \mathbf{v}^*(s,t), s, t\big) \\ \mathbf{m}(s,t) &= \hat{\mathbf{m}}\big(\mathbf{u}(s,t) - \mathbf{u}^*(s,t), \mathbf{v}(s,t) - \mathbf{v}^*(s,t), s, t\big) \end{aligned} \tag{2.16}$$

We assume that the functions $\hat{\mathbf{n}}$ and $\hat{\mathbf{m}}$ are differentiable and satisfy the monotonicity conditions (see [20] for more details) and that $\forall (s,t) \in \mathcal{Q}$:

$$\hat{\mathbf{n}}(\mathbf{0},\mathbf{0},s,t) = \hat{\mathbf{m}}(\mathbf{0},\mathbf{0},s,t) = \mathbf{0}$$

This condition ensures that the resultant contact force and couple vanish in the relaxed configuration. We also suppose that the relations (2.16) is invertible and we have:

$$\begin{aligned} \mathbf{u}(s,t) &= \mathbf{u}^*(s,t) + \hat{\mathbf{u}}\big(\mathbf{n}(s,t), \mathbf{m}(s,t), s, t\big) \\ \mathbf{v}(s,t) &= \mathbf{v}^*(s,t) + \hat{\mathbf{v}}\big(\mathbf{n}(s,t), \mathbf{m}(s,t), s, t\big) \end{aligned} \tag{2.17}$$

such that $\forall(s,t) \in \mathcal{Q}$:

$$\hat{\mathbf{u}}(\mathbf{0},\mathbf{0},s,t) = \hat{\mathbf{v}}(\mathbf{0},\mathbf{0},s,t) = \mathbf{0}$$

for the same reason as in (2.16). We can notice that the boundary conditions (2.15) taken at $t = \gamma(s)$ with the constitutive relation (2.17) lead to:

$$\begin{aligned} \mathbf{u}(s,\gamma(s)) &= \mathbf{u}^*(s,\gamma(s)) = \mathbf{u}^\circ(s) \\ \mathbf{v}(s,\gamma(s)) &= \mathbf{u}^*(s,\gamma(s)) = \mathbf{v}^\circ(s) \end{aligned} \tag{2.18}$$

2.5 Hypotheses beyond tree growth

Equations (2.4), (2.13), (2.16), together with the boundary conditions (2.6), (2.15) give the classical equations of Cosserat's rod theory. In the case of tree growth, we have to establish the geometry of the reference configuration that results from primary growth, as well as the evolution of the relaxed configuration. This evolution is affected by the secondary growth involving changes in material and geometrical properties. Consequently, some relations have to be specified, in order to obtain a well-posed problem and to solve (2.11) and (2.8).

2.5.1 Primary growth

The primary growth gives the geometry of the base curve $\boldsymbol{r}^\circ$ and the initial strains defining the orientation $(\boldsymbol{d}_i^\circ)_{i=1,2,3}$ of the cross-sections of the rod. However, the orientation of the apex may depend on information resulting from the current configuration, e.g. in the case of phototropism or negative gravitropism where the stem movement is oriented with respect to the direction of light and gravity respectively. More generally, curvature κ° and torsion τ° can be driven according to growth strategies and thus be a function of both date, current geometry, current mechanical state, etc. From equations (2.11) and (2.10), it follows that relations on the curvature and the torsion are needed, e.g.:

$$\begin{aligned} \kappa^\circ(s) &= \hat{\kappa}^\circ(s,\gamma(s),\boldsymbol{r}(s,\gamma(s)),\boldsymbol{d}_i(s,\gamma(s)),\ldots) \\ \tau^\circ(s) &= \hat{\tau}^\circ(s,\gamma(s),\boldsymbol{r}(s,\gamma(s)),\boldsymbol{d}_i(s,\gamma(s)),\ldots) \end{aligned} \tag{2.19}$$

These functions must be continuous to ensure the existence and uniqueness of a solution to the system (2.11) with the boundary condition (2.6). In the most simple case, if no direction is favoured for the apical growth (i.e. there are no feedback), then it leads to $\kappa^\circ = \tau^\circ = 0$ and the reference configuration becomes a straight line oriented by $\boldsymbol{d}_{03}$.

If there is a fixed preferential direction of growth $\boldsymbol{d}_P$, we can establish a simple relation for κ° and τ°. Starting from the arc-length s, we assume that apical growth direction reaches the preferential direction $\boldsymbol{d}_P$ after an increase in length of δ, i.e. $\boldsymbol{d}_3(s+\delta,\gamma(s)) = \boldsymbol{d}_P$. Then, the Taylor approximation of $\boldsymbol{d}_3$ at s and time $\gamma(s)$ with the relations (2.18) gives:

$$\begin{aligned} \boldsymbol{d}_3(s+\delta,\gamma(s)) &= \boldsymbol{d}_3(s,\gamma(s)) + \delta\partial_s\boldsymbol{d}_3(s,\gamma(s)) + \frac{\delta^2}{2}\partial_{ss}\boldsymbol{d}_3(s,\gamma(s)) \\ &= \left(\kappa^\circ(s)\delta + \frac{\mathrm{d}\kappa^\circ}{\mathrm{d}s}(s)\frac{\delta^2}{2}\right)\boldsymbol{d}_1(s,\gamma(s)) \\ &\quad + \kappa^\circ(s)\tau^\circ(s)\frac{\delta^2}{2}\boldsymbol{d}_2(s,\gamma(s)) + \left(1-\kappa^\circ(s)^2\frac{\delta^2}{2}\right)\boldsymbol{d}_3(s,\gamma(s)) \end{aligned} \tag{2.20}$$

Taking the scalar product of the previous relation with $\boldsymbol{d}_i(s,\gamma(s))$ for $i = 1,2,3$ we obtain the

following system:

$$\begin{aligned}
\boldsymbol{d}_P \cdot \boldsymbol{d}_1(s,\gamma(s)) &= \kappa^\circ(s)\delta + \frac{\mathrm{d}\kappa^\circ}{\mathrm{d}s}(s)\frac{\delta^2}{2} \\
\boldsymbol{d}_P \cdot \boldsymbol{d}_2(s,\gamma(s)) &= \kappa^\circ(s)\tau^\circ(s)\frac{\delta^2}{2} \\
\boldsymbol{d}_P \cdot \boldsymbol{d}_3(s,\gamma(s)) &= 1 - \kappa^\circ(s)^2\frac{\delta^2}{2}
\end{aligned} \tag{2.21}$$

for which the solutions for κ°, $\frac{\mathrm{d}\kappa^\circ}{\mathrm{d}s}$ and τ° are given by:

$$\begin{aligned}
\kappa^\circ(s) &= \operatorname{sgn}\Big(\boldsymbol{d}_P \cdot \boldsymbol{d}_1(s,\gamma(s))\Big)\frac{\kappa_{\max}}{2}\sqrt{2\Big(1 - \boldsymbol{d}_P \cdot \boldsymbol{d}_3(s,\gamma(s))\Big)} \\
\frac{\mathrm{d}\kappa^\circ}{\mathrm{d}s}(s) &= \frac{\kappa_{\max}^2}{2}\left(\boldsymbol{d}_P \cdot \boldsymbol{d}_1(s,\gamma(s)) - \operatorname{sgn}\Big(\boldsymbol{d}_P \cdot \boldsymbol{d}_1(s,\gamma(s))\Big)\sqrt{2\Big(1 - \boldsymbol{d}_P \cdot \boldsymbol{d}_3(s,\gamma(s))\Big)}\right) \\
\tau^\circ(s) &= \begin{cases} \operatorname{sgn}\Big(\boldsymbol{d}_P \cdot \boldsymbol{d}_1(s,\gamma(s))\Big)\kappa_{\max}\dfrac{\boldsymbol{d}_P \cdot \boldsymbol{d}_2(s,\gamma(s))}{\sqrt{2\Big(1 - \boldsymbol{d}_P \cdot \boldsymbol{d}_3(s,\gamma(s))\Big)}} & \text{if } \kappa^\circ(s) \neq 0 \\ 0 & \text{if } \kappa^\circ(s) = 0 \end{cases}
\end{aligned} \tag{2.22}$$

where $\kappa_{\max} = 2/\delta$ corresponds to the maximum curvature induced by primary growth and *sgn* is the sign-function. These relations ensure that the initial strain is defined such that for all arc-length s, $\boldsymbol{d}_3(s,\gamma(s))$ is getting closer to the preferential direction $\boldsymbol{d}_P$.

2.5.2 Secondary growth

Increase of mass

The secondary growth involves the evolution of the geometry of the cross-sections and an increase in mass. Regarding the evolution of the geometry, we assume for simplicity that the cross-sections are circular with a radius r solution of the problem:

$$\begin{aligned}
\partial_t r(s,t) &= v_r(s,t) \\
r(s,\gamma(s)) &= r_0(s)
\end{aligned} \tag{2.23}$$

where v_r is the radial growth velocity and $r_0 > 0$ corresponds to the radius of the primary meristem, i.e. pith radius in the case of plants. The area of the cross-sections for every $(s,t) \in \mathcal{Q}$ is given by:

$$A(s,t) = \pi r^2(s,t) \tag{2.24}$$

Assuming a constant mass density in the reference configuration, the linear mass $\bar{\rho}$ is defined for $(s,t) \in \mathcal{Q}$ by:

$$\bar{\rho}(s,t) = \rho A(s,t) = \rho\pi r^2(s,t) \tag{2.25}$$

An equation for the evolution of the geometrical and material properties of the cross-sections

We now address the question of the evolution of the relaxed configuration. This configuration accounts for changes in geometry and material properties of the cross-sections. These changes do not cause any movement in the current configuration, since the preexisting material points of the cross-sections already balance the external body force and couple. Therefore, to derive a supplementary equation accounting for the effects of remodelling, we assume that in a short lapse of time Δt, the growth process generates changes in material or geometrical properties of the cross-sections without an increase in mass. This means that during this short lapse of time, the relaxed

configuration is changing whereas the current configuration remains static. Using equation (2.17) at times t and $t + \Delta t$, we obtain from the previous assumption, that:

$$\begin{aligned} \mathbf{u}^*(s,t) + \hat{\mathbf{u}}(\mathbf{n}(s,t), \mathbf{m}(s,t), s, t) &= \mathbf{u}^*(s, t+\Delta t) + \hat{\mathbf{u}}(\mathbf{n}(s,t), \mathbf{m}(s,t), s, t+\Delta t) \\ \mathbf{v}^*(s,t) + \hat{\mathbf{v}}(\mathbf{n}(s,t), \mathbf{m}(s,t), s, t) &= \mathbf{v}^*(s, t+\Delta t) + \hat{\mathbf{v}}(\mathbf{n}(s,t), \mathbf{m}(s,t), s, t+\Delta t) \end{aligned} \tag{2.26}$$

By regrouping the terms in the same side, dividing by Δt and considering $\Delta t \to 0$, we find $\forall (s,t) \in \mathcal{Q}$:

$$\begin{aligned} \partial_t \mathbf{u}^*(s,t) + \partial_t \hat{\mathbf{u}}(\mathbf{n}(s,t), \mathbf{m}(s,t), s, t) &= \mathbf{0} \\ \partial_t \mathbf{v}^*(s,t) + \partial_t \hat{\mathbf{v}}(\mathbf{n}(s,t), \mathbf{m}(s,t), s, t) &= \mathbf{0} \end{aligned} \tag{2.27}$$

These equations ensure that without modification of the contact force and couple, the current configuration is not moving whereas the relaxed configuration may evolve with respect to changes in geometrical or material properties of the cross-sections. According to the definition of the reference configuration (2.18), we consider the following initial conditions for these evolution equations:

$$\begin{aligned} \mathbf{u}^*(s, \gamma(s)) &= \mathbf{u}^\circ(s) \\ \mathbf{v}^*(s, \gamma(s)) &= \mathbf{v}^\circ(s) \end{aligned} \tag{2.28}$$

These initial conditions express that new material cross-sections are free of deformation at their date of appearance.

Equations (2.27) call important remarks. First, these equations point out that the evolution of the relaxed configuration is driven by the history of the contact force and couple and by the evolution of the material and geometrical properties of the cross-sections. It is thus important to notice that there is no stationary solution, since the equations vanish if $\partial_t \hat{\mathbf{u}} = \partial_t \hat{\mathbf{v}} = \mathbf{0}$. In this case, it results from equations (2.28) that the reference and the relaxed configuration coincide (i.e. there is no changes in material and geometrical properties for all cross-sections). Therefore, there is no obvious limit values for $\mathbf{u}^*$ and $\mathbf{v}^*$ as time is increasing. This result is in contradiction with previous growth models which assumed that $\mathbf{u}^* \to \mathbf{u}$ and $\mathbf{v}^* \to \mathbf{v}$ when time increases (see [18, 19] for instance) . This difference is explained by the fact that the cited works do not model simultaneously the effects of the remodelling and the increase of mass due to the growth process.

Modeling secondary tropisms

The equations (2.27) model the evolution of the relaxed configuration due to changes in geometrical and material properties of the cross-sections. However, equations of motion should also take into consideration tropisms, which correspond to an active biomechanical response of tree growth to its environment. In order to account for movements induced by DMS, an additional term is introduced in equation (2.27):

$$\begin{aligned} \partial_t \mathbf{u}^*(s,t) + \partial_t \hat{\mathbf{u}}(\mathbf{n}(s,t), \mathbf{m}(s,t), s, t) &= \mathbf{p}(s,t) \\ \partial_t \mathbf{v}^*(s,t) + \partial_t \hat{\mathbf{v}}(\mathbf{n}(s,t), \mathbf{m}(s,t), s, t) &= \mathbf{q}(s,t) \end{aligned} \tag{2.29}$$

where $\boldsymbol{p}$ and $\boldsymbol{q}$ are strain rates related to the DMS effect and depend on v_r. The derivation of equation (2.27) highlights that the additional terms $\mathbf{p}$ and $\mathbf{q}$ in (2.29) will cause a movement of the current configuration.

2.6 Planar motion of a growing branch

This section is devoted to the theoretical study of the planar motion of a growing branch. First, simple assumptions are made about the constitutive relations and the kinetics of primary and secondary growth, leading to a reduced system of partial differential equations. Then, we assume that the rod deflection is sufficiently small so that the system allows the calculation of exact solutions. Finally, the exact solutions of the current framework are compared with the classical rod theory and are analysed with respect to growth strategies involved in the gravitropic response.

2.6.1 Planar motion of an inextensible and unshearable growing rod

We consider the motion in the plane $(\boldsymbol{i}, \boldsymbol{j})$ of an inextensible and unshearable rod which starts to grow in direction $\boldsymbol{a}_0 = \cos(\theta_0)\boldsymbol{i} + \sin(\theta_0)\boldsymbol{j}$. These assumptions lead to the following simplifications of the strain vectors:

$$\mathbf{u}^\circ = (0, \kappa^\circ, 0)\ \mathbf{u}^* = (0, \kappa^*, 0)\ \mathbf{u} = (0, \kappa, 0) \tag{2.30}$$

$$\mathbf{v}^\circ = (0, 0, 1)\ \ \mathbf{v}^* = (0, 0, 1)\ \ \mathbf{v} = (0, 0, 1) \tag{2.31}$$

In this case, the material parameter s corresponds to the arc-length in all configurations, and the cross-sections are always orthogonal to the base curve. We also simplify the notations for the directors by setting $\boldsymbol{a} = \boldsymbol{d}_3$, $\boldsymbol{b} = \boldsymbol{d}_1$ and $\boldsymbol{k} = \boldsymbol{d}_2$. We denote θ the angle between $\boldsymbol{i}$ and $\boldsymbol{a}$ (see figure 2.4), thus we have $\partial_s\theta = \kappa$. We denote, $\boldsymbol{f} = f_x\boldsymbol{i} + f_y\boldsymbol{j}$, $\boldsymbol{n} = n_x\boldsymbol{i} + n_y\boldsymbol{j}$, $m = m_2$, $p = p_2$, and we

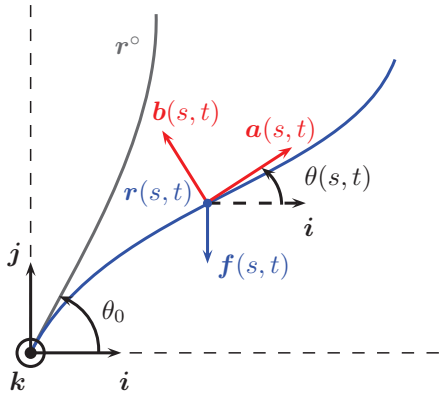

Fig. 2.4: Planar motion of an inextensible and unshearable growing rod subjected to its self-weight $\boldsymbol{f}$. The base curve of the reference configuration is represented by $\boldsymbol{r}^\circ$ whereas the current configuration is represented by $\boldsymbol{r}$ and the local basis $(\boldsymbol{a}, \boldsymbol{b}, \boldsymbol{k})$.

consider a linear elastic constitutive relation:

$$\kappa(s,t) = \kappa^*(s,t) + \frac{m(s,t)}{EI(s,t)} \tag{2.32}$$

where E is a constant Young's modulus, and $I(s,t) = \pi r^4(s,t)/4$ is the geometrical moment of inertia of the cross-section at s and at time t. Then, equations (2.13), (2.17), (2.29) are reduced to:

$$\begin{cases} \partial_s n_x = -f_x \\ \partial_s n_y = -f_y \\ \partial_s m = n_x \sin\theta - n_y \cos\theta \\ \partial_t \kappa^* = \dfrac{\partial_t EI}{(EI)^2} m + p \\ \partial_s \theta = \kappa^* + \dfrac{m}{EI} \\ \partial_s \boldsymbol{r} = \cos\theta\boldsymbol{i} + \sin\theta\boldsymbol{j} \end{cases} \tag{2.33}$$

The initial-boundary conditions from (2.15), (2.28), (2.6) reduce to:

$$\begin{cases} n_x(L(t),t) = 0 \\ n_y(L(t),t) = 0 \\ m(L(t),t) = 0 \\ \kappa^*(s,\gamma(s)) = \kappa^\circ(s) \\ \theta(0,t) = \theta_0 \\ \boldsymbol{r}(0,t) = \mathbf{0} \end{cases} \tag{2.34}$$

Hypotheses beyond tree growth

For simplicity reasons, we assume that the apical growth velocity v_a and the radial growth velocity v_r are constant, we obtain the following functions:

$$\begin{aligned} L(t) &= v_a t \\ \gamma(s) &= \frac{s}{v_a} \\ r(s,t) &= v_r t - \frac{v_r}{v_a} s + r_0 \end{aligned} \tag{2.35}$$

We consider that the growing rod is only subjected to its self-weight, hence we have $\boldsymbol{f} = -\rho g \pi r^2 \boldsymbol{j}$ and:

$$\begin{aligned} n_x(s,t) &= 0 \\ n_y(s,t) &= -\frac{1}{3}\rho g \pi (v_a t - s)\left(r^2 + r_0 r + r_0^2\right) \end{aligned} \tag{2.36}$$

Assuming that the orientation of the stem is driven by a preferential growth angle θ_P, primary reorientation is described by (2.22):

$$\begin{aligned} \kappa^\circ(s) &= \operatorname{sgn}\left(\sin\left(\theta_P - \theta(s,\gamma(s))\right)\right)\frac{\kappa_{\max}}{2}\sqrt{2\Big(1-\cos\left(\theta_P - \theta(s,\gamma(s))\right)\Big)} \\ &= \kappa_{\max}\sin\left(\frac{\theta_P - \theta(s,\gamma(s))}{2}\right) \end{aligned} \tag{2.37}$$

and

$$\frac{\mathrm{d}\kappa^\circ}{\mathrm{d}s}(s) = \kappa_{\max}^2\left(\frac{1}{2}\sin\left(\theta_P - \theta(s,\gamma(s))\right) - \sin\left(\frac{\theta_P - \theta(s,\gamma(s))}{2}\right)\right) \tag{2.38}$$

The curvature variation induced by DMS is formulated as in [6]. We also assume that DMS intensity and direction depend on the local deviation between the current orientation of the cross-section and the preferential orientation as in [14]. The change of curvature rate of the rod due to DMS is given by:

$$p = 2\frac{v_r}{r^2}\alpha\sin\left(\theta_P - \theta\right) \tag{2.39}$$

where α is the maximum DMS between normal and reaction wood. Thus $p(s,t)$ gives the change of curvature per unit time that results from the formation and maturation of reaction wood cells per unit time at the periphery of the cross-section located at the arc length s and at time t. The analytical expressions of $p(s,t)$ integrates the mechanical effect of the location and maturation strains of reaction wood and can be given by any mechanosensing model that makes the link between the actual mechanical state, the biological reaction to this mechanical stimulus (e.g. location and density of reaction wood, intensity of maturation strains) and the resulting auto-equilibrated stress field (see for instance [27] and [28]).

Calculation of the exact solution in the case of small deflection

In order to calculate analytical solutions of the previous system, we suppose that the rod deflection is small ($\theta \approx \theta_0$). The approximation of the zeroth order of (2.33) gives:

$$\begin{cases} \partial_s m = -n_y \cos\theta_0 \\ \partial_t \kappa^* = \dfrac{\partial_t EI}{(EI)^2} m + 2\alpha \dfrac{v_r}{r^2} \sin(\theta_P - \theta_0) \\ \partial_s \theta = \kappa^* + \dfrac{m}{EI} \\ \partial_s \boldsymbol{r} = \cos\theta_0 \boldsymbol{i} + (\sin\theta_0 + (\theta - \theta_0)\cos\theta_0)\boldsymbol{j} \end{cases} \tag{2.40}$$

If $\theta_P = \pi/2$ and $\theta_0 = 0$, then the previous approximation is of first order. The approximation of the zeroth order of the initial-boundary conditions (2.34) is given by:

$$\begin{cases} m(L(t), t) = 0 \\ \kappa^*(s, \gamma(s)) = \kappa_{\max} \sin\left(\dfrac{\theta_P - \theta_0}{2}\right) \\ \theta(0, t) = \theta_0 \\ \boldsymbol{r}(0, t) = \boldsymbol{0} \end{cases} \tag{2.41}$$

Finally, the integration of the approximated system (2.40) gives the following solutions:

$$m(s,t) = -\frac{\rho g \pi}{12} \cos\theta_0 (v_a t - s)^2 \left(r^2 + 2r_0 r + 3r_0^2\right) \tag{2.42}$$

$$\kappa^*(s,t) = -\frac{1}{3}\frac{\rho g}{E}\cos\theta_0 \left[\left(\frac{2v_a}{v_r}\right)^2 \left(1 - \frac{r}{r_0} + \log\left(\frac{r}{r_0}\right)\right) + \frac{(v_a t - s)^2}{r_0^2}\left(4\frac{r_0}{r} + \frac{5}{3}\frac{r_0^2}{r^2} - \frac{2}{3}\frac{r_0^3}{r^3} - 3\frac{r_0^4}{r^4}\right)\right] + 2\alpha \sin(\theta_P - \theta_0)\left(\frac{1}{r_0} - \frac{1}{r}\right) + \kappa_{\max}\sin\left(\frac{\theta_P - \theta_0}{2}\right) \tag{2.43}$$

$$\kappa(s,t) = -\frac{4}{3}\frac{\rho g}{E}\cos\theta_0 \left[\left(\frac{v_a}{v_r}\right)^2 \left(1 - \frac{r}{r_0} + \log\left(\frac{r}{r_0}\right)\right) + \frac{(v_a t - s)^2}{r_0^2}\left(\frac{r_0}{r} + \frac{2}{3}\frac{r_0^2}{r^2} + \frac{1}{3}\frac{r_0^3}{r^3}\right)\right] + 2\alpha \sin(\theta_P - \theta_0)\left(\frac{1}{r_0} - \frac{1}{r}\right) + \kappa_{\max}\sin\left(\frac{\theta_P - \theta_0}{2}\right) \tag{2.44}$$

$$\theta(s,t) = \theta_0 - \frac{4}{3}\frac{\rho g}{E}\cos\theta_0 \left(\frac{v_a}{v_r}\right)^3 \left[-r\log\left(\frac{r}{r_0}\right) + \frac{r_0^3}{6}\left(\frac{1}{r^2} - \frac{1}{(v_r t + r_0)^2}\right) - \frac{4}{3}\frac{v_r}{v_a}s + (v_r t + r_0)\log\left(\frac{v_r t + r_0}{r_0}\right)\right] + 2\alpha\sin(\theta_P - \theta_0)\left(\frac{s}{r_0} + \frac{v_a}{v_r}\log\left(\frac{r}{v_r t + r_0}\right)\right) + s\kappa_{\max}\sin\left(\frac{\theta_P - \theta_0}{2}\right) \tag{2.45}$$

We denote $\boldsymbol{r} = r_x \boldsymbol{i} + r_y \boldsymbol{j}$, then:

$$r_x(s,t) = s\cos\theta_0 \tag{2.46}$$

$$r_y(s,t) = s\sin\theta_0 - \frac{4}{3}\frac{\rho g}{E}\cos^2\theta_0\left(\frac{v_a}{v_r}\right)^4\left[\frac{1}{2}r^2\log\left(\frac{r}{r_0}\right) - \frac{1}{4}(r^2-(v_rt+r_0)^2)\right.$$
$$\left. + \frac{r_0^3}{6}\left(\frac{1}{r} + \frac{r}{(v_rt+r_0)^2} - \frac{2}{(v_rt+r_0)}\right) - \frac{2}{3}\left(\frac{v_r}{v_a}\right)^2 s^2 - \frac{1}{2}(v_rt+r_0)\left(r - \frac{v_r}{v_a}s\right)\log\left(\frac{v_rt+r_0}{r_0}\right)\right]$$
$$+ 2\alpha\cos\theta_0\sin(\theta_P-\theta_0)\left(\frac{s^2}{2r_0} - \left(\frac{v_a}{v_r}\right)^2 r\log\left(\frac{r}{v_rt+r_0}\right) - \frac{v_a}{v_r}s\right) + \frac{s^2}{2}\cos\theta_0\ \kappa_{\max}\sin\left(\frac{\theta_P-\theta_0}{2}\right) \tag{2.47}$$

2.6.2 Analysis of the exact solutions

Comparison with the classical rod theory

We now compare the solutions obtained for a straight rod ($\kappa^\circ = 0$) with those given by the classical rod theory and in the case of the absence of secondary growth. With the classical rod theory ($\kappa^* = 0$) we find :

$$\bar{\kappa}(s,t) = -\frac{1}{3}\frac{\rho g}{E}\cos\theta_0\left(\frac{v_a}{v_r}\right)^2\left(1 - 4\frac{r_0^3}{r^3} + 3\frac{r_0^4}{r^4}\right) \tag{2.48}$$

$$\bar{\theta}(s,t) = \theta_0 - \frac{1}{3}\frac{\rho g}{E}\cos\theta_0\left(\frac{v_a}{v_r}\right)^3\left[\frac{v_r}{v_a}s - 2r_0^3\left(\frac{1}{r^2} - \frac{1}{(v_rt+r_0)^2}\right) + r_0^4\left(\frac{1}{r^3} - \frac{1}{(v_rt+r_0)^3}\right)\right] \tag{2.49}$$

$$\bar{r}_y(s,t) = s\sin\theta_0 - \frac{1}{3}\frac{\rho g}{E}\cos^2\theta_0\left(\frac{v_a}{v_r}\right)^4\left[\frac{1}{2}\left(\frac{v_r}{v_a}\right)^2 s^2 - 2r_0^3\left(\frac{1}{r} + \frac{r}{(v_rt+r_0)^2} - \frac{2}{(v_rt+r_0)}\right)\right. \tag{2.50}$$
$$\left. + r_0^4\left(\frac{1}{2}\frac{1}{r^2} + \frac{r}{(v_rt+r_0)^3} - \frac{3}{2}\frac{1}{(v_rt+r_0)^2}\right)\right] \tag{2.51}$$

In the absence of secondary growth ($v_r = 0$) the classical solutions are given by:

$$\tilde{m}(s,t) = -\frac{1}{2}\rho g\pi\cos\theta_0(v_at-s)^2 r_0^2 \tag{2.52}$$

$$\tilde{\kappa}(s,t) = -2\frac{\rho g}{E}\cos\theta_0\frac{(v_at-s)^2}{r_0^2} \tag{2.53}$$

$$\tilde{\theta}(s,t) = \theta_0 - \frac{2}{3}\frac{\rho g}{E}\cos\theta_0\frac{(L(t)^3-(v_at-s)^3)}{r_0^2} \tag{2.54}$$

$$\tilde{r}_y(s,t) = s\sin\theta_0 - \frac{2}{3}\frac{\rho g}{E}\cos^2\theta_0\frac{1}{r_0^2}\left[\frac{1}{4}(L(t)-s)^4 - \frac{1}{4}L(t)^4 + L(t)^3 s\right] \tag{2.55}$$

By setting $\alpha = 0$ and $\kappa_{\max} = 0$ (see table 2.1 for the value of the other parameters), the current configuration obtained with our theoretical framework ($\boldsymbol{r}$) is compared with the rod shape provided by the classical rod theory ($\bar{\boldsymbol{r}}$) at $t = 6$ years (see figure 2.5). The rod deflection when secondary growth is neglected ($\tilde{\boldsymbol{r}}$) is also provided. From these results, it appears that the classical rod theory tends to underestimate the rod deflection comparing to the deflection obtained with the surface growth framework. This result is in accordance with previous published works (see [16] for instance) and is explained by remodelling phenomena, i.e. unstrained material points are formed on successive deformed configurations. The classical rod theory gives an upper bound of the solution obtained from the present growth model. The deflection of the rod without secondary growth is obviously much higher due to smaller cross-sections and gives a lower bound of the solution obtained in the present mathematical framework.

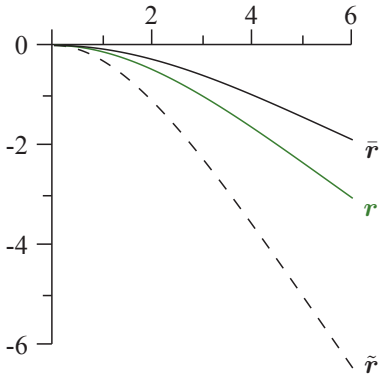

Fig. 2.5: Comparison of the solutions of a growing rod at $t = 6$ years. The black curve $\bar{\boldsymbol{r}}$ represents the current configuration given by the classical rod theory, the green curve $\boldsymbol{r}$ represents the current configuration obtained with the present framework and the dashed curve $\tilde{\boldsymbol{r}}$ gives the current configuration without secondary growth. X-axis and Y-axis correspond to the horizontal and vertical distance (m).

Parameter	Unit	$\boldsymbol{r}$	$\boldsymbol{r}_a$	$\boldsymbol{r}_b$	$\boldsymbol{r}_c$	$\boldsymbol{r}_d$	$\boldsymbol{r}_e$	$\boldsymbol{r}_f$
α	def (m/m)	0	0.001	0	0.001	0	0.001	0.001
$\kappa_{\max}$	m^{-1}	0	0	0.2	0	0.2	0	0.2
v_r	m/y	0.001	0.01	0.005	0.0023	0.001	0.001	0.001
θ_0	rad	0	0	0	0	0	0	0
θ_P	rad	–	$\frac{\pi}{2}$	$\frac{\pi}{2}$	$\frac{\pi}{2}$	$\frac{\pi}{2}$	$\frac{\pi}{2}$	$\frac{\pi}{2}$
v_a	m/y	1.0	1.0	1.0	1.0	1.0	1.0	1.0
r_0	m	0.01	0.01	0.01	0.01	0.01	0.01	0.01
ρ	$\mathrm{kg/m}^3$	1000	1000	1000	1000	1000	1000	1000
g	N/kg	10	10	10	10	10	10	10
E	Pa	10^{10}	10^{10}	10^{10}	10^{10}	10^{10}	10^{10}	10^{10}

Tab. 2.1: Parameter values used to compute the different configurations presented in figures 2.5, 2.6, 2.7 and 2.8. These parameters are taken in [14, 16, 27].

Comparison of growth strategies involved in negative gravitropic response

As trees are subjected to their self-weight, they have to induce a negative gravitropic response to maintain their verticality [1]. The control of the reorientation involves two mechanisms: 1 – a differential growth of shoot apical meristem and 2 – the formation of reaction wood that induces DMS during the secondary growth [4]. The straightening up of branches is the result of a complex combination of these two processes at different time scales [29, 30]. Considering relations (2.37) and (2.39), the effects of primary and secondary tropism are analysed in the case of gravitropic response using the exact solutions calculated at 2.6.1. We set $\theta_0 = 0$ and $\theta_P = \pi/2$ (see table 2.1), and we compare the kinetics of the growing branch for each of the two mechanisms (see figure 2.6) with different values of radial growth velocity v_r.

Simulated shapes in figures 2.6(a) and 2.6(c) are obtained only considering DMS ($\alpha \neq 0$, $\kappa_{\max} = 0$) whereas shapes in figures 2.6(b) and 2.6(d) result from a primary reorientation of the shoot tip that does not involve DMS ($\alpha = 0$, $\kappa_{\max} \neq 0$). Figure 2.6(e) presents the kinetics of a growing rod without reorientation process, like branches of a weeping willow. The simulated growing branches in figures 2.6(a) and 2.6(b) are characterized by a straightened shape due to a moderate secondary growth which increases the rod stiffness. However, a close comparison between

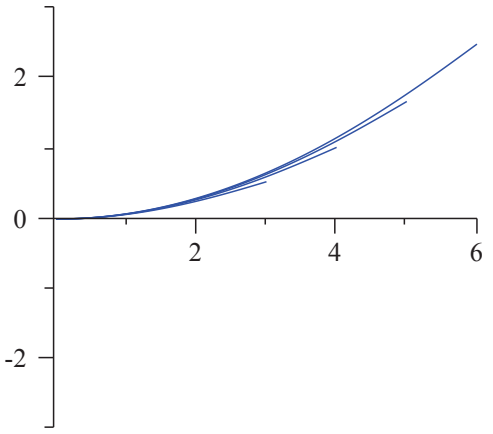

(a) Motion of the current configuration $\boldsymbol{r}_a$ with secondary negative gravitropism only (α=0.001, $\kappa_{\max}$=0 and v_r=0.01).

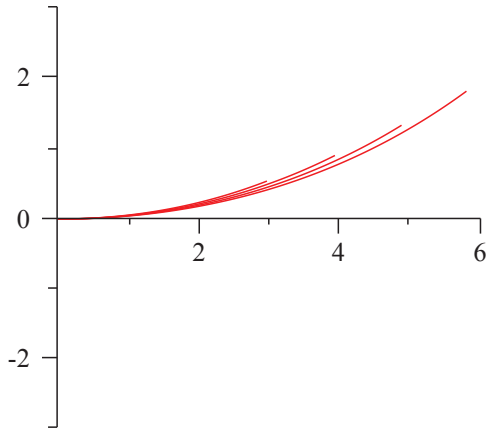

(b) Motion of the current configuration $\boldsymbol{r}_b$ with primary negative gravitropism only (α=0, $\kappa_{\max}$=0.2 and v_r=0.005).

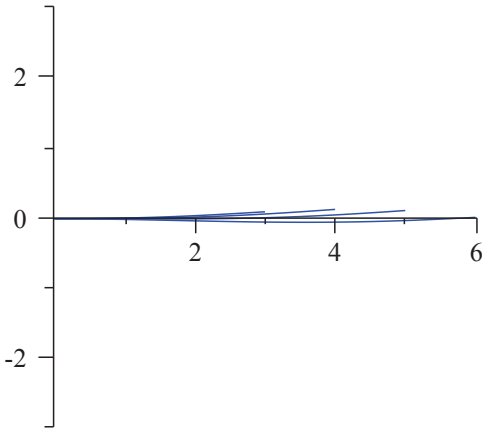

(c) Motion of the current configuration $\boldsymbol{r}_c$ with secondary negative gravitropism only (α=0.001, $\kappa_{\max}$=0, v_r=0.0023).

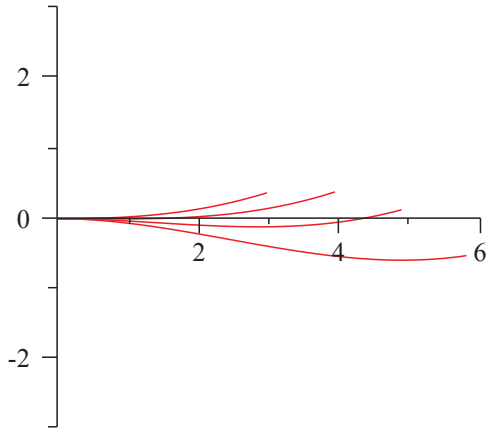

(d) Motion of the current configuration $\boldsymbol{r}_d$ with primary negative gravitropism only (α=0, $\kappa_{\max}$=0.2 and v_r=0.001).

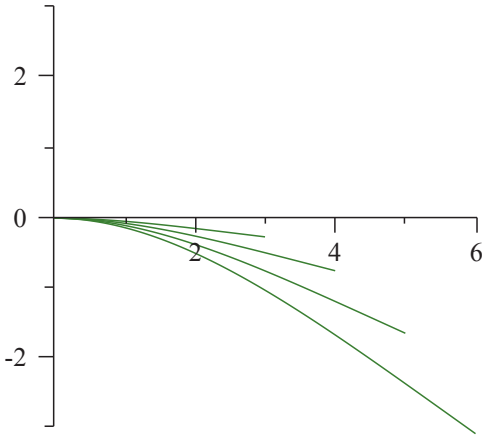

(e) Motion of the current configuration $\boldsymbol{r}$ without negative gravitropism (α=0, $\kappa_{\max}$=0 and v_r=0.001).

Fig. 2.6: Comparison of the kinetics of the two mechanisms involved in the gravitropic response of a growing branch with respect to different values of the radial growth velocity v_r (m/y). The motion of the current configurations is calculated using the exact solutions of a growing rod at time $t = 3, 4, 5$ and 6 years. X-axis and Y-axis correspond to the horizontal and vertical distance (m).

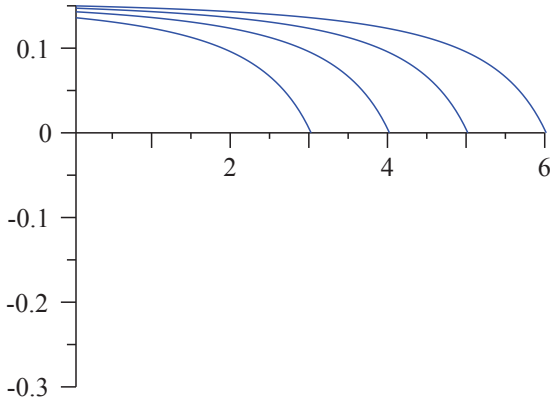

(a) Curvature κ_a of the current configuration $\boldsymbol{r}_a$ with secondary negative gravitropism only (α=0.001, $\kappa_{\max}$=0 and v_r=0.01).

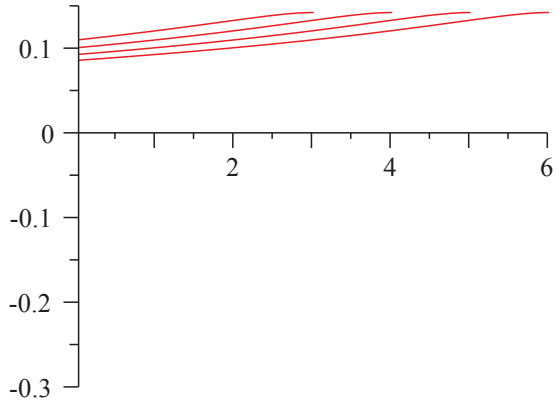

(b) Curvature κ_b of the current configuration $\boldsymbol{r}_b$ with primary negative gravitropism only (α=0, $\kappa_{\max}$=0.2 and v_r=0.005).

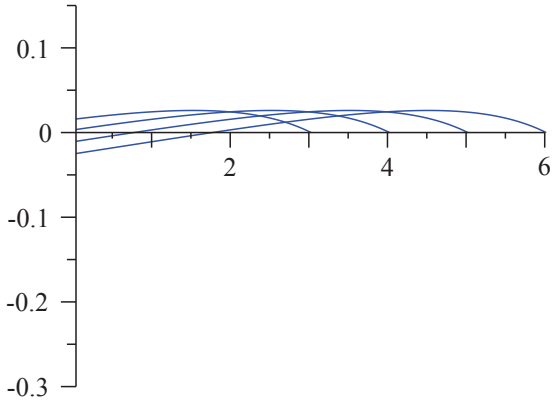

(c) Curvature κ_c of the current configuration $\boldsymbol{r}_c$ with secondary negative gravitropism only (α=0.001, $\kappa_{\max}$=0, v_r=0.0023).

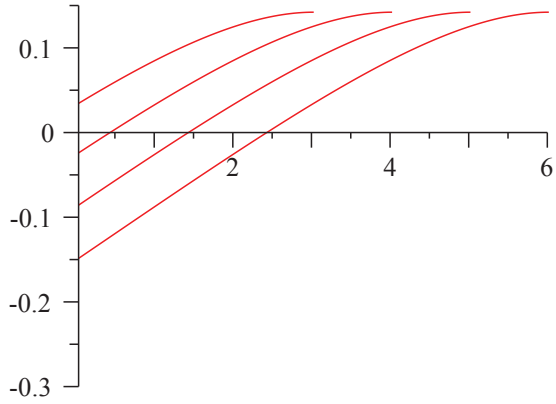

(d) Curvature κ_d of the current configuration $\boldsymbol{r}_d$ with primary negative gravitropism only (α=0, $\kappa_{\max}$=0.2 and v_r=0.001).

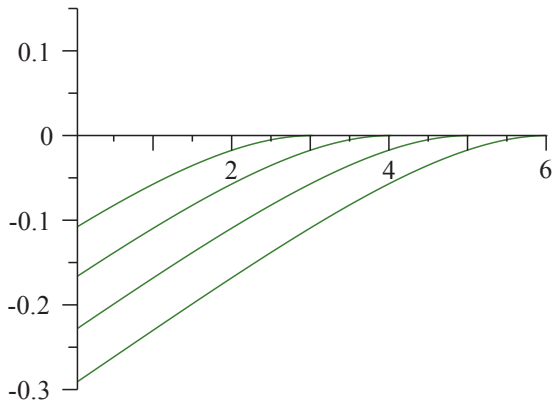

(e) Curvature κ of the current configuration $\boldsymbol{r}$ without negative gravitropism (α=0, $\kappa_{\max}$=0 and v_r=0.001).

Fig. 2.7: Comparison of the curvatures of the current configurations shown in figure 2.6. The curvatures are calculated using the exact solutions of a growing rod at time $t = 3, 4, 5$ and 6 years. X-axis corresponds to the arc-length (m); Y-axis corresponds to the rod curvature (m^{-1}).

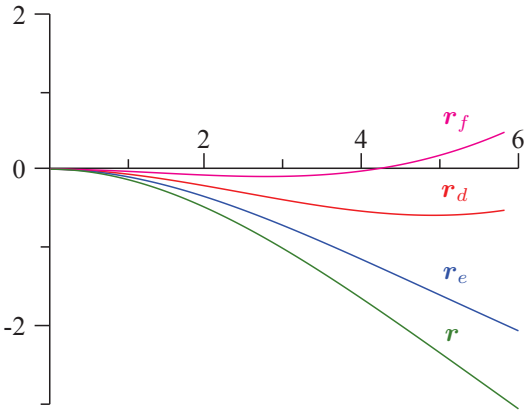

(a) Current configurations $\boldsymbol{r}$ (α=$\kappa_{\max}$=0), $\boldsymbol{r}_d$ (α=0 and $\kappa_{\max}$=0.2), $\boldsymbol{r}_e$ (α =0.001 and $\kappa_{\max}$=0) and $\boldsymbol{r}_f$ (α=0.001, $\kappa_{\max}$=0.2). X-axis and Y-axis correspond to horizontal and vertical distance (m).

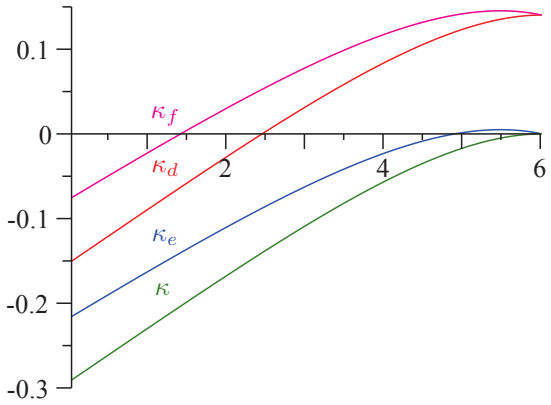

(b) Curvatures $\kappa, \kappa_d, \kappa_e$ and κ_f of the current configurations $\boldsymbol{r}, \boldsymbol{r}_d, \boldsymbol{r}_e$ and $\boldsymbol{r}_f$. X-axis corresponds to the arc-length (m); Y-axis corresponds to the rod curvature (m^{-1}).

Fig. 2.8: Comparison of the effects of the two mechanisms involved in the gravitropic response of a growing branch, i.e. the reorientation of the apical meristem ($\kappa_{\max}$ in m^{-1}) and DMS (α). Current configurations and curvatures along the arc-length (m) are given at time $t = 6$ years.

the evolution of these two configurations reveals that $\boldsymbol{r}_a$ straights up at each time whereas $\boldsymbol{r}_b$ bends slowly downward. Thus, it appears that the formation of reaction wood is a necessary process to straight up a branch vertically. Such simulated shapes correspond to orthotropic branches found in several tree architectural models, e.g. Rauh's model (see [31]). Branch shapes obtained in figures 2.6(c) and 2.6(d) are more horizontal and result from a lower secondary growth. The formation of reaction wood in $\boldsymbol{r}_c$ or the primary reorientation of $\boldsymbol{r}_d$ are sufficient here to compensate for the self-weight increase (see [32]). Such plagiotropic branches are found for instance in trees belonging to Massart's model [31] and provide efficient light interception. The examples above highlight different tree growth strategies that could be achieved with the two mechanisms involved in the gravitropic response and that depend on the radial growth velocity.

The analysis of the effects of primary and secondary tropisms on branch shape is completed by comparing the evolution of the curvatures in each current configuration (see figure 2.7). Figures 2.7(a) and 2.7(b) do not exhibit negative curvatures. However, at a fixed arc-length, we observe that the curvature is increasing in time in the case of reaction wood formation whereas it decreases in the case of primary tropism. Nevertheless, the mechanical responses of growing branches are very different since the maximum of curvature is found at the basal part of the axis (where the diameter is larger) in the case of secondary tropism, while it is located at the apex in the case of primary tropism, for all simulation times. This observation is less contrasted when looking at figures 2.7(c) and 2.7(d), where the simulations took into consideration a lower secondary growth. In the case of secondary tropism, it appears that the curvature is always decreasing with time, except at a certain distance of the axis tip, where a maximum is reached. The maximum value of curvatures in figures 2.7(b) and 2.7(d) is defined by the initial condition in equation (2.41), i.e. $\kappa_{\max}\sqrt{2}/2 \approx 0.1414\ \mathrm{m}^{-1}$. When tropisms are not considered (see figure 2.7(e)) the successive configurations exhibit a negative curvature that decreases with time.

Finally, the respective effects of primary and secondary negative gravitropism with a fixed radial growth velocity are given in figures 2.8(a) and 2.8(b). We can see in figure 2.8(a) that primary and secondary tropisms are complementary involved in the straightening up process. As mentioned above, the reorientation of the shoot tip increases the curvature at the end of the branch, whereas the formation of reaction wood increases the curvature at its base. Moreover the evolution of

the curvature is not monotonic, with a maximum value observed close to the branch tip (see figure 2.8(b)). The results above show that the mathematical model, developed in a suitable mathematical framework, is able to reproduce the main developmental and adaptative processes involved in tree growth.

2.7 Conclusion

In this paper, a mathematical framework has been developed in order to model surface growth processes, extending the classical rod theory to growing structures. One of the major difficulties encountered was the definition of a growing reference configuration representing the primary growth path. This information takes into account the genotypic aspects of tree growth, as well as the apical reorientations induced in response to the local environment. This last component, which defines part of the shape of the reference configuration, takes into account information provided in the current configuration. The identification of the specific basic set in space-time was also a key element to deal with a base curve extending in time. The changing in the material and geometrical properties of the rod due to secondary growth (remodelling), was considered through a dynamic equation modelling the evolution of the relaxed configuration. In the case of woody plants, the effects of DMS, resulting from the formation of reaction wood, have been modelled with a modification of the evolution equation in the relaxed configuration. This work is particularly suited to model the interactions between growth and biomechanics in tree shape analysis. Furthermore, this contribution is currently the only one that allows the calculation of exact solutions in simple cases. Numerical schemes, based on the discretization of system (2.33) with initial-boundary conditions as given by (2.34), will be developed in a next stage. Numerical simulations will allow going further in the analysis of more complex 3-dimensional cases, with a particular focus on the feedback between the current configuration and the reference configuration. A new mathematical challenge would be also to show the existence and uniqueness of a solution, arising from the original initial-boundary problem (2.33) and (2.34).

Acknowledgements

Thanks are due to the Agropolis Fondation (http://www.agropolis-fondation.fr) which supported this research work. AMAP (Botany and Computational Plant Architecture, http://amap.cirad.fr/) is a joint research unit which associates CIRAD (UMR51), CNRS (UMR5120), INRA (UMR931), IRD (2M123), and Montpellier 2 University (UM27).

2.8 Appendix

2.8.1 Notations

s	Arc-length in the reference configuration.
t	Time.
$L(t)$	Length of the base curve of the rod in the reference configuration at time t.
$\gamma(s)$	Date of appearance of the material cross-section at arc-length s.
$\mathcal{Q}$	Basic set in space-time defining all admissible arc-length at each time.
$\boldsymbol{r}^\circ$	Base curve of the rod in the reference configuration.
$\boldsymbol{r}^*$	Base curve of the rod in the relaxed configuration.
$\boldsymbol{r}$	Base curve of the rod in the current configuration.
$(\boldsymbol{i}, \boldsymbol{j}, \boldsymbol{k})$	Orthonormal basis of the euclidean space.
$(\boldsymbol{d}_1^\circ, \boldsymbol{d}_2^\circ, \boldsymbol{d}_3^\circ)$	Orthonormal basis giving the orientation of the cross-sections in the reference configuration (corresponding to the Serret-Frenet frame defined from $\boldsymbol{r}^\circ$).
$(\boldsymbol{d}_1^*, \boldsymbol{d}_2^*, \boldsymbol{d}_3^*)$	Orthonormal basis giving the orientation of the cross-sections in the relaxed configuration.
$(\boldsymbol{d}_1, \boldsymbol{d}_2, \boldsymbol{d}_3)$	Orthonormal basis giving the orientation of the cross-sections in the current configuration.
κ°	Curvature of the base curve in the reference configuration.
τ°	Torsion of the base curve in the reference configuration.
$\boldsymbol{u}^\circ$	Strain vector related to bending and torsion in the reference configuration.
$\boldsymbol{u}^*$	Strain vector related to bending and torsion in the relaxed configuration.
$\boldsymbol{u}$	Strain vector related to bending and torsion in the current configuration.
$\mathbf{u}^\circ$	$= (0, \kappa^\circ, \tau^\circ)$. Components of $\boldsymbol{u}^\circ$ in the local basis $(\boldsymbol{d}_i^\circ)_{i=1,2,3}$.
$\mathbf{u}^*$	$= (u_1^*, u_2^*, u_3^*)$. Components of $\boldsymbol{u}^*$ in the local basis $(\boldsymbol{d}_i^*)_{i=1,2,3}$.
$\mathbf{u}$	$= (u_1, u_2, u_3)$. Components of $\boldsymbol{u}$ in the local basis $(\boldsymbol{d}_i)_{i=1,2,3}$.
$\boldsymbol{v}^\circ$	Strain vector related to shear and extension in the reference configuration.
$\boldsymbol{v}^*$	Strain vector related to shear and extension in the relaxed configuration.
$\boldsymbol{v}$	Strain vector related to shear and extension in the current configuration.
$\mathbf{v}^\circ$	$= (0, 0, 1)$. Components of $\boldsymbol{v}^\circ$ in the local basis $(\boldsymbol{d}_i^\circ)_{i=1,2,3}$.
$\mathbf{v}^*$	$= (v_1^*, v_2^*, v_3^*)$. Components of $\boldsymbol{v}^*$ in the local basis $(\boldsymbol{d}_i^*)_{i=1,2,3}$.
$\mathbf{v}$	$= (v_1, u_2, v_3)$. Components of $\boldsymbol{v}$ in the local basis $(\boldsymbol{d}_i)_{i=1,2,3}$.
$\boldsymbol{f}$	Body force per unit length of the base curve in the reference configuration.
$\boldsymbol{l}$	Body couple per unit length of the base curve in the reference configuration.
$\boldsymbol{n}$	Contact force vector.
$\boldsymbol{m}$	Contact couple vector.
$\mathbf{n}$	$= (n_1, n_2, n_3)$. Components of $\boldsymbol{n}$ in the local basis $(\boldsymbol{d}_i)_{i=1,2,3}$.
$\mathbf{m}$	$= (m_1, m_2, m_3)$. Components of $\boldsymbol{m}$ in the local basis $(\boldsymbol{d}_i)_{i=1,2,3}$.
$\hat{\mathbf{n}}$	Constitutive relation for $\mathbf{n}$.
$\hat{\mathbf{m}}$	Constitutive relation for $\mathbf{m}$.
$\hat{\mathbf{u}}$	Constitutive relation for $\mathbf{u}$.
$\hat{\mathbf{v}}$	Constitutive relation for $\mathbf{v}$.
v_a	Apical growth velocity.
v_r	Radial growth velocity.
$r(s,t)$	Radius of the cross-section at s and at time t .
$A(s,t)$	Area of the cross-section at s and at time t.
$I(s,t)$	Geometrical moment of inertia of the cross-section at s and at time t.
E	Constant Young's modulus.

References

[1] M. Fournier, A. Stokes, C. Coutand, T. Fourcaud, B. Moulia, Ecology and biomechanics : a mechanical approach to the ecology of animals and plants, CRC Taylor and Francis, 2006, Ch. 1 : Tree Biomechanics and Growth Strategies in the Context of Forest Functional Ecology, pp. 1–33.

[2] T. Fourcaud, X. Zhang, A. Stokes, H. Lambers, C. Körner, Plant growth modelling and applications: The increasing importance of plant architecture in growth models, Annals of Botany 101 (2008) 1053–1063.

[3] C. Plomion, G. Leprovost, A. Stokes, Wood formation in trees, Plant Physiology 127 (2001) 1513–1523.

[4] B. Moulia, C. Coutand, C. Lenne, Posture control and skeletal mechanical acclimation in terrestrial plants: Implication for mechanical modeling of plant architecture, American Journal of Botany 93 (2006) 1477–1489.

[5] R. R. Archer, On the origin of growth stresses in trees, Wood Science and Technology 23 (4) (1989) 311–322.

[6] M. Fournier, H. Bailleres, B. Chanson, Tree biomechanics: Growth, cumulative prestresses, and reorientations, Biomimetics 2 (1994) 229–251.

[7] R. Skalak, G. Dasgupta, M. Moss, Analytical description of growth, Journal of theoretical Biology 94 (1982) 555–577.

[8] L. A. Taber, Biomechanics of growth, remodeling, and morphogenesis, Applied Mechanics Reviews 48 (1995) 487–545.

[9] R. Skalak, D. A. Farrow, A. Hoger, Kinematics of surface growth, Journal of Mathematical Biology 35 (1997) 869–907.

[10] D. Ambrosi, F. Mollica, On the mechanics of a growing tumor, International Journal of Engineering Science 40 (2002) 1297–1316.

[11] D. Ambrosi, G. Ateshian, E. Arruda, S. Cowin, J. Dumais, A. Goriely, G. Holzapfel, J. Humphrey, R. Kemkemer, E. Kuhl, Perspectives on biological growth and remodeling, Journal of the Mechanics and Physics of Solids 59 (4) (2011) 863–883.

[12] G. A. Ateshian, On the theory of reactive mixtures for modeling biological growth, Biomechanics and Modeling in Mechanobiology 6 (2007) 423–445.

[13] N. Hodge, P. Papadopoulos, A continuum theory of surface growth, Proceedings of the Royal Society of London A 466 (2010) 3135–3152.

[14] H. Yamamoto, M. Yoshida, T. Okuyama, Growth stress controls negative gravitropism in woody plant stem, Planta 216 (2002) 280–292.

[15] T. Fourcaud, P. Lac, Numerical modelling of shape regulation and growth stresses in trees. part i: An incremental static finite element formulation, Trees 17 (2003) 23–30.

[16] T. Fourcaud, F. Blaise, P. Lac, P. Castéra, P. de Reffye, Numerical modelling of shape regulation and growth stresses in trees. part ii: implementation in the amappara software and simulation of tree growth, Trees 17 (2003) 31–39.

[17] A. Goriely, M. Robertson-Tessi, M. Tabor, R. Vandiver, Mathematical Modelling of Biosystems, Vol. 102, Springer Berlin Heidelberg, 2008, Ch. 1 : Elastic Growth Models, pp. 1–44.

[18] N. A. Faruk Senan, O. M. O'Reilly, T. N. Tresierras, Modeling the growth and branching of plants: A simple rod-based model, Journal of the Mechanics and Physics of Solids 56 (2008) 3021–3036.

[19] O. M. O'Reilly, T. N. Tresierras, On the evolution of intrinsic curvature in rod-based models of growth in long slender plant stem, International Journal of Solids and Structure 48 (2011) 1239–1247.

[20] S. S. Antman, Nonlinear Problems of Elasticity, Springer, 2005, Ch. 8 : Theory of Rods Deforming in Space, pp. 269–344.

[21] R. W. Ogden, Non-Linear Elastic Deformations, Halsted Press, New York, 1984.

[22] M. Epstein, G. A. Maugin, Thermomechanics of volumetric growth in uniform bodies, International journal of Plasticity 16 (2000) 951–978.

[23] P. Heuret, C. Meredieu, T. Coudurier, F. Courdier, D. Barthélémy, Ontogenetic trends in the morphological features of main stem annual shoots of *Pinus pinaster* (pinaceae), American Journal of Botany 93 (11) (2006) 1577–1587.

[24] B. Moulia, M. Fournier, The power and control of gravitropic movements in plants: a biomechanical and systems biology view, Journal of Experimental Botany 60 (2009) 461–486.

[25] M. J. Jaffe, Thigmomorphogenesis: the response of plant growth and development to mechanical stimulation. with special reference to bryonia dioica., Planta 114 (2) (1973) 143–157.

[26] C. Coutand, Mechanosensing and thigmomorphogenesis, a physiological and biomechanical point of view, Plant Science 179 (3) (2010) 168–182.

[27] T. Alméras, M. Fournier, Biomechanical design and long-term stability of trees: Morphological and wood traits involved in the balance between weight increase and the gravitropic reaction, Journal of theoretical Biology 256 (2009) 370–381.

[28] Y.-S. Huang, L.-F. Hung, L.-L. Kuo-Huang, Biomechanical modeling of gravitropic response of branches: roles of asymmetric periphery growth strain versus self-weight bending effect, Trees 24 (2010) 1151–1161.

[29] R. Sierra-de-Grado, V. Pando, P. Martínez-Zurimendi, A. Peñalvo, E. Báscones, M. B., Biomechanical differences in the stem straightening process among pinus pinaster provenances. a new approach for early selection of stem straightness., Tree Physiology 28 (2008) 835–846.

[30] R. Herrera, C. Krier, C. Lalanne, E. H. M. Ba, A. Stokes, F. Salin, T. Fourcaud, S. Claverol, C. Plomion, (not) keeping the stem straight: a proteomic analysis of maritime pine seedlings undergoing phototropism and gravitropism, BMC Plant Biology 10 (2010) 217.

[31] F. Hallé, R. Oldeman, P. Tomlinson, Tropical trees and forests: an architectural analysis, Springer-Verlag, Berlin, 1978.

[32] P. Castéra, V. Morlier, Growth patterns and bending mechanics of branches, Trees 5 (1991) 232–238.

Chapitre 3

NUMERICAL METHODS FOR THE BIOMECHANICS OF GROWING TREES

Thomas Guillon* Yves Dumont† Thierry Fourcaud†

Abstract

Modelling the biomechanics of growing trees is a non-classical problem, as the usual framework of structural mechanics does not take into account the evolution of the domain geometry due to growth processes. Incremental approaches have been used in rod theory to bypass this problem and to model the addition of new material points on a existing deformed structure. However, these approaches are based on explicit time integration schemes of a unknown continuous model, and thus, the accuracy of the numerical results obtained cannot be analysed. A new continuous space-time formulation has been recently proposed to model the biomechanical response of growing rods. The aim of this paper is to discretize the corresponding system of partial differential equations in order to solve the problem numerically. The finite element method is implemented to compute the space boundary problem and different time integration schemes are considered to solve the associated initial value problem with a special attention to the previously used explicit Euler scheme. The numerical results point out that the accuracy of the time integration schemes strongly depends on the value of the parameters. The explicit Euler method presents errors with significant orders of magnitude. Nevertheless, attention must be paid to implicit methods since, for specific values of the parameters and large time steps, they may lead to spurious solutions that may come from numerical instabilities. Hence, the predictor-corrector Heun's method is an interesting alternative even if it is more time consuming.

Keywords : Plant growth, Rod theory, Boundary initial value problem, Hermite finite element, Predictor-corrector methods.

∗. Université Montpellier II, UMR AMAP, TA-A51/PS2, boulevard de la Lironde, 34398 Montpellier Cedex 5, France

†. CIRAD, UMR AMAP, TA-A51/PS2, boulevard de la Lironde, 34398 Montpellier Cedex 5, France

3.1 Introduction

The analysis of tree growth strategies required an accurate modelling of the interaction between the growth processes and the biomechanical responses of the growing structure [1]. However, the mechanical modelling of surface growth problem exceeds the usual framework used in strength of materials and structural mechanics, since new material points are added to an already existing deformed body at each time of growth [2]. One traditional way to solve the biomechanical problem of growing trees, is to consider an incremental approach [3, 4, 5, 6]. It consists in adding new material layers to the surface of the last known current configuration and computing the effects of the load increment over the new prestressed configuration. However, this approach necessitates to separate the growth process and the mechanical responses of the growing body. Therefore, it is equivalent to an explicit time discretization of an unknown continuous model, and thus, no mathematical analysis can be achieved to test the accuracy of the obtained results.

In a recent work, a mathematical framework has been proposed to model simultaneously the growth and the biomechanics of a rod in continuous time [7]. A new system of partial differential equations was built, considering the dependence between time and space, which is specific to surface growth. One advantage of this continuous formulation of grwoth is that the time-dependent equations can be discretized with any numerical scheme. Moreover, in the case of small deflection, the linearization of the system leads to the calculation of exact solutions which can be used to analyse the accuracy of the numerical simulations.

The present work addresses the discretization of the original system of partial differential equations developed in [7]. Different time integration schemes are compared and the quality of the explicit Euler method, traditionally used in incremental approaches, is discussed. The paper is organised as follow. Section 3.2 recalls the system of partial differential equations previously developed to model the planar motion of a growing rod. A new formulation of these equations is proposed, which exhibits the coupling between a boundary value problem and an initial value problem. Section 3.3 is concerned with the discretization of the coupled problem using the finite element method in conjunction with different time integration schemes. Numerical experiments are analysed in Section 3.4 and reveal the importance of a mathematical framework to analyse the accuracy of the numerical solution for each time integration scheme. Conclusions about the quality of the numerical schemes are presented in Section 3.5.

3.2 The mathematical model

This section recalls the system of partial differential equations that has been developed to model the biomechanics of a growing rod [7]. The geometrical implications of the growth process are first considered. Then, different mathematical formulations of the planar motion of an inextensible and unshearable growing rod are analysed.

3.2.1 The geometrical description of growth

A growing rod is characterized by the evolution of its length (primary growth) and the diameter of its cross-sections (secondary growth) at each time.

The length of the rod at time t is denoted $L(t)$ and is assumed to be a strictly increasing function in time. Then the inverse function $\gamma(s)$ gives the date of appearance of a material point at arc-length s. The derivative of the length corresponds to the apical growth velocity and is given by $v_a = \mathrm{d}L/\mathrm{d}t > 0$. Therefore, the basic set of all admissible material points at each time is defined by (see figure 3.1(a)):

$$Q = \Big\{(s,t)/t \in \mathbb{R}^+, s \in [0, L(t)]\Big\} \tag{3.1}$$

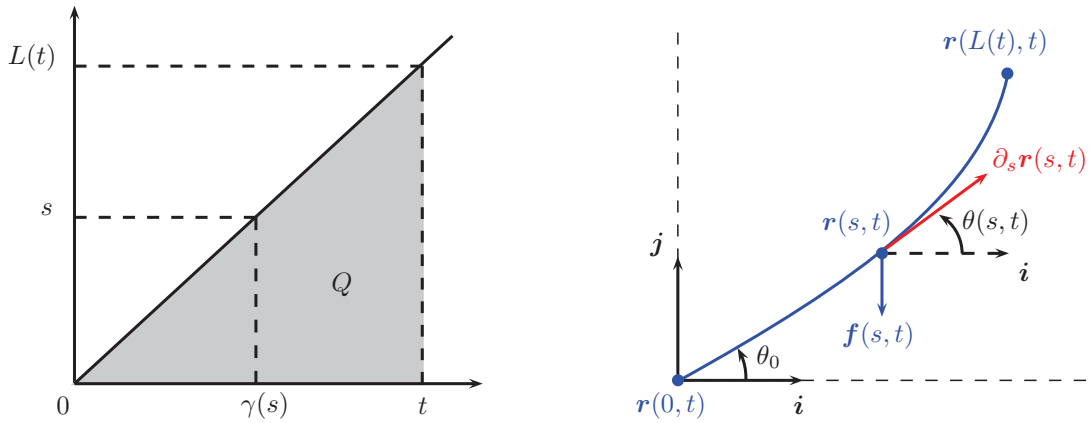

(a) Representation of the basic set Q with length L as a linear function in time. The inverse function $\gamma(s)$ gives the date of appearance of a material point located at arc-length s.

(b) Planar motion of an inextensible and unshearable growing rod subjected to its self-weight $\boldsymbol{f}$. The current configuration is represented by $\boldsymbol{r}$. θ is the angle between $\boldsymbol{i}$ and $\partial_s \boldsymbol{r}$.

Fig. 3.1: The basic set of all admissible material points and the planar motion of a growing rod.

where s is the arc-length parametrization. This set points out that space and time are not independent in the modelling of the biomechanics of a growing rod. As a result, the mechanical equilibrium of the rod has to be computed at each time t on an increasing domain given by $[0, L(t)]$. To complete this description, we can notice that at each time t, the basic set Q contains the boundary points $(0, t)$ and $(L(t), t)$ representing the two ends of the rod, whereas at an arc-length s the point $(s, \gamma(s)) \in Q$ may represent an initial condition at the date of appearance of the cross-section located at s.

For the sake of simplicity, the cross-sections of the rod are assumed to be circular with a radius r solution of the following initial value problem for $(s, t) \in Q$:

$$\begin{aligned} \partial_t r(s,t) &= v_r(s,t) \\ r(s,\gamma(s)) &= r_0(s) \end{aligned} \tag{3.2}$$

where v_r is the radial growth velocity and $r_0 > 0$ is the initial radius of the cross-section at its date of appearance (i.e. the radius of the primary meristem).

3.2.2 Planar motion of a growing stem

We consider the motion in the Euclidean plane $(\boldsymbol{i}, \boldsymbol{j})$ of an inextensible and unshearable growing rod subjected to body force per unit length $\boldsymbol{f}$. We assume that the growth starts with the angle θ_0 from $\boldsymbol{i}$, and we denote θ the angle between $\boldsymbol{i}$ and the tangent of the current configuration $\boldsymbol{r}$ (see figure 3.1(b)).

The system

The initial-boundary problem modelling the biomechanics of a growing rod is given as follows for $(s,t) \in Q$:

$$\partial_s n_x = -f_x \tag{3.3}$$
$$\partial_s n_y = -f_y \tag{3.4}$$
$$\partial_s m = n_x \sin\theta - n_y \cos\theta \tag{3.5}$$
$$\partial_t \kappa^* = \frac{\partial_t EI}{(EI)^2} m + p \tag{3.6}$$
$$\partial_s \theta = \kappa^* + \frac{m}{EI} \tag{3.7}$$
$$\partial_s \boldsymbol{r} = \cos\theta \boldsymbol{i} + \sin\theta \boldsymbol{j} \tag{3.8}$$

with the initial-boundary conditions :

$$n_x(L(t),t) = 0 \tag{3.9}$$
$$n_y(L(t),t) = 0 \tag{3.10}$$
$$m(L(t),t) = 0 \tag{3.11}$$
$$\kappa^*(s,\gamma(s)) = \kappa^\circ(s) \tag{3.12}$$
$$\theta(0,t) = \theta_0 \tag{3.13}$$
$$\boldsymbol{r}(0,t) = \boldsymbol{0} \tag{3.14}$$

where equations (3.3),(3.4) and (3.5) correspond to the quasi-static balance equations, in which $\boldsymbol{n} = n_x \boldsymbol{i} + n_y \boldsymbol{j}$ is the contact force and m the moment. Then, equation (3.6) represents the evolution of the curvature in the relaxed configuration due to the remodelling effects of growth [7]. Equation (3.7) corresponds to the linear constitutive relation for an inextensible and unshearable rod, with E the Young's modulus and $I(s,t) = \pi r^4(s,t)/4$ the geometrical moment of inertia of the cross-section at s and at time t. In the following, we will denote $\kappa = \partial_s \theta$ the curvature of the current configuration. Finally, equation (3.8) gives the position of the cross-sections in the current configuration.

In addition, the function p in (3.6) has been introduced to take into account changes in curvature induced by a differential in maturation strains of wood cells [8] which is related to secondary tropism of lignified axes. Assuming that reorientation processes occur with a fixed preferential angle θ_P, the tropism function can be expressed as in [3]:

$$p = 2\frac{v_r}{r^2}\alpha \sin(\theta_P - \theta) \tag{3.15}$$

where α is the maximum differential in maturation strains between normal and reaction wood. Next, the function κ° in (3.12) defines the initial curvature of the cross-section at its date of appearance and is related to primary tropism. We use the following relation [7]:

$$\kappa^\circ(s) = \kappa_{\max} \sin\left(\frac{\theta_P - \theta(s,\gamma(s))}{2}\right) \tag{3.16}$$

where $\kappa_{\max}$ is the maximum curvature induced by primary growth. We have also:

$$\frac{\mathrm{d}\kappa^\circ}{\mathrm{d}s}(s) = \kappa_{\max}^2 \left(\frac{1}{2}\sin(\theta_P - \theta(s,\gamma(s))) - \sin\left(\frac{\theta_P - \theta(s,\gamma(s))}{2}\right)\right) \tag{3.17}$$

Coupling a boundary problem to an initial value problem

As the equations (3.3),(3.4) and (3.8) can be easily solved by numerical integration, the above system can be reduced. Moreover, substituting m in (3.6) by (3.7) and differentiating equation (3.7) with respect to the arc-length s combined with the equation (3.5), we get the following coupled problem:

$$\begin{cases} \partial_s(EI\partial_s\theta) - n_x\sin\theta + n_y\cos\theta = \partial_s(EI\kappa^*) \\ \partial_t\kappa^* = \dfrac{\partial_t EI}{EI}(\kappa - \kappa^*) + p \end{cases} \tag{3.18}$$

with the initial-boundary conditions :

$$\begin{cases} \theta(0,t) = \theta_0 \\ \kappa(L(t),t) = \kappa^\circ(L(t)) \\ \kappa^*(s,\gamma(s)) = \kappa^\circ(s) \end{cases} \tag{3.19}$$

Thus, we obtain a second order boundary problem for θ, coupled to a first order initial value problem for κ^*. We can notice that the first equation of the problem (3.18) is equivalent to the usual two-dimensional non-linear rod equilibrium equation [9] with an additional contact force taking into account the effects of the remodelling, i.e. changes in material and geometrical properties of the rod due to the growth process.

Weak formulation of the boundary problem

We now consider the weak formulation of the boundary value problem (BVP). We first observe that the continuity of $\kappa = \partial_s\theta$ is required to integrate properly the initial value problem in (3.18). Thus, for $t \in [0,T]$ we define $\mathcal{V}^t$ such that:

$$\mathcal{V}^t = \Big\{ v \in H^2\big([0,L(t)]\big) / v(0) = 0 \Big\}$$

Then, by denoting $\beta = \theta - \theta_0$, the weak form is given by finding $\beta(\cdot,t) \in \mathcal{V}^t$ such that, for all $v \in \mathcal{V}^t$:

$$\int_0^{L(t)} EI\partial_s\beta\frac{\mathrm{d}v}{\mathrm{d}s}\mathrm{d}s + \int_0^{L(t)} \big(n_x\sin(\theta_0+\beta) - n_y\cos(\theta_0+\beta)\big)v\mathrm{d}s = \int_0^{L(t)} EI\kappa^*\frac{\mathrm{d}v}{\mathrm{d}s}\mathrm{d}s \tag{3.20}$$

It is important to notice that this formulation is different at each time, since the domain $[0,L(t)]$ is increasing. Moreover, the partial derivative of κ^* with respect to s will be required to estimate numerically the right hand side of (3.20). By denoting $\omega = \partial_s\kappa^*$ and taking the partial derivative with respect to s in (3.6), the weak form is coupled to the following initial value problem (IVP):

$$\begin{cases} \partial_t\kappa^* = \dfrac{\partial_t EI}{EI}(\kappa - \kappa^*) + p \\ \partial_t\omega = \left(\dfrac{\partial_{st}EI}{EI} - 2\dfrac{\partial_s EI\partial_t EI}{(EI)^2}\right)(\kappa - \kappa^*) + \dfrac{\partial_t EI}{(EI)^2}\Big(n_x\sin(\theta_0+\beta) - n_y\cos(\theta_0+\beta)\Big) + \partial_s p \\ \kappa^*(s,\gamma(s)) = \kappa^\circ(s) \\ \omega(s,\gamma(s)) = \dfrac{\mathrm{d}\kappa^\circ}{\mathrm{d}s}(s) - \dfrac{p(s,\gamma(s))}{v_a(\gamma(s))} \end{cases} \tag{3.21}$$

where the last initial condition is deduced from the calculation of $\frac{\mathrm{d}}{\mathrm{d}s}(\kappa^*(s,\gamma(s)))$ and:

$$\partial_s p = 2\frac{v_r}{r^2}\alpha\left[\left(\frac{\partial_s v_r}{v_r} - 2\frac{\partial_s r}{r}\right)\sin(\theta_P - \theta_0 - \beta) - \kappa\cos(\theta_P - \theta_0 - \beta)\right]$$

3.3 Discretization

This section is concerned with the discretization of the problem coupling the BVP (3.20) to the IVP (3.21). As explained in section 3.2.1, the basic set Q underlines that time and space are not independent. Therefore, for $T > 0$, a partition $(t^n)_{0\leq n\leq N}$ of $[0, T]$ imposes a partition $(s_i)_{0\leq i\leq n}$ of $[0, L(t^n)]$ at each time step n, such that $s_i = L(t^i) = L^i$ (see figure 3.2(a)). In the following, we assume that $t^n = n\Delta t$ and we denote $h = (h_i)_{1\leq i\leq n}$ the space steps defined by $h_i = s_i - s_{i-1}$. A finite element approximation of the weak form is first established using the cubic Hermite elements. Then, different numerical schemes are considered for the time integration of the initial value problem.

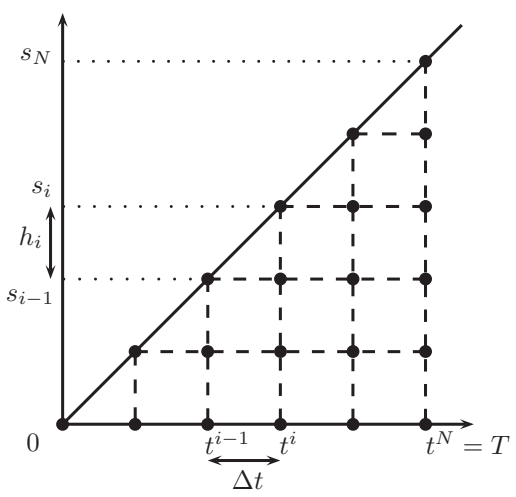

(a) The partition $(t^n)_{0\leq n\leq N}$ of the time interval $[0, T]$ imposes a partition $(s_i)_{0\leq i\leq n}$ of the space interval $[0, L(t^n)]$.

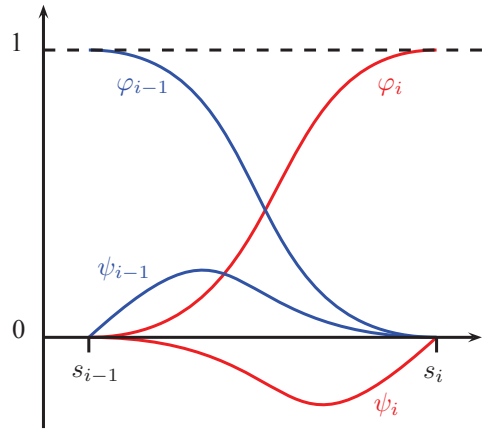

(b) Representation of the shape functions φ_{i-1}, ψ_{i-1}, φ_i and ψ_i characterizing the cubic Hermite element over the interval $[s_{i-1}, s_i]$.

Fig. 3.2: Discretization of the basic set Q and Hermite finite element.

3.3.1 Finite element approximation of the boundary problem

This subsection considers the Hermite finite element to construct a semi-discrete approximation of the boundary problem (3.20). The assemblage procedure is carefully analysed with special attention to the additional term due to the remodelling effects modelled by (3.21).

Hermite finite element

We consider the classical P3 Hermite finite elements which associate at each node s_i, with $0 \leq i \leq N$, two piecewise cubic functions φ_i and ψ_i defined by (see figure 3.2(b) and 3.6.1):

$$\begin{cases} \varphi_i(s_j) = \delta_{ij} \quad \text{and} \quad \dfrac{\mathrm{d}\varphi_i}{\mathrm{d}s}(s_j) = 0 \\ \psi_i(s_j) = 0 \quad \text{and} \quad \dfrac{\mathrm{d}\psi_i}{\mathrm{d}s}(s_j) = \delta_{ij} \end{cases}$$

for $0 \leq j \leq N$. Then, for $1 \leq n \leq N$, we introduce the following finite dimensional subspace:

$$\mathcal{V}_h^n = \mathrm{span}\{\psi_0, \phi_1, \psi_1, \ldots, \varphi_{n-1}, \psi_{n-1}, \varphi_n\} \subset \mathcal{V}^{t^n}$$

The approximation of the unknown functions β^n and κ^{*n} with the Hermite finite elements is given by:

$$\beta_h^n = \sum_{i=1}^{n} \varphi_i \beta_i^n + \psi_i \kappa_i^n$$
$$\kappa_h^{*n} = \sum_{i=0}^{n} \varphi_i {\kappa^*}_i^n + \psi_i \omega_i^n$$

Hence, for $t = t^n$, the BVP (3.20) is rewritten in a discrete form as follows, find $\beta_h^n \in \mathcal{V}_h^n$, such that, for all $v \in \mathcal{V}_h^n$, we have:

$$\begin{aligned} F(\beta_h^n, v) &= \int_0^{L^n} EI^n \partial_s \beta_h^n \frac{\mathrm{d}v}{\mathrm{d}s} \mathrm{d}s + \int_0^{L^n} \Big({n_x}^n \sin\left(\theta_0 + \beta_h^n\right) - {n_y}^n \cos\left(\theta_0 + \beta_h^n\right) \Big) v \mathrm{d}s \\ &\quad - \int_0^{L^n} EI^n \kappa_h^{*n} \frac{\mathrm{d}v}{\mathrm{d}s} \mathrm{d}s \\ &= K(\beta_h^n, v) + M(\beta_h^n, v) - G(\kappa_h^{*n}, v) \\ &= 0 \end{aligned} \tag{3.22}$$

By denoting $\boldsymbol{x}^n$ the vector such that for $0 \leq i \leq n$:

$$x_{2i+1}^n = \beta_i^n$$
$$x_{2i+2}^n = \kappa_i^n$$

the resulting non-linear finite dimensional system of $2N+2$ equations $\boldsymbol{F}^n(\boldsymbol{x}^n) = \boldsymbol{0}$ is deduced from (3.22), in which for $0 \leq i \leq n$:

$$\begin{aligned} F_{2i+1}^n(\boldsymbol{x}^n) &= F(\beta_h^n, \varphi_i) \\ F_{2i+2}^n(\boldsymbol{x}^n) &= F(\beta_h^n, \psi_i) \end{aligned} \tag{3.23}$$

The first and the last equations have to be removed from this system since $\beta_0^n = 0$ and $\kappa_n^n = \kappa^\circ(s_n)$ and we obtain a system of $2N$ equations.

Assemblage of the non-linear system

The assemblage of the previous system is performed by assessing the contribution of each element e_i^n which support is $[s_{i-1}, s_i]$. For $1 \leq i \leq n$, we denote:

$$\begin{aligned} \boldsymbol{N}_i(s) &= \begin{bmatrix} \varphi_{i-1}(s) & \psi_{i-1}(s) & \varphi_i(s) & \psi_i(s) \end{bmatrix}^T \\ \boldsymbol{x}_i^n &= \begin{bmatrix} \beta_{i-1}^n & \kappa_{i-1}^n & \beta_i^n & \kappa_i^n \end{bmatrix}^T \\ \boldsymbol{y}_i^n &= \begin{bmatrix} {\kappa^*}_{i-1}^n & \omega_{i-1}^n & {\kappa^*}_i^n & \omega_i^n \end{bmatrix}^T \end{aligned}$$

Then, the computation of (3.22) for the element e_i^n leads to:

$$\begin{aligned} \boldsymbol{F}^{e_i^n}(\boldsymbol{x}_i^n) &= \int_{s_{i-1}}^{s_i} EI^n \frac{\mathrm{d}\boldsymbol{N}_i^T}{\mathrm{d}s} \boldsymbol{x}_i^n \frac{\mathrm{d}\boldsymbol{N}_i}{\mathrm{d}s} \mathrm{d}s + \int_{s_{i-1}}^{s_i} \Big({n_x}^n \sin\left(\theta_0 + \boldsymbol{N}_i^T \boldsymbol{x}_i^n\right) - {n_y}^n \cos\left(\theta_0 + \boldsymbol{N}_i^T \boldsymbol{x}_i^n\right) \Big) \boldsymbol{N}_i \mathrm{d}s \\ &\quad - \int_{s_{i-1}}^{s_i} EI^n \boldsymbol{N}_i^T \boldsymbol{y}_i^n \frac{\mathrm{d}\boldsymbol{N}_i}{\mathrm{d}s} \mathrm{d}s \\ &= \boldsymbol{K}^{e_i^n}(\boldsymbol{x}_i^n) + \boldsymbol{M}^{e_i^n}(\boldsymbol{x}_i^n) - \boldsymbol{G}^{e_i^n}(\boldsymbol{y}_i^n) \end{aligned} \tag{3.24}$$

So that the equation (3.23) is deduced as follows, for $1 \leq i \leq n-1$:

$$\begin{cases} F_2^n = F_2^{e_1^n} \\ F_{2i+1}^n = F_3^{e_i^n} + F_1^{e_{i+1}^n} \\ F_{2i+2}^n = F_4^{e_i^n} + F_2^{e_{i+1}^n} \\ F_{2n+1}^n = F_3^{e_n^n} \end{cases} \tag{3.25}$$

Each integral in (3.24) is estimated with a Gauss-Legendre quadrature (see 3.6.2). Special attention must be given to the computation of the last element e_n^n because of the boundary condition of κ and the initial conditions of κ^* and ω. More precisely, we have:

$$\begin{aligned} \kappa_n^n &= {\kappa^*}_n^n = \kappa_{\max} \sin\left(\frac{\theta_P - \theta_0 - \beta_n^n}{2}\right) \\ \omega_n^n &= \kappa_{\max}^2 \left(\frac{1}{2}\sin\left(\theta_P - \theta_0 - \beta_n^n\right) - \sin\left(\frac{\theta_P - \theta_0 - \beta_n^n}{2}\right)\right) - \frac{2\alpha}{r_0^2}\frac{{v_r}_n^n}{{v_a}_n^n}\sin\left(\theta_P - \theta_0 - \beta_n^n\right) \end{aligned} \tag{3.26}$$

Assemblage of the Jacobian

In order to solve the non-linear system (3.23) with the Newton method, we need to compute the Jacobian matrix of the vector-valued function $\boldsymbol{F}^n$. This is performed for each element e_i^n:

$$\nabla_{\boldsymbol{x}_i^n} \boldsymbol{F}^{e_i^n}(\boldsymbol{x}_i^n) = \nabla_{\boldsymbol{x}_i^n} \boldsymbol{K}^{e_i^n}(\boldsymbol{x}_i^n) + \nabla_{\boldsymbol{x}_i^n} \boldsymbol{M}^{e_i^n}(\boldsymbol{x}_i^n) - \nabla_{\boldsymbol{x}_i^n} \boldsymbol{G}^{e_i^n}(\boldsymbol{y}_i^n) \tag{3.27}$$

where:

$$\begin{aligned} \nabla_{\boldsymbol{x}_i^n} \boldsymbol{K}^{e_i^n}(\boldsymbol{x}_i^n) &= \int_{s_{i-1}}^{s_i} EI^n \frac{\mathrm{d}\boldsymbol{N}_i}{\mathrm{d}s}\frac{\mathrm{d}\boldsymbol{N}_i^T}{\mathrm{d}s}\nabla_{\boldsymbol{x}_i^n}\boldsymbol{x}_i^n \mathrm{d}s \\ \nabla_{\boldsymbol{x}_i^n} \boldsymbol{M}^{e_i^n}(\boldsymbol{x}_i^n) &= \int_{s_{i-1}}^{s_i} \left({n_x}^n \cos\left(\theta_0 + \boldsymbol{N}_i^T\boldsymbol{x}_i^n\right) + {n_y}^n \sin\left(\theta_0 + \boldsymbol{N}_i^T\boldsymbol{x}_i^n\right)\right)\boldsymbol{N}_i\boldsymbol{N}_i^T\nabla_{\boldsymbol{x}_i^n}\boldsymbol{x}_i^n \mathrm{d}s \\ \nabla_{\boldsymbol{x}_i^n} \boldsymbol{G}^{e_i^n}(\boldsymbol{y}_i^n) &= \int_{s_{i-1}}^{s_i} EI^n \frac{\mathrm{d}\boldsymbol{N}_i}{\mathrm{d}s}\boldsymbol{N}_i^T\nabla_{\boldsymbol{x}_i^n}\boldsymbol{y}_i^n \mathrm{d}s \end{aligned} \tag{3.28}$$

where $\nabla_{\boldsymbol{x}_i^n}\boldsymbol{x}_i^n = \boldsymbol{I}_4$ for $1 \leq i \leq n-1$ and the components of $\nabla_{\boldsymbol{x}_i^n}\boldsymbol{y}_i^n$ will depend on the time integration scheme of the initial value problems (3.21). For the last element e_n^n, the initial and boundary conditions lead to the following matrices:

$$\nabla_{\boldsymbol{x}_n^n}\boldsymbol{x}_n^n = \begin{bmatrix} 1 & 0 & 0 & 0 \\ 0 & 1 & 0 & 0 \\ 0 & 0 & 1 & 0 \\ 0 & 0 & \partial_{\beta_n^n}\kappa_n^n & 0 \end{bmatrix}, \nabla_{\boldsymbol{x}_n^n}\boldsymbol{y}_n^n = \begin{bmatrix} * & * & 0 & 0 \\ * & * & 0 & 0 \\ 0 & 0 & \partial_{\beta_n^n}{\kappa^*}_n^n & 0 \\ 0 & 0 & \partial_{\beta_n^n}\omega_n^n & 0 \end{bmatrix} \tag{3.29}$$

3.3.2 Time integration schemes

To achieve the resolution of the finite dimensional system deduced from (3.22), it remains to compute the additional term G due to the remodelling effects at each time step. This can be performed by constructing a numerical scheme for the initial value problem (3.21). Subsequently, we first introduce implicit schemes, which are characterized by solving the non-linear system (3.23) before incrementing the time integration scheme at each time step. Then, explicit schemes are proposed in which the time integration is first computed before solving the non-linear spatial system.

Implicit Euler method

The implicit Euler method is applied to solve (3.21) which gives, for $1 \leq n \leq N$ and $0 \leq i \leq n$:

$$\begin{aligned}
{\kappa^*}_i^n &= \frac{{\kappa^*}_i^{n-1} + \Delta t \left(\frac{\partial_t EI_i^n}{EI_i^n} \kappa_i^n + p_i^n \right)}{1 + \Delta t \frac{\partial_t EI_i^n}{EI_i^n}} \\
\omega_i^n &= \omega_i^{n-1} + \Delta t \left[\left(\frac{\partial_{st} EI_i^n}{EI_i^n} - 2 \frac{\partial_s EI_i^n \partial_t EI_i^n}{(EI_i^n)^2} \right) (\kappa_i^n - {\kappa^*}_i^n) \right. \\
&\quad \left. + \frac{\partial_t EI_i^n}{(EI_i^n)^2} \Big({n_x}_i^n \sin(\theta_0 + \beta_i^n) - {n_y}_i^n \cos(\theta_0 + \beta_i^n) \Big) + \partial_s p_i^n \right]
\end{aligned} \tag{3.30}$$

with the initial conditions given by (3.26). Then, for an element e_i^n with $1 \leq i \leq n$, we can deduce the value of $\nabla_{\boldsymbol{x}_i^n} \boldsymbol{G}^{e_i^n}(\boldsymbol{y}_i^n)$ from:

$$\nabla_{\boldsymbol{x}_i^n} \boldsymbol{y}_i^n = \begin{bmatrix}
\partial_{\beta_{i-1}^n} {\kappa^*}_{i-1}^n & \partial_{\kappa_{i-1}^n} {\kappa^*}_{i-1}^n & 0 & 0 \\
\partial_{\beta_{i-1}^n} \omega_{i-1}^n & \partial_{\kappa_{i-1}^n} \omega_{i-1}^n & 0 & 0 \\
0 & 0 & \partial_{\beta_i^n} {\kappa^*}_i^n & \partial_{\kappa_i^n} {\kappa^*}_i^n \\
0 & 0 & \partial_{\beta_i^n} \omega_i^n & \partial_{\kappa_i^n} \omega_i^n
\end{bmatrix} \tag{3.31}$$

Finally, the coupled problem (3.20) and (3.21) is fully discretized at each time step n. First, the non-linear system $\boldsymbol{F}^n(\boldsymbol{x}^n) = \boldsymbol{0}$ is solved by a Newton method with the additional term G deduced from (3.30). Then, for $0 \leq i \leq n$, the obtained values of β_i^n and κ_i^n are used to compute the value of ${\kappa^*}_i^n$ and ω_i^n.

Crank-Nicolson method

The numerical time integration of (3.21) by the Crank-Nicolson method is performed as follows, for $1 \leq n \leq N$ and $0 \leq i \leq n$:

$$\begin{aligned}
{\kappa^*}_i^n &= \frac{{\kappa^*}_i^{n-1} + \frac{\Delta t}{2} \left(\frac{\partial_t EI_i^n}{EI_i^n} \kappa_i^n + \frac{\partial_t EI_i^{n-1}}{EI_i^{n-1}} \kappa_i^{n-1} + p_i^n + p_i^{n-1} \right)}{1 + \frac{\Delta t}{2} \frac{\partial_t EI_i^n}{EI_i^n}} \\
\omega_i^n &= \omega_i^{n-1} + \frac{\Delta t}{2} \left[\left(\frac{\partial_{st} EI_i^n}{EI_i^n} - 2 \frac{\partial_s EI_i^n \partial_t EI_i^n}{(EI_i^n)^2} \right) (\kappa_i^n - {\kappa^*}_i^n) \right. \\
&\quad + \left(\frac{\partial_{st} EI_i^{n-1}}{EI_i^{n-1}} - 2 \frac{\partial_s EI_i^{n-1} \partial_t EI_i^{n-1}}{(EI_i^{n-1})^2} \right) (\kappa_i^{n-1} - {\kappa^*}_i^{n-1}) \\
&\quad + \frac{\partial_t EI_i^n}{(EI_i^n)^2} \Big({n_x}_i^n \sin(\theta_0 + \beta_i^n) - {n_y}_i^n \cos(\theta_0 + \beta_i^n) \Big) \\
&\quad + \frac{\partial_t EI_i^{n-1}}{(EI_i^{n-1})^2} \Big({n_x}_i^{n-1} \sin(\theta_0 + \beta_i^{n-1}) - {n_y}_i^{n-1} \cos(\theta_0 + \beta_i^{n-1}) \Big) \\
&\quad \left. + \partial_s p_i^n + \partial_s p_i^{n-1} \right]
\end{aligned} \tag{3.32}$$

The Jacobian of the additional term G is computed in the same way as (3.31) in which Δt is substituted by $\Delta t/2$. Hence, the discretized problem is solved numerically similarly as in the implicit Euler case.

Explicit Euler method

The discretization of (3.21) reveals that the explicit Euler method would preserve the monotonicity if the following condition on the time step is satisfied:

$$\Delta t < \frac{1}{4}\frac{\min r_0}{\max v_r} \tag{3.33}$$

Consequently, by considering the changes of variable $\mu = EI\kappa^*$ and $\nu = \partial_s \mu$, we obtain the new following initial value problem:

$$\begin{cases} \partial_t \mu = \partial_t EI\kappa + EIp \\ \partial_t \nu = \left(\partial_{st} EI - \dfrac{\partial_s EI \partial_t EI}{EI}\right)\kappa + \dfrac{\partial_t EI}{EI}\Big(\nu + n_x \sin(\theta_0+\beta) - n_y \cos(\theta_0+\beta) + \partial_s(EIp)\Big) \\ \mu(s,\gamma(s)) = EI(s,\gamma(s))\kappa^\circ(s) \\ \nu(s,\gamma(s)) = \partial_s EI(s,\gamma(s))\kappa^\circ(s) + EI(s,\gamma(s))\dfrac{\mathrm{d}\kappa^\circ}{\mathrm{d}s}(s) - \dfrac{EI(s,\gamma(s))p(s,\gamma(s))}{v_a(\gamma(s))} \end{cases} \tag{3.34}$$

which does not impose the previous condition over the time step. Thus, the explicit Euler method gives:

$$\begin{aligned} \mu_i^n &= \mu_i^{n-1} + \Delta t\left(\partial_t EI_i^{n-1}\kappa_i^{n-1} + EI_i^{n-1}p_i^{n-1}\right) \\ \nu_i^n &= \nu_i^{n-1} + \Delta t\Bigg[\left(\partial_{st} EI_i^{n-1} - \frac{\partial_s EI_i^{n-1}\partial_t EI_i^{n-1}}{EI_i^{n-1}}\right)\kappa_i^{n-1} \\ &\quad + \frac{\partial_t EI_i^{n-1}}{EI_i^{n-1}}\Big(\nu_i^{n-1} + {n_x}_i^{n-1}\sin(\theta_0+\beta_i^{n-1}) - {n_y}_i^{n-1}\cos(\theta_0+\beta_i^{n-1})\Big)\Bigg] \end{aligned} \tag{3.35}$$

with the initial conditions:

$$\begin{aligned} \mu_n^n &= EI_n^n \kappa_{\max}\sin\left(\frac{\theta_P - \theta_0 - \beta_n^n}{2}\right) \\ \nu_n^n &= \partial_s EI_n^n \kappa_{\max}\sin\left(\frac{\theta_P - \theta_0 - \beta_n^n}{2}\right) \\ &\quad + EI_n^n \kappa_{\max}^2\left(\frac{1}{2}\sin(\theta_P - \theta_0 - \beta_n^n) - \sin\left(\frac{\theta_P - \theta_0 - \beta_n^n}{2}\right)\right) - EI_n^n \frac{2\alpha}{r_0^2}\frac{{v_r}_n^n}{{v_a}_n^n}\sin(\theta_P - \theta_0 - \beta_n^n) \end{aligned} \tag{3.36}$$

Moreover, in the case of explicit scheme, the Jacobian of the additional term G is simplified since for $1 \leq i \leq n-1$, we have $\nabla_{\boldsymbol{x}_i^n}\boldsymbol{y}_i^n = \mathbf{0}$ and for the last element e_n^n:

$$\nabla_{\boldsymbol{x}_n^n}\boldsymbol{y}_n^n = \begin{bmatrix} 0 & 0 & 0 & 0 \\ 0 & 0 & 0 & 0 \\ 0 & 0 & \partial_{\beta_n^n}\mu_n^n & 0 \\ 0 & 0 & \partial_{\beta_n^n}\nu_n^n & 0 \end{bmatrix}$$

Finally, the numerical solution is computed at each time step n, by first incrementing (3.35) and then solving the non-linear system $\boldsymbol{F}^n(\boldsymbol{x}^n) = \mathbf{0}$.

Heun's method

We close this presentation of time integration schemes with the Heun's predictor-corrector method. At each time step n, the explicit Euler method is applied and the non-linear system is

solved (predictor), giving the intermediate solutions $\tilde{\mu}_i^n$, $\tilde{\nu}_i^n$, $\tilde{\beta}_i^n$ and $\tilde{\kappa}_i^n$. Then, this intermediate values are considered to increment the following scheme (corrector):

$$\begin{aligned}
\mu_i^n &= \mu_i^{n-1} + \frac{\Delta t}{2}\left(\partial_t EI_i^{n-1}\kappa_i^{n-1} + \partial_t EI_i^n\tilde{\kappa}_i^n + EI_i^{n-1}p_i^{n-1} + EI_i^n\tilde{p}_i^n\right)\\
\nu_i^n &= \nu_i^{n-1} + \frac{\Delta t}{2}\left[\left(\partial_{st}EI_i^{n-1} - \frac{\partial_s EI_i^{n-1}\partial_t EI_i^{n-1}}{EI_i^{n-1}}\right)\kappa_i^{n-1} + \left(\partial_{st}EI_i^n - \frac{\partial_s EI_i^n\partial_t EI_i^n}{EI_i^n}\right)\tilde{\kappa}_i^n\right.\\
&\quad + \frac{\partial_t EI_i^{n-1}}{EI_i^{n-1}}\left(\nu_i^{n-1} + {n_x}_i^{n-1}\sin(\theta_0+\beta_i^{n-1}) - {n_y}_i^{n-1}\cos(\theta_0+\beta_i^{n-1})\right)\\
&\quad \left.+\frac{\partial_t EI_i^n}{EI_i^n}\left(\tilde{\nu}_i^n + {n_x}_i^n\sin(\theta_0+\tilde{\beta}_i^n) - {n_y}_i^n\cos(\theta_0+\tilde{\beta}_i^n)\right)\right]
\end{aligned} \tag{3.37}$$

Finally, the non-linear spatial system is solved again with these new incremented values.

3.4 Numerical simulations

In this section, numerical results are analysed to illustrate the properties of the previous schemes. We consider that the growing stem is submitted to its self-weight and that the function v_a and v_r are constant. Thus, we obtain the following exact solutions for the problems (3.2), (3.3) and (3.4) for, $(s,t) \in Q$:

$$\begin{cases}
L(t) = v_a t\\
r(s,t) = v_r t - \dfrac{v_r}{v_a}s + r_0\\
n_x(s,t) = 0\\
n_y(s,t) = -\dfrac{1}{3}\rho g\pi(v_a t - s)\left(r^2 + r_0 r + r_0^2\right)
\end{cases} \tag{3.38}$$

In order to test the convergence and the stability of the schemes, the simulations are performed with various time steps Δt and different values of the parameters r_0 and v_r. Moreover, we consider the very specific case of small deflection ($\theta \approx \theta_0$) with $\theta_0 = 0$, $\theta_P = \pi/2$ and $\kappa_{\max} = 0$, and thus, the linearisation of the system defined in section 3.2.2 leads to the following exact solution:

$$\kappa(s,t) = -\frac{4}{3}\frac{\rho g}{E}\left[\left(\frac{v_a}{v_r}\right)^2\left(1 - \frac{r}{r_0} + \log\left(\frac{r}{r_0}\right)\right) + \frac{(v_a t - s)^2}{r_0^2}\left(\frac{r_0}{r} + \frac{2}{3}\frac{r_0^2}{r^2} + \frac{1}{3}\frac{r_0^3}{r^3}\right)\right] + 2\alpha\left(\frac{1}{r_0} - \frac{1}{r}\right) \tag{3.39}$$

$$\begin{aligned}
\theta(s,t) = -\frac{4}{3}\frac{\rho g}{E}\left(\frac{v_a}{v_r}\right)^3&\left[-r\log\left(\frac{r}{r_0}\right) + \frac{r_0^3}{6}\left(\frac{1}{r^2} - \frac{1}{(v_r t + r_0)^2}\right) - \frac{4}{3}\frac{v_r}{v_a}s + (v_r t + r_0)\log\left(\frac{v_r t + r_0}{r_0}\right)\right]\\
&+ 2\alpha\left(\frac{s}{r_0} + \frac{v_a}{v_r}\log\left(\frac{r}{v_r t + r_0}\right)\right)
\end{aligned} \tag{3.40}$$

Then, to compare the numerical results with the previous exact solution, we consider the Banach space $\mathcal{X}$ such that $u \in \mathcal{X}$ if, for $t \in [0,T]$ and $s \in [0, L(T)]$, we have $u(\cdot,t) \in \mathcal{V}^t$ and $u(s,\cdot) \in L^2([\gamma(s),T])$ with:

$$\|u\|_{\mathcal{X}} = \left(\int_0^T \|u\|_{\mathcal{V}^t}^2 \mathrm{d}t\right)^{\frac{1}{2}}$$

where $\|\cdot\|_{\mathcal{V}^t} = \|\cdot\|_{H^2([0,L(t)])}$. Thus, the error e_h between the exact solution θ and the numerical approximation θ_h is given by $e_h = \|\theta - \theta_h\|_{\mathcal{X}}$ and is assessed by the Gauss-Legendre quadrature for the space integration and the trapezoidal rule for the time integration.

Parameter	Unit	Fig 3.3,3.4	Fig 3.5,3.6	Fig 3.8
r_0	m	0.001	0.001	0.001
v_r	m/y	0.001	0.01	0.001
v_a	m/y	1.0	1.0	1.0
θ_0	rad	0	0	$\pi/4$
θ_P	rad	$\pi/2$	$\pi/2$	$\pi/2$
α	def (m/m)	2.10^{-4}	2.10^{-4}	1.10^{-4}
$\kappa_{\max}$	m^{-1}	0	0	5
ρ	kg/m^3	1000	1000	1000
g	N/kg	10	10	10
E	Pa	10^{10}	10^{10}	10^9

Tab. 3.1: Parameter values used for the numerical simulations. These parameters are taken from [3, 10, 11].

Figures 3.3 and 3.4 shows the results obtained for θ_h and κ_h at time $t = 1$ year for different time steps Δt. The parameters values are summed up in table 3.1. As the time step size decreases, the numerical solutions get closer to the exact solution. As expected, the Crank-Nicolson method and Heun's method have a better accuracy than the implicit and explicit Euler method, for an equal time step size. This is confirmed by the error analysis with respect to the time step size in figure 3.7(b).

Regarding the condition (3.33), it is relevant to consider specific values of r_0 and v_r such that the ratio r_0/v_r remains small. This is achieved in figures 3.5 and 3.6 that show the numerical solutions obtained for θ_h and κ_h. Compared with the previous simulation, the results indicate a slower convergence toward the exact solution θ, particularly for the explicit Euler method. Furthermore, the numerical approximations of the curvature κ obtained with the implicit Euler method and the Crank-Nicolson method lead to spurious solutions for large time steps. More precisely, accentuating oscillations appears from the free end of the rod ($s = 1$), where the value of κ is imposed, to the cantilevered end ($s = 0$). However, figure 3.7(a) indicates that the rate of convergence is still greater for the implicit methods than for the explicit methods.

Other errors resulting from simulations for different values of r_0 and v_r are shown in figure 3.7. These results highlight that the quality of the numerical approximation strongly depends on the values of r_0 and v_r. For a given time step, the error is more significant in the case of small ratio r_0/v_r. In the worst case, even with a small time step, the error e_h of the explicit Euler method may reach important order of magnitude. In this context, the Crank-Nicolson method and the Heun's method have interesting characteristics in term of accuracy and rate of convergence, and may be preferred if attention is paid to the time step size according to the value of the ratio r_0/v_r.

Figures 3.7(a) and 3.7(b) show that the use of second order numerical methods are almost of same accuracy than first order methods. In contrary, in figures 3.7(c) and 3.7(d) the difference is clear between first order and second order methods. However, choosing the time step lower than 10^{-2} does not necessary increase the approximations significantly. In fact, this limitation may be related to the accumulation of errors due to the use of Hermite finite element approximation, of time integration method, and Newton's algorithm to solve the nonlinear equation. Thus high order time integration methods are only useful for a large time-step and when $r_0/v_r > 1$. This question will require further investigations.

The table 3.2 presents the CPU times obtained for each numerical method. The results are similar for the implicit and explicit Euler methods and for the Crank-Nicolson method, whereas the Heun's method may take 50% longer. This is caused by the two-steps resolution (predictor-corrector) of the non-linear finite element system at each time step. Besides, the required time to perform the simulation increases exponentially for a decreasing time step, since the size of

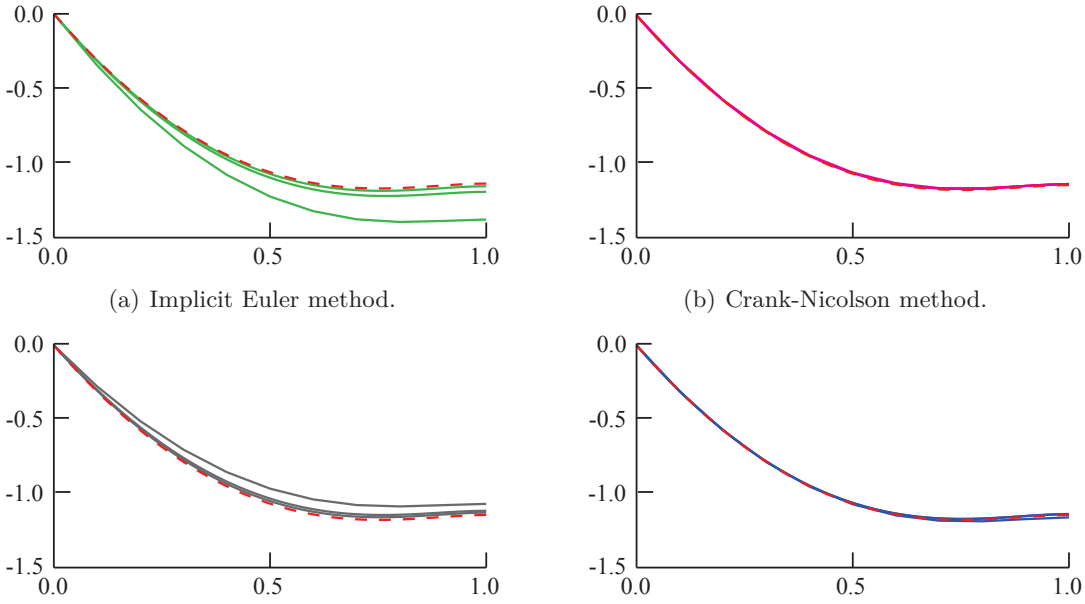

(a) Implicit Euler method. (b) Crank-Nicolson method.

(c) Explicit Euler method. (d) Heun's method.

Fig. 3.3: Numerical results of the angle θ at $t = 1$ with $r_0 = 0.001$, $v_r = 0.001$ and $\Delta t = 0.1$, 0.025, 0.01. The solid lines represents the successive simulations, whereas the dashed line gives the values for the exact solution. X-axis corresponds to the arc-length (m).

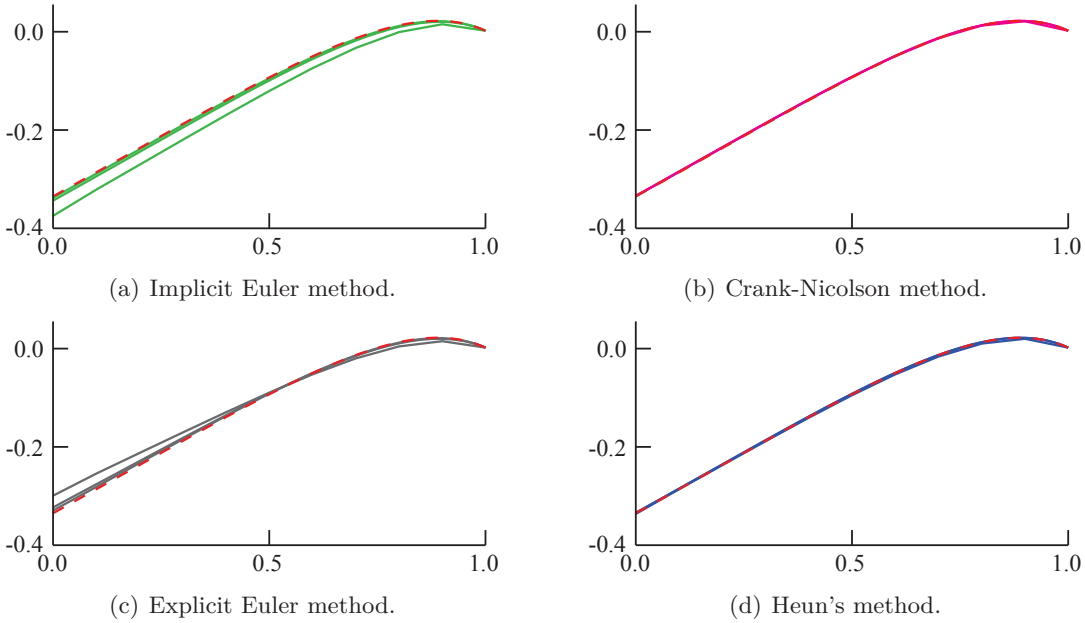

(a) Implicit Euler method. (b) Crank-Nicolson method.

(c) Explicit Euler method. (d) Heun's method.

Fig. 3.4: Numerical results of the curvature κ at $t = 1$ with $r_0 = 0.001$, $v_r = 0.001$ and $\Delta t = 0.1$, 0.025, 0.01. The solid lines represents the successive simulations, whereas the dashed line gives the values for the exact solution. X-axis corresponds to the arc-length (m); Y-axis corresponds to the rod curvature (m^{-1}).

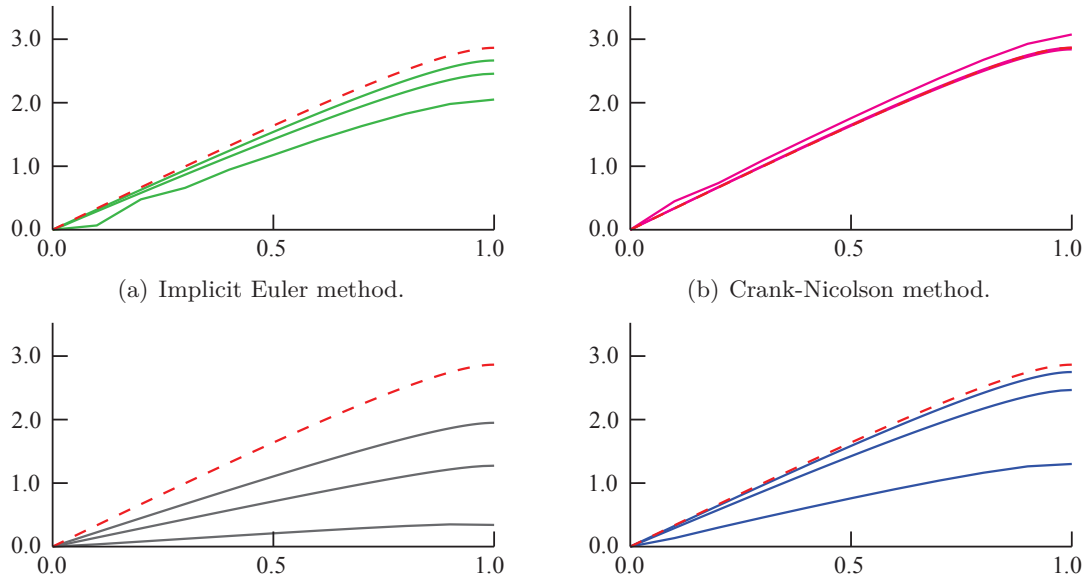

(a) Implicit Euler method. (b) Crank-Nicolson method.

(c) Explicit Euler method. (d) Heun's method.

Fig. 3.5: Numerical results of the angle θ at $t = 1$ with $r_0 = 0.001$, $v_r = 0.01$ and $\Delta t = 0.1$, 0.025, 0.01. The solid lines represents the successive simulations, whereas the dashed line gives the values for the exact solution. X-axis corresponds to the arc-length (m).

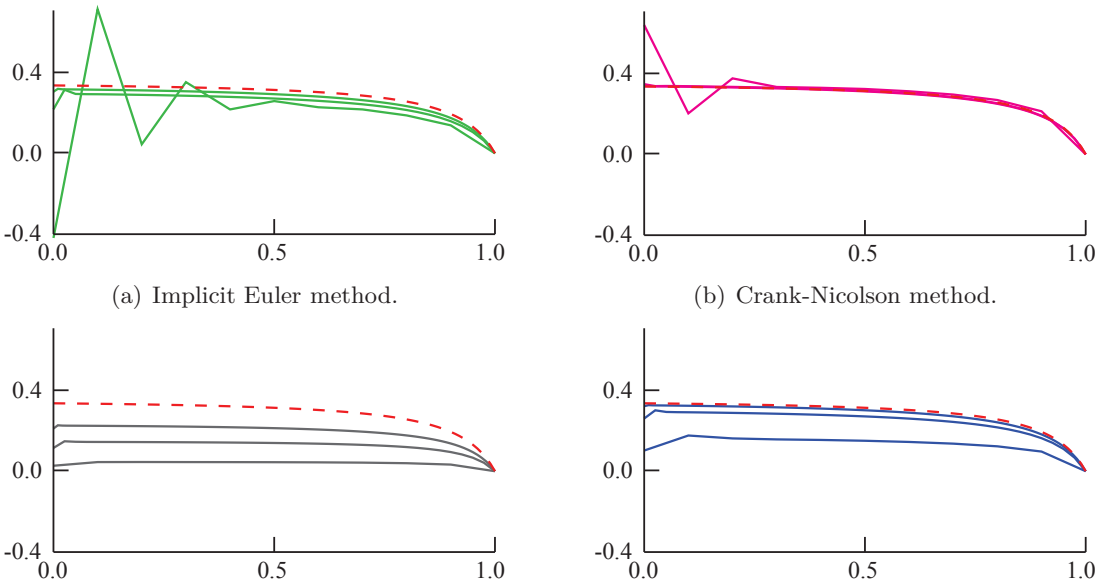

(a) Implicit Euler method. (b) Crank-Nicolson method.

(c) Explicit Euler method. (d) Heun's method.

Fig. 3.6: Numerical results of the curvature κ at $t = 1$ with $r_0 = 0.001$, $v_r = 0.01$ and $\Delta t = 0.1$, 0.025, 0.01. The solid lines represents the successive simulations, whereas the dashed line gives the values for the exact solution. X-axis corresponds to the arc-length (m); Y-axis corresponds to the rod curvature (m^{-1}).

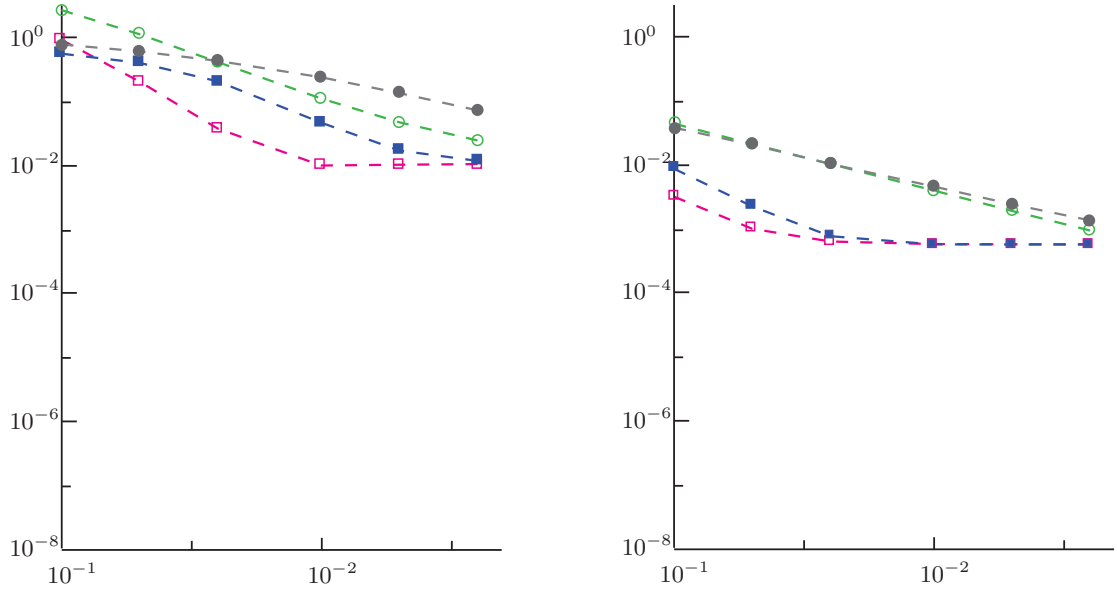

(a) $r_0 = 0.001$ and $v_r = 0.01$ $(r_0/v_r < 1)$

(b) $r_0 = 0.001$ and $v_r = 0.001$ $(r_0/v_r = 1)$

(c) $r_0 = 0.01$ and $v_r = 0.01$ $(r_0/v_r = 1)$

(d) $r_0 = 0.01$ and $v_r = 0.001$ $(r_0/v_r > 1)$

Fig. 3.7: Error $e_h = \|\theta - \theta_h\|_{\mathcal{X}}$ with respect to the time step Δt and for different values of r_0 and v_r (the values of the other parameters are the same as those used in figures 3.3 and 3.4). Here $\circ$ represents the implicit Euler method, $\square$ the Crank-Nicolson method, $\bullet$ the explicit Euler method and $\blacksquare$ the Heun's method.

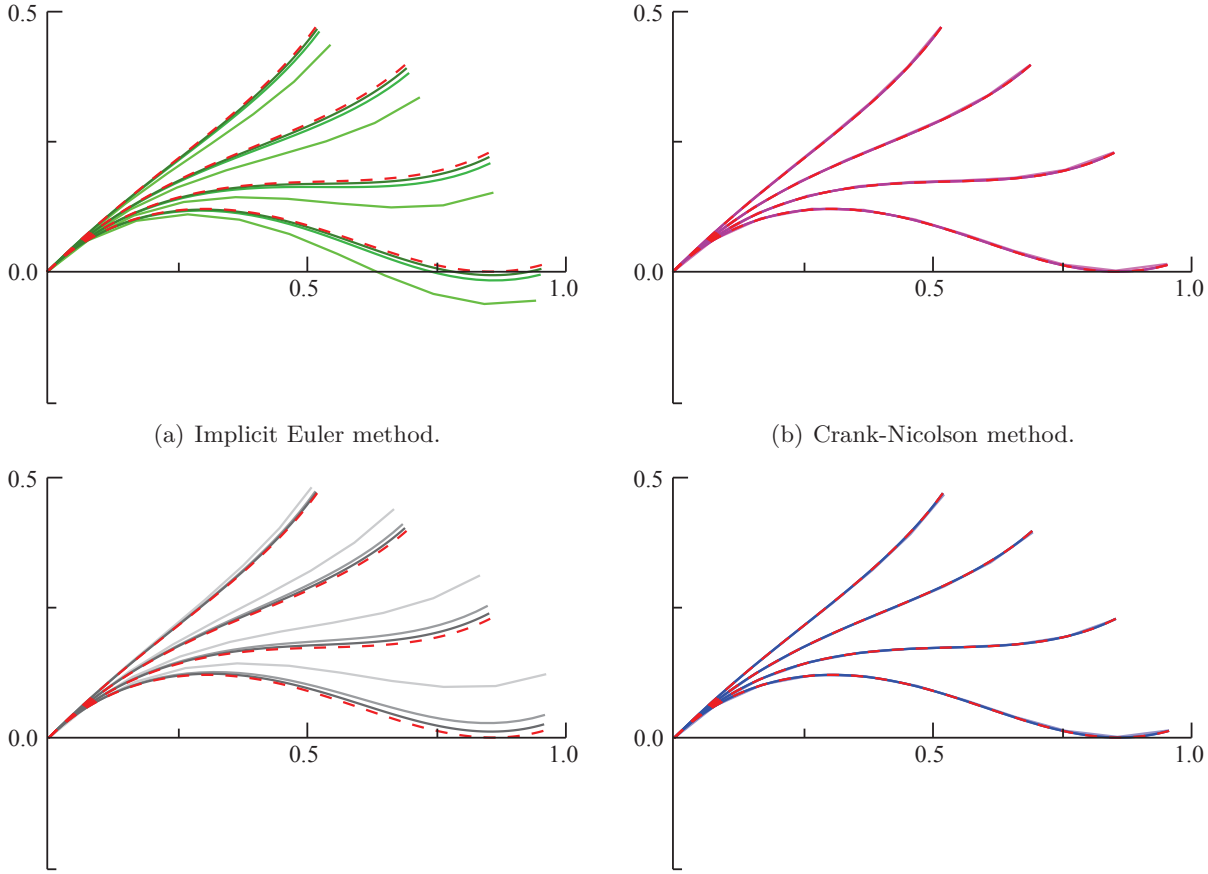

(a) Implicit Euler method.

(b) Crank-Nicolson method.

(c) Explicit Euler method.

(d) Heun's method.

Fig. 3.8: Numerical simulations of the current configuration $\boldsymbol{r}$ at $t = 0.7, 0.8, 0.9, 1$ with $\Delta t = 0.1$, 0.025, 0.01. The solid lines represents the successive simulations, whereas the dashed line gives the values for the Crank-Nicolson method with $\Delta t = 0.0025$. X-axis and Y-axis correspond to the horizontal and vertical distance (m).

Δt	Implicit Euler	Crank-Nicolson	Explicit Euler	Heun
0.01	2.42	2.55	1.72	3.23
0.0025	128.43	130.08	117.73	196.68

Tab. 3.2: CPU times (s) estimates for the computation of the results in figures 3.3 and 3.4. The simulations are performed with Java 6 on Intel Core Duo CPU T7250 (2 GHz).

the non-linear finite element system is increasing at each time step. This characteristic, due to the dependence between time and space discretization, may be of great importance to choose the numerical method for given values of r_0 and v_r.

Finally, figure 3.8 shows a more complex and realistic simulation of a growing stem considering the three main processes involved in the control of tree shape, i.e. gravity, secondary straightening up and primary tropism ($\kappa_{\max} \neq 0$). The current configuration is presented at different times and, since there is no accurate exact solution in this case because of the large values of θ, the results are compared with those obtained with the Crank-Nicolson method with $\Delta t = 0.0025$. It can be seen in figures 3.8(a) and 3.8(c) that the rod's deflection is overestimated with the implicit Euler method whereas it is underestimated with explicit Euler method. As previously seen in figure 3.7, the Crank-Nicolson method and the Heun's method presents a more significant rate of convergence than the Euler methods.

3.5 Conclusion

In this paper, the discretization of the partial differential equations modelling the biomechanics of a growing rod has been investigated. The system has been rewritten considering the coupling between a non-linear boundary value problem and a linear initial value problem. The finite element method has been implemented for the boundary value problem and different time integration schemes have been proposed to discretize the initial value problem. In comparison with previous works, which have only considered an explicit incremental approach, the numerical experiments have revealed that the explicit Euler method has a poor accuracy and should be avoided, particularly in the case of ratio $r_0/v_r < 1$. However, even with the Crank-Nicolson method, attention must be paid to the time step size, since, for large time steps, implicit schemes lead to spurious solutions that may come from numerical instabilities. The Heun's method is an interesting alternative if an explicit scheme is needed to take into account a nonlinear constitutive relation, but the computation time may increase drastically for small time step. Further studies should therefore investigate the theoretical properties of convergence and stability of the presented schemes in order to optimize the time step size and to consider adaptive integration methods.

Acknowledgements

Thanks are due to Agropolis Fondation which supported this research work. AMAP (Botany and Computational Plant Architecture, http://amap.cirad.fr/) is a joint research unit which associates CIRAD (UMR51), CNRS (UMR5120), INRA (UMR931), IRD (2M123), and Montpellier 2 University (UM27).

3.6 Appendix

3.6.1 Hermite finite elements

The shape functions of the Hermite element and their derivatives, which support is $[0,1]$ are given by:

$$\begin{cases} \hat{\varphi}_0(\xi) = (1-\xi)^2(2\xi+1) \\ \hat{\psi}_0(\xi) = \xi(1-\xi)^2 \\ \hat{\varphi}_1(\xi) = \xi^2(3-2\xi) \\ \hat{\psi}_1(\xi) = \xi^2(\xi-1) \end{cases} \quad \text{and} \quad \begin{cases} \dfrac{\mathrm{d}\hat{\varphi}_0}{\mathrm{d}\xi}(\xi) = -6\xi(1-\xi) \\ \dfrac{\mathrm{d}\hat{\psi}_0}{\mathrm{d}\xi}(\xi) = (1-\xi)(1-3\xi) \\ \dfrac{\mathrm{d}\hat{\varphi}_1}{\mathrm{d}\xi}(\xi) = 6\xi(1-\xi) \\ \dfrac{\mathrm{d}\hat{\psi}_1}{\mathrm{d}\xi}(\xi) = \xi(3\xi-2) \end{cases} \tag{3.41}$$

where $\xi \in [0,1]$. Using the change of variable $s = s_{i-1} + h_i\xi$, we can deduce the shape functions and their derivatives for $s \in [s_{i-1}, s_i]$:

$$\begin{cases} \varphi_{i-1}(s) = \hat{\varphi}_0\left(\dfrac{s-s_{i-1}}{h_i}\right) \\ \psi_{i-1}(s) = h_i\hat{\psi}_0\left(\dfrac{s-s_{i-1}}{h_i}\right) \\ \varphi_i(s) = \hat{\varphi}_1\left(\dfrac{s-s_{i-1}}{h_i}\right) \\ \psi_i(s) = h_i\hat{\psi}_1\left(\dfrac{s-s_{i-1}}{h_i}\right) \end{cases} \quad \text{and} \quad \begin{cases} \dfrac{\mathrm{d}\varphi_{i-1}}{\mathrm{d}s}(s) = \dfrac{1}{h_i}\dfrac{\mathrm{d}\hat{\varphi}_0}{\mathrm{d}s}\left(\dfrac{s-s_{i-1}}{h_i}\right) \\ \dfrac{\mathrm{d}\psi_{i-1}}{\mathrm{d}s}(s) = \dfrac{\mathrm{d}\hat{\psi}_0}{\mathrm{d}s}\left(\dfrac{s-s_{i-1}}{h_i}\right) \\ \dfrac{\mathrm{d}\varphi_i}{\mathrm{d}s}(s) = \dfrac{1}{h_i}\dfrac{\mathrm{d}\hat{\varphi}_1}{\mathrm{d}s}\left(\dfrac{s-s_{i-1}}{h_i}\right) \\ \dfrac{\mathrm{d}\psi_i}{\mathrm{d}s}(s) = \dfrac{\mathrm{d}\hat{\psi}_1}{\mathrm{d}s}\left(\dfrac{s-s_{i-1}}{h_i}\right) \end{cases} \tag{3.42}$$

3.6.2 Gauss-Legendre quadrature

The approximation of an integral with the five-points Gauss-Legendre quadrature is defined by:

$$\int_{s_{i-1}}^{s_i} f(s)\mathrm{d}s = \sum_{k=1}^{5} w_k f(z_k) = w_1 f(z_1) + w_2 f(z_2) + w_3 f(z_3) + w_4 f(z_4) + w_5 f(z_5)$$

where:

$$\begin{aligned} w_1 &= \frac{h_i}{2}\left(\frac{322+13\sqrt{70}}{900}\right) & z_1 &= \frac{s_{i-1}+s_i}{2} - \frac{h_i}{6}\sqrt{5-2\sqrt{\frac{10}{7}}} \\ w_2 &= \frac{h_i}{2}\left(\frac{322-13\sqrt{70}}{900}\right) & z_2 &= \frac{s_{i-1}+s_i}{2} - \frac{h_i}{6}\sqrt{5+2\sqrt{\frac{10}{7}}} \\ w_3 &= \frac{h_i}{2}\left(\frac{128}{225}\right) & z_3 &= \frac{s_{i-1}+s_i}{2} \\ w_4 &= \frac{h_i}{2}\left(\frac{322-13\sqrt{70}}{900}\right) & z_4 &= \frac{s_{i-1}+s_i}{2} + \frac{h_i}{6}\sqrt{5+2\sqrt{\frac{10}{7}}} \\ w_5 &= \frac{h_i}{2}\left(\frac{322+13\sqrt{70}}{900}\right) & z_5 &= \frac{s_{i-1}+s_i}{2} + \frac{h_i}{6}\sqrt{5-2\sqrt{\frac{10}{7}}} \end{aligned} \tag{3.43}$$

References

[1] M. Fournier, A. Stokes, C. Coutand, T. Fourcaud, B. Moulia, Ecology and biomechanics : a mechanical approach to the ecology of animals and plants, CRC Taylor and Francis, 2006, Ch. 1 : Tree Biomechanics and Growth Strategies in the Context of Forest Functional Ecology, pp. 1–33.

[2] D. Ambrosi, F. Mollica, On the mechanics of a growing tumor, International Journal of Engineering Science 40 (2002) 1297–1316.

[3] H. Yamamoto, M. Yoshida, T. Okuyama, Growth stress controls negative gravitropism in woody plant stem, Planta 216 (2002) 280–292.

[4] T. Fourcaud, P. Lac, Numerical modelling of shape regulation and growth stresses in trees. part i: An incremental static finite element formulation, Trees 17 (2003) 23–30.

[5] J.-D. M. Catherine Coutand and, G. Jeronimidis, J.-F. Destrebecq, Twig: A model to simulate the gravitropic response of a tree axis in the frame of elasticity and viscoelasticity, at intra-annual time scale, Journal of Theoretical Biology 273 (2011) 115–129.

[6] O. M. O'Reilly, T. N. Tresierras, On the evolution of intrinsic curvature in rod-based models of growth in long slender plant stem, International Journal of Solids and Structure 48 (2011) 1239–1247.

[7] T. Guillon, Y. Dumont, T. Fourcaud, A mathematical framework for modelling the biomechanics of growing trees with rod theory, manuscript submitted for publication.

[8] M. Fournier, H. Bailleres, B. Chanson, Tree biomechanics: Growth, cumulative prestresses, and reorientations, Biomimetics 2 (1994) 229–251.

[9] S. S. Antman, Nonlinear Problems of Elasticity, Springer, 2005, Ch. 8 : Theory of Rods Deforming in Space, pp. 269–344.

[10] T. Fourcaud, F. Blaise, P. Lac, P. Castéra, P. de Reffye, Numerical modelling of shape regulation and growth stresses in trees. part ii: implementation in the amappara software and simulation of tree growth, Trees 17 (2003) 31–39.

[11] T. Alméras, M. Fournier, Biomechanical design and long-term stability of trees: Morphological and wood traits involved in the balance between weight increase and the gravitropic reaction, Journal of theoretical Biology 256 (2009) 370–381.

Chapitre 4

OPTIMAL CONTROL OF BIOMASS ALLOCATION IN PRIMARY AND SECONDARY GROWTH FOR THE GRAVITROPIC RESPONSE OF A GROWING STEM

Thomas Guillon* Yves Dumont† Tancrède Alméras‡ Thierry Fourcaud†

Abstract

Height is a major ecological trait for growing trees, representing the intensity for light competition. Moreover, tree height results from a tradeoff between different functions, including tree mechanical stability. Trees develop growth strategies to maintain their vertical orientation and mechanical stability, in addition to other ecophysiological functions, through differential primary growth near the shoot apical meristem and formation of reaction wood during secondary growth. Although an important variability in straightening strategies have been observed both in experimental studies and in the field, to our knowledge no theoretical studies have been carried out to explain these differences in dynamic biomass allocation with respect to the ecological context. The present work addresses the mathematical formulation of two optimal control problems characterising tree's growth strategies, both formulation being based on maximizing height that is important for light competition and for trees emerging from a closed canopy. Growth strategies are considered through two variables, which are the ratio of biomass allocated to primary growth and the distribution of biomass allocated to secondary growth along the growing stem. The gradients of the objective functionals are evaluated using the adjoint equations. A projected gradient algorithm is introduced to solve numerically the optimization problems. This method needs the computation of the projection operator of a cubic Hermite interpolation onto the closed convex space of differentiable distribution functions. Thus, an intermediate optimization problem has to be solved and relies on the characterization of non-negative polynomials over an interval. This work gives the theoretical foundations that are necessary to solve numerically the optimal control problems related to the biomechanics of growing trees.

Keywords : Height growth strategy, Tree biomechanics, Reaction wood, Adjoint equations, Projected gradient methods.

∗. Université Montpellier II, UMR AMAP, TA-A51/PS2, boulevard de la Lironde, 34398 Montpellier Cedex 5, France

†. CIRAD, UMR AMAP, TA-A51/PS2, boulevard de la Lironde, 34398 Montpellier Cedex 5, France

‡. CNRS, Laboratoire de Mécanique et Génie Civil, Université Montpellier II, CC48, Place Eugène Bataillon, 34095 Montpellier, France

4.1 Introduction

Height is a major ecological trait in tree's growth strategy, which is related to the competition for light [1] and wind dispersal of seeds [2]. However, growth in height has important mechanical consequences since it increases the risk of buckling or breakage due to self-weight or wind forces [3]. In order to maintain the vertical orientation of their main axes under mechanical disturbances, trees have developed two control mechanisms [4, 3, 5] 1 – a differential growth of shoot apical meristem, i.e. more cells are formed on one side of the axis, modifying the tip growth orientation; 2 – a differential elongation or shortening of wood fibre at the periphery of the axis during their maturation phase, which generates internal prestresses and induces a bending movement of the whole stem. At the macroscopic level, the first mechanism is related to an initial curvature at the tip of the growing stem due to primary growth, while the second involves a change in curvature due to the formation of reaction wood during secondary growth.

The combination of these two control mechanisms leads to different straightening strategies of tree stems. Furthermore, secondary growth may have two opposite effects: 1 – it increases the bending moment resulting from the integration of asymmetrical maturation strains within the actual growth ring; 2 – it increases the stem stiffness, limiting its straightening up efficiency. The efficiency of the gravitropic response of tropical seedling has been explored and highlights important differences between species depending on their light requirement [6]. Nevertheless, even species with the same light requirement can present distinct reorientation strategies with different spatio-temporal patterns in primary and secondary tropism [7, 8]. An experiment have been conducted in an ecological context to examine growth strategies of *Fagus sylvatica* and *Acer pseudoplatanus* in response to canopy disturbance [9]. The results have indicated that uprighting movements due to primary and secondary tropism have a significant role that provides a rapid response to canopy opening. Moreover the two species have revealed distinct strategies: a rapid height growth rate and a restricted stem diameter in *Acer*, allowing efficient reorientation at the setm base; a lower height growth rate with a higher stem diameter in *Fagus* to maintain a vertical orientation. Although modelling approaches have been carried out to recognize the implications of both primary and secondary tropism in the straightening up of stems [10, 11, 12], little information is available on which combination of the two control mechanisms allows to reach a theoretical optimal height in a given ecological context.

The purpose of this paper is to investigate, in a theoretical way, the optimal biomass allocations in primary and secondary growth that lead to a maximal height of a growing stem submitted to its self-weight. More precisely, we compare the differences between two growth strategies for a given amount of biomass 1 – maximizing height at each time, which is related to light competition in a dense population; 2 – maximizing height at a final target date, which is related to trees emerging from a closed canopy. Growth strategies are analysed with regard to initial inclination, material properties (mass density, Young's modulus) and developmental characteristics such as biomass production and evolution of mass distribution over the main axis. A recent continuous mathematical formulation of tree growth biomechanics is used for developing the optimal control problems [13, 14]. An outline of the paper is as follows: Section 4.2 defines the relation between biomass allocation and the system of partial differential equations modelling the biomechanics of a growing rod. Section 4.3 is concerned with the mathematical formulation of the two optimal control problems and their first-order necessary conditions. The numerical algorithm performing the discretized solution of the constrained maximization problems is investigated in Section 4.4. Concluding comments about the contribution of the theoretical approach developed in this study are given in Section 4.5.

4.2 The Mathematical model

This section is devoted to the mathematical description of the biomechanics of a growing tree with rod theory. The relation between biomass allocation and geometrical description of growth is analysed and integrated to the system of partial differential equations developed in [13].

4.2.1 Biomass allocation and geometrical description of growth

We consider the functional dependencies between the biomass allocated to growth and the resulting geometry of growing rod, which is characterized by the evolution at each time of its length (primary growth) and of the diameter of its cross-sections (secondary growth).

Primary growth

Given a time $t \in [0, T]$, we assume that the biomass devoted to the growth per unit time is denoted $q(t)$. At the final time T, the total biomass B devoted to primary and secondary growth is given by:

$$B(T) = \int_0^T q(t)\mathrm{d}t$$

Then, $\xi(t)$ represents the ratio of biomass allocated to primary growth at time t, i.e. growth in length, and the function ξ belongs to the following closed convex functional space:

$$\mathcal{K}_1 = \left\{\xi \in L^2([0,T])/\forall t \in [0,T], \xi(t) \in [0,1]\right\} \tag{4.1}$$

Assuming a constant mass density and a constant circular pith radius r_0 (radius of the primary meristem), the length of the rod is the solution of the following differential equation:

$$\begin{cases} \dfrac{\mathrm{d}L}{\mathrm{d}t}(t) = \dfrac{\xi(t)q(t)}{\rho\pi r_0^2} \\ L(0) = 0 \end{cases} \tag{4.2}$$

The length L is an increasing function in time, and we denote $v_a = \mathrm{d}L/dt \geq 0$ the apical growth velocity. If L is strictly increasing, then the inverse function $\gamma(s)$ gives the date of appearance of the cross-section located at arc-length s. Therefore, the basic set of all admissible material cross-section at each time is defined by (see figure 4.1(a)):

$$Q = \{(s,t)/t \in [0,T], s \in [0, L(t)]\} \tag{4.3}$$

It is important to notice that space and time are not independent in the modelling of the biomechanics of a growing rod. Therefore, the mechanical equilibrium of the rod has to be computed at each time on the increasing domain $[0, L(t)]$. Moreover, the basic set Q contains the boundary points $(0,t)$ and $(L(t),t)$ representing the two ends of the rod, whereas for a given arc-length s, the point $(s, \gamma(s))$ gives an initial condition at the date of appearance of the cross-section located at s.

Secondary growth

According to the foregoing, the ratio of biomass allocated to secondary growth at each time t is equal to $(1 - \xi(t))$. But it remains to distribute this biomass along the existing cross-sections, increasing their area. We thus introduce the distribution of the biomass allocated to secondary growth η. Considering the following functional space:

$$\mathcal{X} = \left\{u \in L^2(Q)/\forall t \in [0,T], u(\cdot,t) \in H^1([0, L(t)])\right\} \tag{4.4}$$

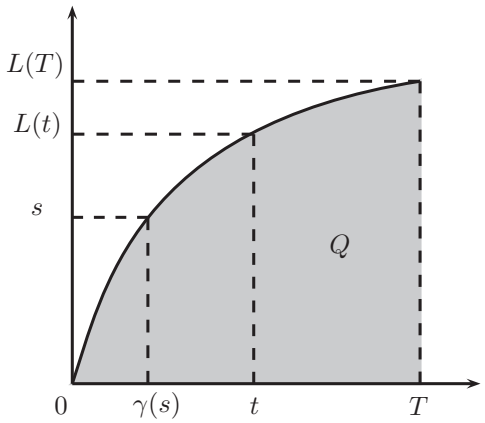

(a) The basic set Q and length L of the rod at each time. The inverse function $\gamma(s)$ gives the date of appearance of a material point located at arc-length s.

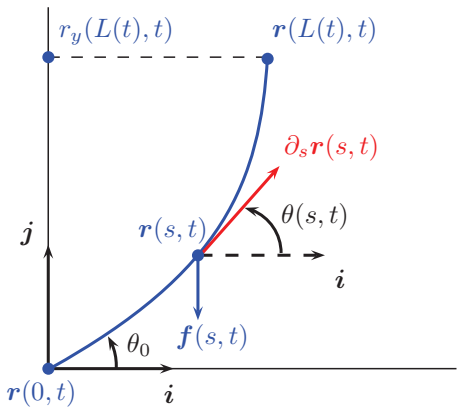

(b) Planar motion of an inextensible and unshearable growing rod subjected to its self-weight $\boldsymbol{f}$. The height of the stem at time t is given by $r_y(L(t),t)$. θ is the angle between $\boldsymbol{i}$ and $\partial_s\boldsymbol{r}$.

Fig. 4.1: The basic set of all admissible material points and the planar motion of a growing rod.

we assume that $\eta \in \mathcal{K}_2$, where:

$$\mathcal{K}_2 = \left\{ \eta \in \mathcal{X} / \forall (s,t) \in Q, \eta(s,t) \geq 0 \text{ and } \int_0^{L(t)} \eta(s,t)\mathrm{d}s = 1 \right\} \tag{4.5}$$

Hence, the evolution of the cross-sectional area A is the solution of the following initial value problem:

$$\begin{cases} \partial_t A(s,t) = \dfrac{\eta(s,t)(1-\xi(t))q(t)}{\rho} \\ A(s,\gamma(s)) = \pi r_0^2 \end{cases} \tag{4.6}$$

For the sake of simplicity, the cross-sections are assumed to be circular, the radius at time t of the cross-section located at arc-length s is denoted $r(s,t)$ and satisfies the relation $A(s,t) = \pi r^2(s,t)$. The time derivative of the radius gives the radial growth velocity and is denoted $v_r = \partial_t r$.

4.2.2 Planar motion of a growing stem

We now present the system of partial differential equations modelling the motion of an inextensible and unshearable growing rod in the Euclidean plane $(\boldsymbol{i},\boldsymbol{j})$. The rod is subjected to body force per unit length $\boldsymbol{f} = f_x\boldsymbol{i} + f_y\boldsymbol{j}$. The initial inclination of the stem is defined by the angle θ_0 from $\boldsymbol{i}$, and we denote θ the state variable describing the angle between $\boldsymbol{i}$ and the tangent of the current configuration $\boldsymbol{r}$ (see figure 4.1(b)).

The system

The initial-boundary value problem modelling the biomechanics of a growing rod for $(s,t) \in Q$, is given by:

$$\partial_s n_x = -f_x \tag{4.7}$$
$$\partial_s n_y = -f_y \tag{4.8}$$
$$\partial_s m = n_x \sin\theta - n_y \cos\theta \tag{4.9}$$
$$\partial_t \kappa^* = 2\frac{\partial_t A}{A}(\partial_s \theta - \kappa^*) + p \tag{4.10}$$
$$\partial_s \theta = \kappa^* + \frac{4\pi}{EA^2} m \tag{4.11}$$
$$\partial_s \boldsymbol{r} = \cos\theta \boldsymbol{i} + \sin\theta \boldsymbol{j} \tag{4.12}$$

with the initial and boundary conditions:

$$n_x(L(t),t) = 0 \tag{4.13}$$
$$n_y(L(t),t) = 0 \tag{4.14}$$
$$m(L(t),t) = 0 \tag{4.15}$$
$$\kappa^*(s,\gamma(s)) = \kappa^\circ(s) \tag{4.16}$$
$$\theta(0,t) = \theta_0 \tag{4.17}$$
$$\boldsymbol{r}(0,t) = \boldsymbol{0} \tag{4.18}$$

where equations (4.7),(4.8) and (4.9) correspond to the quasi-static balance equations, in which $\boldsymbol{n} = n_x \boldsymbol{i} + n_y \boldsymbol{j}$ is the contact force and m the moment. Then, equation (4.10) represents the evolution of the curvature in the relaxed configuration due to the remodelling effects of growth [13]. Equation (4.11) corresponds to the linear constitutive relation of an inextensible and unshearable rod, with E the Young's modulus. Finally, equation (4.12), where $\boldsymbol{r} = r_x \boldsymbol{i} + r_y \boldsymbol{j}$, gives the position of the cross-sections in the current configuration.

Primary tropism

The curvature induced by the differential growth at the shoot apical meristem correspond to the initial condition (4.16), which is given by:

$$\kappa^\circ(s) = \kappa_{\max} \sin\left(\frac{\theta_P - \theta(s,\gamma(s))}{2}\right) \tag{4.19}$$

where $\kappa_{\max}$ is the maximum curvature induced by primary growth and θ_P is the preferential angle of orientation, which is equal to $\pi/2$ in the case of gravitropism.

Secondary tropism

The function p in equation (4.10), takes into account changes in curvature due to the formation of reaction wood, and we assume the following relation [10]:

$$p = \sqrt{\pi}\frac{\partial_t A}{A^{3/2}} \alpha \sin(\theta_P - \theta) \tag{4.20}$$

where α is the maximum differential in maturation strains between normal and reaction wood.

4.3 The optimal control problems

In this section, we address the mathematical formulation of the two optimal control problems considering a *differentiate-then-discretize* approach [15, 16]. After defining the objective functionals, the first-order necessary conditions are derived leading to the computation of the adjoint equations and the gradient of the objective functionals.

4.3.1 Objective functionals

Optimal control problems can be now formulated in term of a dynamic biomass allocation strategy. Considering an ecological context with intense competition for light, the following objective function represents the integration of the height reached at each time, for $(\xi, \eta) \in \mathcal{K}_1 \times \mathcal{K}_2$ we have:

$$J_1(\xi, \eta) = \int_0^T r_y(L(t), t)\mathrm{d}t = \int_0^T \int_0^{L(t)} \sin\theta(s, t)\mathrm{d}s\mathrm{d}t \tag{4.21}$$

In the case of trees emerging from a closed canopy, the objective function is defined by the height reached at the final target date T, for $(\xi, \eta) \in \mathcal{K}_1 \times \mathcal{K}_2$ we have:

$$J_2(\xi, \eta) = r_y(L(T), T) = \int_0^{L(T)} \sin\theta(s, T)\mathrm{d}s \tag{4.22}$$

Finally, the dynamic biomass allocation strategy maximizing height is the solution of the following constrained maximization problems:

$$\begin{cases} \underset{(\xi,\eta)\in\mathcal{K}_1\times\mathcal{K}_2}{\text{maximize}} & J_k(\xi, \eta) \\ \text{subject to} & (4.2), (4.6), (4.7), (4.8), (4.9), (4.10), (4.11), (4.13), (4.14), (4.15), (4.16), (4.17) \end{cases} \tag{4.23}$$

for $k = 1, 2$.

4.3.2 Adjoint equations

Lagrangian functional

We first introduce the Lagrangian functional associated to the objective functional J_1 in the maximization problem (4.23). The states variables are denoted:

$$\boldsymbol{u} = (n_x, n_y, m, \theta, \kappa^*, A, L)$$

the control variables are denoted:

$$\boldsymbol{v} = (\xi, \eta)$$

the Lagrange multipliers associated to the state variables are denoted:

$$\boldsymbol{\lambda} = (\lambda_{n_x}, \lambda_{n_y}, \lambda_m, \lambda_\theta, \lambda_{\kappa^*}, \lambda_A, \lambda_L)$$

the Lagrange multipliers associated to the boundary or initial conditions of the state variables are denoted:

$$\boldsymbol{\sigma} = (\sigma_{n_x}, \sigma_{n_y}, \sigma_m, \sigma_\theta, \sigma_{\kappa^*}, \sigma_A, \sigma_L)$$

The variables $\boldsymbol{u}, \boldsymbol{v}, \boldsymbol{\lambda}$ and $\boldsymbol{\sigma}$ are considered to be independent and belong to the following functional spaces:

$$\boldsymbol{u} \in \left(L^2(0, T; H^1(\mathbb{R}^+))\right)^6 \times H^1(0, T)$$

$$\boldsymbol{v} \in L^2(0, T) \times L^2(0, T; H^1(\mathbb{R}^+))$$

$$\boldsymbol{\lambda} \in \left(L^2(0,T;H^1(\mathbb{R}^+))\right)^6 \times H^1(0,T)$$
$$\boldsymbol{\sigma} \in \left(L^2(0,T)\right)^4 \times \left(L^2(0,L(T))\right)^2 \times \mathbb{R}$$

Then, the Lagrangian functional is defined as follows:

$$\begin{aligned}
\mathcal{L}(\boldsymbol{u},\boldsymbol{v},\boldsymbol{\lambda},\boldsymbol{\sigma}) &= \int_0^T \int_0^L \sin\theta \mathrm{d}s\mathrm{d}t \\
&+ \int_0^T \int_0^L (\partial_s n_x + f_x)\lambda_{n_x} \mathrm{d}s\mathrm{d}t + \int_0^T n_x(L,t)\sigma_{n_x}(t)\mathrm{d}t \\
&+ \int_0^T \int_0^L (\partial_s n_y + f_y)\lambda_{n_y} \mathrm{d}s\mathrm{d}t + \int_0^T n_y(L,t)\sigma_{n_y}(t)\mathrm{d}t \\
&+ \int_0^T \int_0^L (\partial_s m - n_x \sin\theta + n_y \cos\theta)\lambda_m \mathrm{d}s\mathrm{d}t + \int_0^T m(L,t)\sigma_m(t)\mathrm{d}t \\
&+ \int_0^T \int_0^L \left(\partial_s \theta - \kappa^* - \frac{4\pi}{EA^2} m\right)\lambda_\theta \mathrm{d}s\mathrm{d}t + \int_0^T (\theta(0,t) - \theta_0)\sigma_\theta(t)\mathrm{d}t \\
&+ \int_0^T \int_0^L \left(\partial_t \kappa^* - \frac{\eta(1-\xi)q}{\rho}\left(\frac{2}{A}(\partial_s\theta - \kappa^*) + \frac{\alpha\sqrt{\pi}}{A^{3/2}}\sin(\theta_P - \theta)\right)\right)\lambda_{\kappa^*}\mathrm{d}s\mathrm{d}t \\
&+ \int_0^{L(T)} \left(\kappa^*(s,\gamma(s)) - \kappa_{\max}\sin\left(\frac{\theta_P - \theta(s,\gamma(s))}{2}\right)\right)\sigma_{\kappa^*}(s)\mathrm{d}s \\
&+ \int_0^T \int_0^L \left(\partial_t A - \frac{\eta(1-\xi)q}{\rho}\right)\lambda_A \mathrm{d}s\mathrm{d}t + \int_0^{L(T)} \left(A(s,\gamma(s)) - \pi r_0^2\right)\sigma_A(s)\mathrm{d}s \\
&+ \int_0^T \left(\frac{\mathrm{d}L}{\mathrm{d}t} - \frac{\xi q}{\rho\pi r_0^2}\right)\lambda_L \mathrm{d}t + \sigma_L L(0)
\end{aligned} \tag{4.24}$$

Derivation of the adjoint equations

The first-order necessary conditions of the Lagrangian stationarity leads to the computation of the adjoint equations. Thus, the Fréchet derivative in the direction $\phi \in L^2(0,T;H^1(\mathbb{R}^+))$ or $w \in H^1(0,T)$ defined as:

$$\langle \partial_x \mathcal{L}, \phi \rangle = \lim_{\epsilon \to 0} \frac{\mathcal{L}(x + \epsilon\phi) - \mathcal{L}(x)}{\epsilon}$$

is computed with respect to the state variables and leads to the following system of adjoint equations:

– $\langle \partial_{n_x} \mathcal{L}, \phi \rangle = 0$

$$\begin{cases} \partial_s \lambda_{n_x} + \lambda_m \sin\theta = 0 \\ \lambda_{n_x}(0,t) = 0 \\ \lambda_{n_x}(L(t),t) + \sigma_{n_x}(t) = 0 \end{cases} \tag{4.25}$$

– $\langle \partial_{n_y} \mathcal{L}, \phi \rangle = 0$:

$$\begin{cases} \partial_s \lambda_{n_y} - \lambda_m \cos\theta = 0 \\ \lambda_{n_y}(0,t) = 0 \\ \lambda_{n_y}(L(t),t) + \sigma_{n_y}(t) = 0 \end{cases} \tag{4.26}$$

– $\langle \partial_m \mathcal{L}, \phi \rangle = 0$:

$$\begin{cases} \partial_s \lambda_m + \frac{4\pi}{EA^2}\lambda_\theta = 0 \\ \lambda_m(0,t) = 0 \\ \lambda_m(L(t),t) + \sigma_m(t) = 0 \end{cases} \tag{4.27}$$

– $\langle \partial_\theta \mathcal{L}, \phi \rangle = 0$:

$$\begin{cases} \partial_s \lambda_\theta = \cos\theta - (n_x \cos\theta + n_y \sin\theta)\lambda_m + \dfrac{\eta(1-\xi)q}{\rho}\left(\dfrac{2}{A}\partial_s \lambda_{\kappa^*} + \dfrac{\alpha\sqrt{\pi}}{A^{3/2}}\cos(\theta_P - \theta)\lambda_{\kappa^*}\right) \\ \lambda_\theta(0,t) = \sigma_\theta(t) + \dfrac{2\eta(0,t)(1-\xi(t))q(t)}{\rho A(0,t)}\lambda_{\kappa^*}(0,t) \\ \lambda_\theta(L(t),t) = \dfrac{2\eta(L(t),t)(1-\xi(t))q(t)}{\rho A(L(t),t)}\lambda_{\kappa^*}(L(t),t) \\ \qquad - \dfrac{\xi(t)q(t)}{\rho\pi r_0^2}\kappa_{\max}\cos\left(\dfrac{\theta_P - \theta(L(t),t)}{2}\right)\sigma_{\kappa^*}(L(t)) \end{cases} \tag{4.28}$$

– $\langle \partial_{\kappa^*} \mathcal{L}, \phi \rangle = 0$:

$$\begin{cases} \partial_t \lambda_{\kappa^*} = \dfrac{2\eta(1-\xi)q}{\rho A}\lambda_{\kappa^*} - \lambda_\theta \\ \lambda_{\kappa^*}(s,T) = 0 \\ \lambda_{\kappa^*}(s,\gamma(s)) = \sigma_{\kappa^*}(s) \end{cases} \tag{4.29}$$

– $\langle \partial_A \mathcal{L}, \phi \rangle = 0$:

$$\begin{cases} \partial_t \lambda_A = \dfrac{8\pi}{EA^3} m\lambda_\theta + \dfrac{\eta(1-\xi)q}{\rho}\left(\dfrac{2}{A^2}(\partial_s\theta - \kappa^*) + \dfrac{3}{2}\dfrac{\alpha\sqrt{\pi}}{A^{5/3}}\sin(\theta_P - \theta)\right)\lambda_{\kappa^*} \\ \lambda_A(s,T) = 0 \\ \lambda_A(s,\gamma(s)) = \sigma_A(s) \end{cases} \tag{4.30}$$

– $\langle \partial_L \mathcal{L}, w \rangle = 0$:

$$\begin{cases} \dfrac{\mathrm{d}\lambda_L}{\mathrm{d}t}(t) = \sin\theta(L(t),t) + f_x(L(t),t)\lambda_{n_x}(L(t),t) + f_y(L(t),t)\lambda_{n_y}(L(t),t) \\ \lambda_L(T) = 0 \\ \lambda_L(0) = \sigma_L \end{cases} \tag{4.31}$$

Another mathematical formulation of the adjoint equations

The previous system of adjoint equations is simplified, by differentiating (4.27) and substituting $\partial_s\lambda_\theta$ with (4.28), the Lagrange multiplier λ_θ is eliminated. We now obtain a boundary value problem for λ_m coupled to a final value problem for λ_{κ^*}. Thus, for $t \in [0,T]$ we define $\mathcal{V}^t$ such that:

$$\mathcal{V}^t = \left\{ v \in H^2([0,L(t)]) / v(0) = 0 \right\}$$

Then, the weak form is given by finding $\lambda_m(\cdot,t) \in \mathcal{V}^t$ such that, for all $v \in \mathcal{V}^t$:

$$\begin{aligned} &\int_0^{L(t)} \frac{EA^2}{4\pi}\partial_s\lambda_m \frac{\mathrm{d}v}{\mathrm{d}s}\mathrm{d}s + \int_0^{L(t)} (n_x\cos\theta + n_y\sin\theta)\lambda_m v \mathrm{d}s \\ &= \int_0^{L(t)} \cos(\theta) v \mathrm{d}s - \int_0^{L(t)} \lambda_{\kappa^*}\frac{(1-\xi)q}{\rho}\left[\left(2\frac{A\partial_s\eta - \eta\partial_s A}{A^2} - \eta\frac{\alpha\sqrt{\pi}}{A^{3/2}}\cos(\theta_P - \theta)\right)v + \frac{\eta}{A}\frac{\mathrm{d}v}{\mathrm{d}s}\right]\mathrm{d}s \\ &\qquad + \frac{4\pi}{EA^2}\frac{\xi(t)q(t)}{\rho\pi r_0^2}\kappa_{\max}\cos\left(\frac{\theta_P - \theta(L(t),t)}{2}\right)\lambda_{\kappa^*}(L(t),t)v(L(t)) \end{aligned} \tag{4.32}$$

This weak form is coupled to the final value problem:

$$\begin{cases} \partial_t\lambda_{\kappa^*} = \dfrac{2\eta(1-\xi)q}{\rho A}\lambda_{\kappa^*} + \dfrac{EA^2}{4\pi}\partial_s\lambda_m \\ \lambda_{\kappa^*}(s,T) = 0 \end{cases} \tag{4.33}$$

and by denoting $\lambda_\omega = \partial_s \lambda_{\kappa^*}$ we have to consider the following final value problem:

$$\begin{cases} \partial_t \lambda_\omega = \dfrac{(1-\xi)q}{\rho}\left(2\dfrac{A\partial_s\eta - \eta\partial_s A}{A^2} - \eta\dfrac{\alpha\sqrt{\pi}}{A^{3/2}}\cos\left(\theta_P - \theta\right)\right)\lambda_{\kappa^*} + (n_x\cos\theta + n_y\sin\theta)\lambda_m - \cos\theta \\ \lambda_\omega(s,T) = 0 \end{cases} \tag{4.34}$$

The formulation of the boundary value problem (4.32) coupled to the final value problems (4.33) and (4.34) suggests the same discretization approach as the one developed in [14], i.e. using Hermite finite element to solve (4.32) and a time integration scheme for (4.33) and (4.34). The remaining adjoint equations are then easily deduced by direct numerical integration. For (4.25) and (4.26) we have:

$$\begin{cases} \partial_s \lambda_{n_x} = -\lambda_m \sin\theta \\ \lambda_{n_x}(0,t) = 0 \end{cases} \tag{4.35}$$

and

$$\begin{cases} \partial_s \lambda_{n_y} = \lambda_m \cos\theta \\ \lambda_{n_y}(0,t) = 0 \end{cases} \tag{4.36}$$

for (4.30) we have:

$$\begin{cases} \partial_t \lambda_A = -\dfrac{2}{A} m \partial_s \lambda_m + \dfrac{\eta(1-\xi)q}{\rho}\left(\dfrac{2}{A^2}(\partial_s\theta - \kappa^*) + \dfrac{3}{2}\dfrac{\alpha\sqrt{\pi}}{A^{5/3}}\sin\left(\theta_P - \theta\right)\right)\lambda_{\kappa^*} \\ \lambda_A(s,T) = 0 \end{cases} \tag{4.37}$$

finally for (4.31) we obtain:

$$\begin{cases} \dfrac{\mathrm{d}\lambda_L}{\mathrm{d}t}(t) = \sin\theta(L(t),t) + f_x(L(t),t)\lambda_{n_x}(L(t),t) + f_y(L(t),t)\lambda_{n_y}(L(t),t) \\ \lambda_L(T) = 0 \end{cases} \tag{4.38}$$

Adjoint equations for the objective functional J_2

If we consider the maximization problem (4.23) with the objective functional J_2, we notice that:

$$J_2(\xi,\eta) = \int_0^{L(T)} \sin\theta(s,T)\mathrm{d}s = \int_0^T \int_0^L \sin\theta(s,t)\delta_T(t)\mathrm{d}s\mathrm{d}t$$

where δ_T is the Dirac function. Hence, the weak form (4.32) is modified as follows:

$$\begin{aligned} \int_0^{L(t)} \frac{EA^2}{4\pi}\partial_s\lambda_m\frac{\mathrm{d}v}{\mathrm{d}s}\mathrm{d}s + \int_0^{L(t)}(n_x\cos\theta + n_y\sin\theta)\lambda_m v\mathrm{d}s &= \int_0^{L(t)}\cos\theta(s,t)\delta_T(t)v(s)\mathrm{d}s \\ - \int_0^{L(t)}\lambda_{\kappa^*}\frac{(1-\xi)q}{\rho}\left[\left(2\frac{A\partial_s\eta - \eta\partial_s A}{A^2} - \eta\frac{\alpha\sqrt{\pi}}{A^{3/2}}\cos\left(\theta_P-\theta\right)\right)v + \frac{\eta}{A}\frac{\mathrm{d}v}{\mathrm{d}s}\right]\mathrm{d}s \\ + \frac{4\pi}{EA^2}\frac{\xi(t)q(t)}{\rho\pi r_0^2}\kappa_{\max}\cos\left(\frac{\theta_P - \theta(L(t),t)}{2}\right)\lambda_{\kappa^*}(L(t),t)v(L(t)) \end{aligned} \tag{4.39}$$

and (4.38) is given by:

$$\begin{cases} \dfrac{\mathrm{d}\lambda_L}{\mathrm{d}t}(t) = f_x(L(t),t)\lambda_{n_x}(L(t),t) + f_y(L(t),t)\lambda_{n_y}(L(t),t) \\ \lambda_L(T) = -\sin\theta(L(T),T) \end{cases} \tag{4.40}$$

4.3.3 Gradient evaluation of the objective functionals

The first-order necessary conditions of the Lagrangian stationarity with respect to the control variables ξ and η leads to the gradient evaluation of the objective functionals. From $\langle \partial_\eta \mathcal{L}, \phi \rangle$ and $\langle \partial_\xi \mathcal{L}, w \rangle$ with $\phi \in L^2(0,T;H^1(\mathbb{R}^+))$ and $w \in H^1(0,T)$, we deduce the gradient of J_k:

$$\begin{cases} \nabla_\eta J_k = -\dfrac{(1-\xi)q}{\rho}\left[\lambda_A + \left(\dfrac{2}{A}(\partial_s\theta - \kappa^*) + \dfrac{\alpha\sqrt{\pi}}{A^{3/2}}\sin(\theta_P - \theta)\right)\lambda_{\kappa^*}\right] \\ \nabla_\xi J_k = -\dfrac{q\lambda_L}{\rho\pi r_0^2} + \displaystyle\int_0^L \frac{\eta q}{\rho}\left[\lambda_A + \left(\frac{2}{A}(\partial_s\theta - \kappa^*) + \frac{\alpha\sqrt{\pi}}{A^{3/2}}\sin(\theta_P - \theta)\right)\lambda_{\kappa^*}\right] \mathrm{d}s \end{cases} \tag{4.41}$$

where $k = 1, 2$.

4.4 Numerical algorithm

In this section, we consider the numerical solution of the constrained maximization problem (4.23). We first consider the projected gradient method. However, as the numerical solution of the boundary value problem (4.32) needs the evaluation of $\partial_s\eta$ at the finite elements nodes, the distribution η is approximated by a cubic Hermite interpolation, and thus:

$$\eta \in \mathcal{Y} = \left\{ u \in L^2(Q) / \forall t \in [0,T], u(\cdot,t) \in H^1([0,L(t)]) \cap \mathcal{C}^1([0,L(t)]) \right\} \tag{4.42}$$

Therefore, the projection operator on the closed convex space $\mathcal{Y} \cap \mathcal{K}_2$ has to be computed, since no analytical formulation exists.

4.4.1 Projected gradient method

We assume that the state variables and the adjoint variables are discretized following the approach developed in [13]. If we consider that the biomass devoted to the growth per unit time is given by:

$$q(t) = \rho\pi v_a (v_r t + r_0)^2 \tag{4.43}$$

where v_a and v_r can be interpreted as constant apical growth velocity and radial growth velocity, then we can consider the following function as an initialization of the projected gradient:

$$\begin{cases} \xi^0(t) = \left(\dfrac{r_0}{v_r t + r_0}\right)^2 \\ \eta^0(s,t) = \dfrac{2(v_r t - \frac{v_r}{v_a}s + r_0)}{v_a t(v_r t + 2r_0)} \\ \partial_s\eta^0(s,t) = -\dfrac{2v_r}{v_a^2 t(v_r t + 2r_0)} \end{cases} \tag{4.44}$$

Then we consider the following steps of the projected gradient algorithm [16]:

0. Initilization of ξ^0 and η^0 with (4.44)

At each step k until stationarity:

1. Solve the state equations of section 4.2 and the adjoint equations presented in section 4.3.2 with the values of ξ^k and η^k.
2. Compute $\xi^{k+1} = P_1(\xi^k + \zeta_1 \nabla_\xi J(\xi^k, \eta^k))$
3. Compute $\eta^{k+1} = P_2(\eta^k + \zeta_2 \nabla_\eta J(\xi^k, \eta^k))$

where ζ_1 and ζ_2 are the steps size associated to the control variables. P_1 and P_2 are respectively the projection operator onto the closed convex $\mathcal{K}_1$ and $\mathcal{K}_2$.

4.4.2 Projection operator onto $\mathcal{K}_1$

For $\xi \in L^2([0,T])$, the projection operator onto the closed convex $\mathcal{K}_1$ is given by:

$$P_1(\xi)(t) = \min(\max(0, \xi(t)), 1) \tag{4.45}$$

4.4.3 Projection operator onto $\mathcal{K}_2$

As η belongs to $\mathcal{Y} \cap \mathcal{K}_2$ there is no analytical expression of the projection operator. Thus, this section is devoted to the computation of a projection operator for a finite dimensional approximation of η using Hermite finite elements.

Hermite finite elements

The cubic Hermite finite elements associate at each node s_i, for $0 \leq i \leq n$, the two piecewise cubic polynomials ϕ_i and ψ_i defined by:

$$\begin{cases} \varphi_i(s_j) = \delta_{ij} \quad \text{and} \quad \dfrac{\mathrm{d}\varphi_i}{\mathrm{d}s}(s_j) = 0 \\ \psi_i(s_j) = 0 \quad \text{and} \quad \dfrac{\mathrm{d}\psi_i}{\mathrm{d}s}(s_j) = \delta_{ij} \end{cases}$$

we then introduce the following finite dimensional subspace of $\mathcal{Y}$:

$$\mathcal{W}_h^n = \mathrm{span}\{\phi_0, \psi_0, \ldots, \varphi_n, \psi_n\}$$

and for $s \in [0, L]$ and $w \in \mathcal{W}_h^n$, we obtain the following decomposition:

$$w(s) = \sum_{i=0}^{n} w_i \varphi_i(s) + w_i' \psi_i(s)$$

We also introduce the finite dimensional subspace of $\mathcal{K}_2$:

$$\mathcal{K}_h^n = \left\{ w \in \mathcal{W}_h^n / \forall s \in [0, L], w(s) \geq 0 \text{ and } \int_0^L w(s)\mathrm{d}s = 1 \right\}$$

Characterization of the convex space $\mathcal{K}_h^n$

As $w \in \mathcal{K}_h^n$ is a non-negative cubic polynomials over the interval $[s_{i-1}, s_i]$, it can be written as follows [17]:

$$w(s) = (s_i - s)(a_i s + b_i)^2 + (s - s_{i-1})(c_i s + d_i)^2$$

where $(a_i, b_i, c_i, d_i) \in \mathbb{R}^4$. The, for $1 \leq i \leq n$ and $s \in [s_{i-1}, s_i]$, we denote:

$$\begin{aligned} \boldsymbol{N}_i(s) &= \begin{bmatrix} \varphi_{i-1}(s) & \psi_{i-1}(s) & \varphi_i(s) & \psi_i(s) \end{bmatrix}^T \\ \boldsymbol{w}_i &= \begin{bmatrix} w_{i-1} & w_{i-1}' & w_i & w_i' \end{bmatrix}^T \\ \boldsymbol{x}_i &= \begin{bmatrix} a_i & b_i & c_i & d_i \end{bmatrix}^T \end{aligned}$$

Hence, for $1 \leq i \leq n$, the relation $\boldsymbol{w_i}(\boldsymbol{x_i})$ is defined as follows:

$$\begin{cases} w_{i-1} = h_i(a_i s_{i-1} + b_i)^2 \\ w_{i-1}' = (c_i s_{i-1} + d_i)^2 - (a_i s_{i-1} + b_i)(a_i s_{i-1} + b_i - 2a_i h_i) \\ w_i = h_i(c_i s_i + d_i)^2 \\ w_i' = (c_i s_i + d_i)(c_i s_i + d_i + 2c_i h_i) - (a_i s_i + b_i)^2 \end{cases} \tag{4.46}$$

with the relations for $1 \leq i \leq n-1$:

$$\begin{cases} \boldsymbol{e}_3^T \boldsymbol{w}_i(\boldsymbol{x}_i) - \boldsymbol{e}_1^T \boldsymbol{w}_{i+1}(\boldsymbol{x}_{i+1}) = 0 \\ \boldsymbol{e}_4^T \boldsymbol{w}_i(\boldsymbol{x}_i) - \boldsymbol{e}_2^T \boldsymbol{w}_{i+1}(\boldsymbol{x}_{i+1}) = 0 \end{cases} \tag{4.47}$$

where for $1 \leq j \leq 4$, $\boldsymbol{e}_j^T$ is the projection giving the jth coordinate in the standard basis of $\mathbb{R}^4$. In addition, if $w \in \mathcal{K}_h^n$ we have also:

$$\sum_{i=1}^{n} \frac{h_i}{2}(w_{i-1} + w_i) + \frac{h_i^2}{12}(w'_{i-1} - w'_i) = 1 \tag{4.48}$$

Formulation of the minimization distance problem

We can now reformulate the projection of an element $v \in \mathcal{W}_h^n$ onto the closed convex $\mathcal{K}_h^n$ as the following finite dimensional minimization problem:

$$\begin{cases} \underset{\boldsymbol{x} \in \mathbb{R}^{4n}}{\text{minimize}} & \frac{1}{2} \sum_{i=1}^{n} \int_{s_{i-1}}^{s_i} \left(\boldsymbol{N}_i^T (\boldsymbol{v}_i - \boldsymbol{w}_i) \right)^2 \mathrm{d}s \\ \text{subject to} & (4.47), (4.48) \end{cases} \tag{4.49}$$

The Lagrangian function of the equality constrained minimization problem (4.49), is given by:

$$\begin{aligned} \mathcal{L}(\boldsymbol{x}, \boldsymbol{\lambda}, \boldsymbol{\mu}, \nu) = & \frac{1}{2} \sum_{i=1}^{n} \int_{s_{i-1}}^{s_i} \left(\boldsymbol{N}_i^T (\boldsymbol{v}_i - \boldsymbol{w}_i) \right)^2 \mathrm{d}s \\ & + \sum_{i=1}^{n-1} \lambda_i \left(\boldsymbol{e}_3^T \boldsymbol{w}_i - \boldsymbol{e}_1^T \boldsymbol{w}_{i+1} \right) \\ & + \sum_{i=1}^{n-1} \mu_i \left(\boldsymbol{e}_4^T \boldsymbol{w}_i - \boldsymbol{e}_2^T \boldsymbol{w}_{i+1} \right) \\ & + \nu \left(\sum_{i=1}^{n} \frac{h_i}{2} \left(\boldsymbol{e}_1^T \boldsymbol{w}_i + \boldsymbol{e}_3^T \boldsymbol{w}_i \right) + \frac{h_i^2}{12} \left(\boldsymbol{e}_2^T \boldsymbol{w}_i - \boldsymbol{e}_4^T \boldsymbol{w}_i \right) - 1 \right) \end{aligned} \tag{4.50}$$

where $\boldsymbol{\lambda}, \boldsymbol{\mu} \in \mathbb{R}^{n-1}$ and $\nu \in \mathbb{R}$ are the Lagrange multipliers. This optimization problem is finally solved numerically by the Newton method which needs the computation of the gradient and the Hessian of the Lagrangian function [18]. For $2 \leq i \leq n-1$, the gradient of the Lagrangian with respect to $\boldsymbol{x}_i$ is given by:

$$\begin{aligned} \nabla_{\boldsymbol{x}_i} \mathcal{L}(\boldsymbol{x}, \boldsymbol{\lambda}, \boldsymbol{\mu}, \nu) = & - \int_{s_{i-1}}^{s_i} \boldsymbol{N}_i^T (\boldsymbol{v}_i - \boldsymbol{w}_i) \boldsymbol{N}_i^T \nabla_{\boldsymbol{x}_i} \boldsymbol{w}_i \mathrm{d}s \\ & + \lambda_i \boldsymbol{e}_3^T \nabla_{\boldsymbol{x_i}} \boldsymbol{w}_i - \lambda_{i-1} \boldsymbol{e}_1^T \nabla_{\boldsymbol{x_i}} \boldsymbol{w}_i \\ & + \mu_i \boldsymbol{e}_4^T \nabla_{\boldsymbol{x_i}} \boldsymbol{w}_i - \mu_{i-1} \boldsymbol{e}_2^T \nabla_{\boldsymbol{x_i}} \boldsymbol{w}_i \\ & + \nu \left(\frac{h_i}{2} \left(\boldsymbol{e}_1^T \nabla_{\boldsymbol{x_i}} \boldsymbol{w}_i + \boldsymbol{e}_3^T \nabla_{\boldsymbol{x_i}} \boldsymbol{w}_i \right) + \frac{h_i^2}{12} \left(\boldsymbol{e}_2^T \nabla_{\boldsymbol{x_i}} \boldsymbol{w}_i - \boldsymbol{e}_4^T \nabla_{\boldsymbol{x_i}} \boldsymbol{w}_i \right) \right) \end{aligned} \tag{4.51}$$

For $i = 1$ we have:

$$\begin{aligned} \nabla_{\boldsymbol{x}_1} \mathcal{L}(\boldsymbol{x}, \boldsymbol{\lambda}, \boldsymbol{\mu}, \nu) = & - \int_{s_0}^{s_1} \boldsymbol{N}_1^T (\boldsymbol{v}_1 - \boldsymbol{w}_1) \boldsymbol{N}_1^T \nabla_{\boldsymbol{x}_1} \boldsymbol{w}_1 \mathrm{d}s \\ & + \lambda_1 \boldsymbol{e}_3^T \nabla_{\boldsymbol{x_1}} \boldsymbol{w}_1 \\ & + \mu_1 \boldsymbol{e}_4^T \nabla_{\boldsymbol{x_1}} \boldsymbol{w}_1 \\ & + \nu \left(\frac{h_1}{2} \left(\boldsymbol{e}_1^T \nabla_{\boldsymbol{x_1}} \boldsymbol{w}_1 + \boldsymbol{e}_3^T \nabla_{\boldsymbol{x_1}} \boldsymbol{w}_1 \right) + \frac{h_1^2}{12} \left(\boldsymbol{e}_2^T \nabla_{\boldsymbol{x_1}} \boldsymbol{w}_1 - \boldsymbol{e}_4^T \nabla_{\boldsymbol{x_1}} \boldsymbol{w}_1 \right) \right) \end{aligned} \tag{4.52}$$

and for $i = n$ we obtain:

$$\begin{aligned}\nabla_{\boldsymbol{x}_n}\mathcal{L}(\boldsymbol{x},\boldsymbol{\lambda},\boldsymbol{\mu},\nu) = &-\int_{s_{n-1}}^{s_n} \boldsymbol{N}_n^T(\boldsymbol{v}_n-\boldsymbol{w}_n)\boldsymbol{N}_n^T\nabla_{\boldsymbol{x}_n}\boldsymbol{w}_n\mathrm{d}s\\ &-\lambda_{n-1}\boldsymbol{e}_1^T\nabla_{\boldsymbol{x_n}}\boldsymbol{w}_n\\ &-\mu_{n-1}\boldsymbol{e}_2^T\nabla_{\boldsymbol{x_n}}\boldsymbol{w}_n\\ &+\nu\left(\frac{h_n}{2}\left(\boldsymbol{e}_1^T\nabla_{\boldsymbol{x_n}}\boldsymbol{w}_n+\boldsymbol{e}_3^T\nabla_{\boldsymbol{x_n}}\boldsymbol{w}_n\right)+\frac{h_n^2}{12}\left(\boldsymbol{e}_2^T\nabla_{\boldsymbol{x_n}}\boldsymbol{w}_n-\boldsymbol{e}_4^T\nabla_{\boldsymbol{x_n}}\boldsymbol{w}_n\right)\right)\end{aligned} \tag{4.53}$$

where $\nabla_{\boldsymbol{x}_i}\boldsymbol{w}_i$ is given by:

$$\begin{bmatrix} 2h_is_{i-1}(a_is_{i-1}+b_i) & 2h_i(a_is_{i-1}+b_i) & 0 & 0\\ 2a_is_{i-1}(2h_i-s_{i-1})+2b_i(h_i-s_{i-1}) & -2b_i+2a_i(h_i-s_{i-1}) & 2s_{i-1}(c_is_{i-1}+d_i) & 2(c_is_{i-1}+d_i)\\ 0 & 0 & 2h_is_i(c_is_i+d_i) & 2h_i(c_is_i+d_i)\\ -2s_i(a_is_i+b_i) & -2(a_is_i+b_i) & 2c_i(2h_is_i+s_i^2)+2d_i(h_i+s_i) & 2d_i+2c_i(h_i+s_i)\end{bmatrix} \tag{4.54}$$

In the same way, the Hessian matrix of $\mathcal{L}$ is computed for $2 \le i \le n-1$:

$$\begin{aligned}\nabla^2_{\boldsymbol{x}_i\boldsymbol{x}_i}\mathcal{L}(\boldsymbol{x},\boldsymbol{\lambda},\boldsymbol{\mu},\nu) = &\int_{s_{i-1}}^{s_i} \nabla_{\boldsymbol{x_i}}\boldsymbol{w}_i{}^T\boldsymbol{N}_i\boldsymbol{N}_i^T\nabla_{\boldsymbol{x}_i}\boldsymbol{w}_i-\boldsymbol{N}_i^T(\boldsymbol{v}_i-\boldsymbol{w}_i)\sum_{j=1}^{4}\nabla^2_{\boldsymbol{x}_i\boldsymbol{x}_i}(\boldsymbol{e}_j^T\boldsymbol{w}_i)\boldsymbol{e}_j^T\boldsymbol{N}_i\mathrm{d}s\\ &+\lambda_i\nabla^2_{\boldsymbol{x}_i\boldsymbol{x}_i}(\boldsymbol{e}_3^T\boldsymbol{w}_i)-\lambda_{i-1}\nabla^2_{\boldsymbol{x}_i\boldsymbol{x}_i}(\boldsymbol{e}_1^T\boldsymbol{w}_i)\\ &+\mu_i\nabla^2_{\boldsymbol{x}_i\boldsymbol{x}_i}(\boldsymbol{e}_4^T\boldsymbol{w}_i)-\mu_{i-1}\nabla^2_{\boldsymbol{x}_i\boldsymbol{x}_i}(\boldsymbol{e}_2^T\boldsymbol{w}_i)\\ &+\nu\left(\frac{h_i}{2}\left(\nabla^2_{\boldsymbol{x}_i\boldsymbol{x}_i}(\boldsymbol{e}_1^T\boldsymbol{w}_i)+\nabla^2_{\boldsymbol{x}_i\boldsymbol{x}_i}(\boldsymbol{e}_3^T\boldsymbol{w}_i)\right)+\frac{h_i^2}{12}\left(\nabla^2_{\boldsymbol{x}_i\boldsymbol{x}_i}(\boldsymbol{e}_2^T\boldsymbol{w}_i)-\nabla^2_{\boldsymbol{x}_i\boldsymbol{x}_i}(\boldsymbol{e}_4^T\boldsymbol{w}_i)\right)\right)\end{aligned} \tag{4.55}$$

where for $1 \le j \le 4$, we have:

$$\begin{aligned}\nabla^2_{\boldsymbol{x}_i\boldsymbol{x}_i}(\boldsymbol{e}_1^T\boldsymbol{w}_i) &= \begin{bmatrix}2h_is_{i-1}^2 & 2h_is_{i-1} & 0 & 0\\ 2h_is_{i-1} & 2h_i & 0 & 0\\ 0 & 0 & 0 & 0\\ 0 & 0 & 0 & 0\end{bmatrix}\\ \nabla^2_{\boldsymbol{x}_i\boldsymbol{x}_i}(\boldsymbol{e}_2^T\boldsymbol{w}_i) &= \begin{bmatrix}2s_{i-1}(2h_i-s_{i-1}) & 2(h_i-s_{i-1}) & 0 & 0\\ 2(h_i-s_{i-1}) & -2 & 0 & 0\\ 0 & 0 & 2s_{i-1}^2 & 2s_{i-1}\\ 0 & 0 & 2s_{i-1} & 2\end{bmatrix}\\ \nabla^2_{\boldsymbol{x}_i\boldsymbol{x}_i}(\boldsymbol{e}_3^T\boldsymbol{w}_i) &= \begin{bmatrix}0 & 0 & 0 & 0\\ 0 & 0 & 0 & 0\\ 0 & 0 & 2h_is_i^2 & 2h_is_i\\ 0 & 0 & 2h_is_i & 2h_i\end{bmatrix}\\ \nabla^2_{\boldsymbol{x}_i\boldsymbol{x}_i}(\boldsymbol{e}_4^T\boldsymbol{w}_i) &= \begin{bmatrix}-2s_i^2 & -2s_i & 0 & 0\\ -2s_i & -2 & 0 & 0\\ 0 & 0 & 2s_i(h_i+s_i) & 2(h_i+s_i)\\ 0 & 0 & 2(h_i+s_i) & 2\end{bmatrix}\end{aligned} \tag{4.56}$$

Finally, the numerical solution of the minimization problem (4.49) is equivalent to the computation of the projection $P_2(\eta)$ for $\eta(\cdot,t) \in \mathcal{W}_h^n$ at each time $t \in [0,T]$.

4.5 Conclusion

In this paper, the mathematical formulation of two optimal control problems representing tree's growth strategies in different ecological contexts has been investigated. Growth strategies have been

characterized by the dynamic biomass allocation in primary growth and the distribution along the stem of the biomass allocated to secondary growth. Starting from the system of partial differential equations modelling the biomechanics of a growing rod, two objective functionals have been proposed and their first-order necessary conditions have been assessed through an adjoint equations-based method. On of the major difficulties encountered during this study is the implementation of a projected gradient method, since the formulation of the problem imposes specific regularity conditions on the control variables. Hence, an intermediate minimization problem has been introduced to compute the needed projection operator onto a closed convex. Finally, this work gives detailed theoretical basis to solve numerically the optimal control problems related to the biomechanics of growing tress.

Acknowledgements

Thanks are due to Agropolis Fondation which supported this research work. AMAP (Botany and Computational Plant Architecture, http://amap.cirad.fr/) is a joint research unit which associates CIRAD (UMR51), CNRS (UMR5120), INRA (UMR931), IRD (2M123), and Montpellier 2 University (UM27).

References

[1] D. S. Falster, M. Westoby, Plant height and evolutionary games, Trends in Ecology and Evolution 18 (2003) 337–343.

[2] F. J. Thomson, A. T. Moles, T. D. Auld, R. T. Kingsford, Seed dispersal distance is more strongly correlated with plant height than with seed mass, Journal of Ecology 99 (2011) 1299–1307.

[3] M. Fournier, A. Stokes, C. Coutand, T. Fourcaud, B. Moulia, Ecology and biomechanics : a mechanical approach to the ecology of animals and plants, CRC Taylor and Francis, 2006, Ch. 1 : Tree Biomechanics and Growth Strategies in the Context of Forest Functional Ecology, pp. 1–33.

[4] M. Fournier, H. Bailleres, B. Chanson, Tree biomechanics: Growth, cumulative prestresses, and reorientations, Biomimetics 2 (1994) 229–251.

[5] B. Moulia, C. Coutand, C. Lenne, Posture control and skeletal mechanical acclimation in terrestrial plants: Implication for mechanical modeling of plant architecture, American Journal of Botany 93 (2006) 1477–1489.

[6] T. Alméras, M. Derycke, G. Jaouen, J. Beauchêne, M. Fournier, Functional diversity in gravitropic reaction among tropical seedlings in relation to ecological and developmental traits, Journal of Experimental Botany 60 (2009) 4397–4410.

[7] R. Herrera, C. Krier, C. Lalanne, E. H. M. Ba, A. Stokes, F. Salin, T. Fourcaud, S. Claverol, C. Plomion, (not) keeping the stem straight: a proteomic analysis of maritime pine seedlings undergoing phototropism and gravitropism, BMC Plant Biology 10 (2010) 217.

[8] M. Ba, F. Salin, T. Fourcaud, A. Stokes, Reorientation strategies in leaning stems of young maritime pine (*Pinus pinaster*) and loblolly pine (*Pinus taeda*), IAWA Journal 31 (2010) 465–480.

[9] C. Collet, M. Fournier, F. Ningre, A. P.-I. Hounzandji, T. Constant, Growth and posture control strategies in fagus sylvatica and acer pseudoplatanus saplings in response to canopy disturbance, Annals of Botany 107 (2011) 1345–1353.

[10] H. Yamamoto, M. Yoshida, T. Okuyama, Growth stress controls negative gravitropism in woody plant stem, Planta 216 (2002) 280–292.

[11] T. Fourcaud, P. Lac, Numerical modelling of shape regulation and growth stresses in trees. part i: An incremental static finite element formulation, Trees 17 (2003) 23–30.

[12] T. Fourcaud, F. Blaise, P. Lac, P. Castéra, P. de Reffye, Numerical modelling of shape regulation and growth stresses in trees. part ii: implementation in the amappara software and simulation of tree growth, Trees 17 (2003) 31–39.

[13] T. Guillon, Y. Dumont, T. Fourcaud, A mathematical framework for modelling the biomechanics of growing trees with rod theory, manuscript submitted for publication.

[14] T. Guillon, Y. Dumont, T. Fourcaud, Numerical methods for the biomechanics of growing trees, manuscript submitted for publication.

[15] M. Gunzburger, Adjoint equation-based methods for control problems in incompressible, viscous flows, Flow, Turbulence and Combustion 65 (2000) 249–272.

[16] M. Hinze, R. Pinnau, M. Ulbrich, S. Ulbrich, Optimization with PDE Constraints, Springer, 2009.

[17] L. Brickman, L. Steinberg, On nonnegative polynomials, The American Mathematical Monthly 69 (1962) 218–221.

[18] J. F. Bonnans, J. C. Gilbert, C. Lemaréchal, C. A. Sagastizábal, Numerical Optimization, Springer, 2006.

Chapitre 5

CONCLUSION ET PERSPECTIVES

5.1 Conclusion

La principale contribution de cette thèse concerne le développement d'un modèle mathématique permettant de tenir compte des spécificités de la croissance et de la biomécanique de l'arbre dans le cadre de la théorie des poutres. Cette nouvelle approche permet d'implémenter des méthodes numériques variées (et pas seulement celle d'Euler explicite) pour l'approximation des solutions mais aussi de mener des études approfondies sur la combinaison des effets qui induisent les mouvements de l'arbre. Ainsi, le modèle couplant la croissance et la biomécanique en temps continu met en évidence :

- la dépendance entre l'espace et le temps ;
- l'évolution de la configuration déchargée due à la croissance secondaire ;
- la direction de la croissance primaire qui dépend de l'orientation de l'axe dans la configuration actuelle.

Cependant, ces nouvelles caractéristiques ont conduit à de nombreuses difficultés théoriques pour l'étude et la résolution du système d'équations aux dérivées partielles.

La dépendance entre l'espace et le temps impose le développement de nouvelles méthodes numériques. Elles reposent sur la résolution à chaque instant de l'équation d'équilibre mécanique et de la mise à jour de la courbure intrinsèque des sections droites existantes. L'analyse des résultats numériques a montré que l'erreur globale de la méthode d'Euler explicite, correspondant aux approches incrémentales précédemment développées, peut atteindre des ordres de grandeur très importants. Dans ce contexte, si une méthode explicite est nécessaire (pour la facilité d'implémentation ou pour tenir compte de lois de comportement non linéaires), les méthodes de type prédiction-correction sont une alternative intéressante afin d'améliorer la précision des solutions numériques.

Enfin, ce modèle mathématique a permis de considérer les stratégies de croissance de l'arbre grâce à la formulation de problèmes de contrôle optimal. Ainsi, les conditions nécessaires d'optimalité ont pu être évaluées à partir du système d'équations adjointes. Cette démarche permettra alors d'étudier et de comparer les stratégies de croissance par rapport à l'allocation dynamique de la biomasse pour la croissance primaire et secondaire.

5.2 Perspectives

Les développements présentés dans cette thèse offrent de nouvelles perspectives dans plusieurs disciplines.

5.2.1 Mécanique théorique

L'extension de la théorie des poutres au processus de croissance surfacique proposée au chapitre 2, offre de nouvelles perspectives pour formuler une théorie mécanique générale de la croissance surfacique pour un continuum en trois dimensions. En effet, deux caractéristiques essentielles sont directement transposables à une théorie du continuum en trois dimensions. Il s'agit de la dépendance entre l'espace et le temps (pouvant annuler une dimension de l'espace) ainsi que la construction d'une configuration de référence statique en fonction des déformations dans la configuration actuelle. Cependant, la principale difficulté réside dans la superposition de nouveaux points matériels libres de contraintes sur la surface du solide préalablement déformée. Cette situation peut alors générer des contraintes résiduelles [1, 2]. Cette théorie permettrait d'analyser précisément le champ de contraintes sur les sections droites des arbres, ce qui pourrait être intéressant pour des applications en sylviculture ou pour l'étude de la fragilité des arbres au vent.

5.2.2 Mathématiques

D'un point de vue mathématique, il serait intéressant d'étudier l'existence et l'unicité d'une solution au système d'équations aux dérivées partielles présenté au chapitre 2. De même, l'analyse numérique de la convergence et des conditions de stabilité des schémas (chapitre 3) apporterait des informations importantes pour le choix de la méthode numérique en fonction des gammes de valeurs des paramètres. Enfin, une analyse théorique de l'existence et des caractéristiques des solutions aux problèmes de contrôle optimal (chapitre 4) permettrait d'obtenir des éléments complémentaires sur les stratégies d'allocation de la biomasse maximisant la hauteur de l'arbre selon le contexte écologique.

5.2.3 Biomécanique et croissance de l'arbre

En biomécanique de l'arbre, la prochaine étape de cette étude serait la validation expérimentale des résultats obtenus au chapitre 2. Cependant, elle pourrait appeler l'intégration d'autres éléments au modèle, comme les phénomènes viscoélastiques [3] ou l'excentricité de la croissance secondaire [4].

Par ailleurs, l'un des enjeux majeurs de ce travail est le développement des méthodes numériques pour l'analyse des mouvements de l'arbre dans l'espace à trois dimensions. Ces méthodes permettraient alors de considérer des structures branchées et d'envisager l'analyse des rétroactions entre l'architecture et la biomécanique de l'arbre.

Références

[1] K. Garikipati, The kinematics of biological growth, Applied Mechanics Reviews 62 (2009) 1–7.

[2] D. Ambrosi, G. Ateshian, E. Arruda, S. Cowin, J. Dumais, A. Goriely, G. Holzapfel, J. Humphrey, R. Kemkemer, E. Kuhl, Perspectives on biological growth and remodeling, Journal of the Mechanics and Physics of Solids 59 (4) (2011) 863–883.

[3] J.-D. M. Catherine Coutand and, G. Jeronimidis, J.-F. Destrebecq, Twig : A model to simulate the gravitropic response of a tree axis in the frame of elasticity and viscoelasticity, at intra-annual time scale, Journal of Theoretical Biology 273 (2011) 115–129.

[4] Y.-S. Huang, L.-F. Hung, L.-L. Kuo-Huang, Biomechanical modeling of gravitropic response of branches : roles of asymmetric periphery growth strain versus self-weight bending effect, Trees 24 (2010) 1151–1161.

Modélisation mathématique, simulation numérique et contrôle optimal des rétroactions entre biomécanique et croissance de l'arbre

Résumé

La hauteur des arbres est un trait écologique majeur représentant l'intensité de la compétition pour la lumière. De plus, la croissance des arbres est le résultat de multiples compromis afin de maintenir leur orientation verticale et leur stabilité mécanique tout en assurant les autres fonctions écophysiologiques. Le contrôle de l'orientation de la croissance est réalisé par deux mécanismes : la croissance différentielle au niveau du méristème apical et la formation de bois de réaction au cours de la croissance secondaire. Cependant, la modélisation simultanée de la croissance et des rétroactions biomécaniques dépasse le cadre classique de la mécanique des structures. En effet, le concept de configuration de référence devient imprécis dû à l'apparition de nouveaux points matériels libres de contraintes sur une surface déformée au cours de la croissance. Dans cette thèse, un nouveau formalisme mathématique est proposé à partir de la théorie des poutres et modélise simultanément les effets de la croissance et de la biomécanique de l'arbre. Afin de résoudre le système d'équations aux dérivées partielles, de nouvelles méthodes numériques sont développées et tiennent compte de la dépendance entre l'espace et le temps. Enfin, deux problèmes de contrôle optimal sont analysés, modélisant les stratégies d'allocation dynamique de la biomasse pour la croissance primaire et secondaire, en fonction de différents contextes écologiques. Ce travail offre de nouvelles perspectives sur les mathématiques de la mécanique de la croissance et ses applications en biologie.

Mots-clés : Biomécanique de l'arbre, Stratégie de croissance en hauteur, Croissance surfacique, Théorie des poutres, Méthode des éléments finis, Equations adjointes, Contrôle optimal, Méthode du gradient projeté.

Mathematical modelling, numerical simulation and optimal control of the interactions between tree growth and biomechanics

Abstract

Height is a major ecological trait for growing trees, representing the intensity for light competition. Moreover, tree height results from a trade-off between different functions, including tree mechanical stability. Trees develop growth strategies to maintain their vertical orientation and mechanical stability, in addition to other ecophysiological functions, through differential primary growth near the shoot apical meristem and formation of reaction wood during secondary growth. However, this coupling is a problematic issue since the progressive addition of new material on an existing deformed body makes the definition of a reference configuration unclear. This thesis presents a new mathematical framework for rod theory modelling simultaneously the interactions between the growth process and tree biomechanics. In order to solve the obtained system of partial differential equations, new numerical methods are developed and take into account the dependence between space and time, which is a specific feature of surface growth problems. Finally, the present work addresses the mathematical formulation of two optimal control problems characterising tree's growth strategies. Growth strategies are analysed with respect to the ecological context, through two variables, which are the ratio of biomass allocated to primary growth and the distribution of biomass allocated to secondary growth along the growing stem. This work gives new insights to the mathematical framework of surface growth mechanics and its applications in biology.

Keywords : Tree biomechanics, Height grwoth strategy, Surface growth, Rod theory, Finite element method, Adjoint equations, Optimal control, Projected gradient method.